HIGH THROUGHPUT MULTI-MODAL MICROFLUIDIC SYSTEM FOR ISOLATION OF BLOOD CELLS

A Dissertation
Presented to
The Academic Faculty

by

Bushra Tasadduq

In Partial Fulfillment
Of the Requirements for the Degree
Of Doctor of Philosophy in the
School of Electrical and Computer Engineering

Georgia Institute of Technology
August 2018

HIGH THROUGHPUT MULTI-MODAL MICROFLUIDIC SYSTEM FOR ISOLATION OF BLOOD CELLS

Approved by:

Dr. Todd A Sulchek, Advisor
School of Mechanical Engineering
Georgia Institute of Technology

Dr. Alexander Alexeev
School of Mechanical Engineering
Georgia Institute of Technology

Dr. Ali Fatih Sarioglu, Co-Advisor
School of Electrical and Computer Engineering
Georgia Institute of Technology

Dr. Wilbur A. Lam
Wallace H. Coulter, Department of Biomedical Engineering
Georgia Institute of Technology

Dr. Oliver Brand
School of Electrical and Computer Engineering
Georgia Institute of Technology

Dr. F. Levent Degertekin
School of Electrical and Computer Engineering
Georgia Institute of Technology

Date Approved: June 30, 2017

Dedicated to my husband, sons, parents and teachers especially my advisor Dr. Todd Sulchek

ACKNOWLEDGEMENTS

First, I would like to thank my advisor Dr. Todd Sulchek for his guidance and patience while we worked on this project. I would have never been able to accomplish my aim without his guidance and support during some difficult phases of my PhD work. Then, I would like to thank my co-advisor Dr. Fatih Sarioglu for his guidance especially in writing drafts for publications and his expert opinions in microfluidic based cell-sorting platforms. I would like to especially thank Dr. Alexander Alexeev for all his guidance in understanding the simulation data and its significance to understand the working mechanism of proposed research. I would also like to thank my committee members Dr. Oliver Brand, Dr. Wilbur Lam and Dr. F. Levent Degertekin for their time and guidance. I would also like to thank and acknowledge support of all my lab mates: Billy for flow experiment training, Betsy for her guidance in adhesion study, Wenbin Mao for simulations for tracking paper and Tom, Ahmad, Dan, Kipp, Patricia, Wenwei, Anna, Aaron, Kathryn, Michael, Katie, Katily, Muhymin, and Nick for their help and support. I would like to thank my undergraduate students, Mohamed El Banani for helping me in developing tracking algorithm and Brynn McFarland for doing AFM measurements.

During these five years of my PhD journey I have made many great friends who supported me outside the lab and outside my home country. I would like to say thanks to my very first and very dear friend in Atlanta, Sadia for her friendship, generosity and support. I would also like to thank Unaiza and Munzir for being great friends and neighbors and Sidra for not only being a great friend but also for her great sense of humor. I would also like to thank Javeria, Sarwat, Abeera and Ifrah for their friendship.

Lastly, I would like to say thank to my family especially my husband for all his unconditional support and encouragement. I would like to acknowledge support of my sons who made my days less stressful by smiling and playing silly games with me. I would like to thank my parents for their support, love and especially everyday phone call from my mother. I would also like to thank my mother in law for her support and help. I would also like to appreciate support of my siblings; Zaeem, Aiman and Zaufishan.

TABLE OF CONTENTS

LIST OF TABLES

LIST OF FIGURES

LIST OF SYMBOLS AND ABBREVIATIONS

ε	Aspect ratio
μ	Fluid viscosity
γ	Velocity ratio
Re	Fluid Reynolds's number
E	Young's modulus
N	Sample size
θ	Ridge inclination angle
Hg	Microfluidic channel gap size
L	Microfluidic channel length
W	Microfluidic channel width
H	Microfluidic channel height
d	Lateral distance between two consecutive ridges
w	Microfluidic channel ridge width
l	Microfluidic channel ridge length
F_D	Hydrodynamic drag force
F_R	Elastic force
D	Diameter of particles/cells
$\Delta y/ridge$	Particle/cell lateral displacement per ridge
ΔP	Pressure difference between channel inlet and outlet
Hr	Height of the ridge

λ	Correlation length
Ro	Initial radius
R'	Estimated radius
α	Decay length
MxN'	M, N' are the dimensions of the image
$\Delta z/ridge$	Displacement in z direction per ridge
$\bar{v}_f$	Average flow velocity in focused streamline
$\bar{v}_o$	Average flow velocity in outlet channel
L	Ligand
R	Receptor
Kon	On rate constant
K1	Rate of intracellular biochemical reactions
K2	Rate of intracellular biochemical reactions
Kd	Dissociation constant
f	*Ratio of sample to vertical sheath flow rates*
Qi	Volumetric flow rate of sample inlet
Qs	Volumetric flow rate of vertical sheath inlet
Hf	Height of the focused streamline
TIL	Tumor infiltrating lymphocytes
PD-1	Programmed cell death protein 1
MHC	Major histocompatibility complex
CD	Cluster of differentiation
CAR	Chimeric Ag receptor

CTCs	Circulating tumor cells
FACS	Fluorescence-activated cell sorting
MACS	Magnetic-activated cell sorting
ATPS	Aqueous two-phase systems
PSGL-1	P-selectin glycoprotein ligand-1
AFM	Atomic force microscopy
FNRBCs	Fetal nucleated red blood cells
BSA	Bovine serum albumin
DEP	Dielectrophoresis
DPBS	Dulbecco's phosphate-buffered saline
FBS	Fetal bovine serum
fps	Frames per second
PDMS	Polydimethylsiloxane
PMMA	Poly(methyl methacrylate)
COC	Cyclic olefin copolymer
RBCs	Red blood cells
WBCs	White blood cells
PIV	Particle image velocimetry
IM	Inertial microfluidics
DLD	Deterministic lateral displacement
MF	Membrane filters
CTLD	C-type lectin-like domains
CRD	Carbohydrate recognition domain

EGF	Epidermal growth factor
TCR	T cell receptor
ERK	Extracellular signal regulated kinase
PKB	Protein kinase B
PS	Polystyrene
mRNA	Messenger ribonucleic acid
Nr	Bond density
F_A	Adhesion force
Fc	Critical force

SUMMARY

Samples containing a complex blend of cells such as blood are information-rich, but require sample processing to extract meaningful results. Separation and sorting of blood cells is therefore critical to a variety of biomedical processing steps, including diagnostics, pharmaceutical purification, and improved study of cell biology. Unfortunately, commercially available blood sorting techniques have disadvantages including being labor intensive, deficient in accuracy, and high in cost to implement. A variety of microfluidic techniques utilizing label free biomarkers (size, stiffness, viscoelasticity and dielectrophoresis) have been used for blood sorting to increase automation and accuracy and decrease cost. But high throughput with high purity along with versatility is still challenging to achieve using a microfluidic platform.

In this study, we have developed a novel, multimodal microfluidic platform for cell sorting which utilizes size and adhesion as label-free biomarkers. The size biomarker is chosen as it is a distinguishing characteristic of subpopulation of blood cells and is easily tied to hydrodynamic and inertial separation forces and fractionation methods. The adhesion biomarker is chosen to be a more specific sorting parameter since cell molecular interactions govern important physiological processes such as stem cell homing, inflammation, immune modulation, and cancer metastasis. The ability to continuously sort cells according to presence and degree of specific adhesion without using labels marks a unique capability in cell separation.

The separation device consists of a microchannel with periodically arranged diagonal ridges. In the first part of the study, we have studied the impact of hydrodynamics

caused by the diagonal ridges on microparticle flow and how it can be optimized for size based sorting. We find that the diagonal ridges create helical flow fields that impact similar particles of different z-positions differently. We have successfully demonstrated that by incorporating z-axis focusing of the sample inlet so as to position all particles to a uniform z-position, we can make consistent the particle exposure to transverse flow fields for more accurate size-dependent sorting. With this key insight we have substantially improved the efficiency and accuracy of size based sorting. We are able to sort particles with an enrichment factor of $>10^4$ for small particles and for >13 large particles at a throughput of $2.8 \text{ X } 10^6$ particles/min. We are also able to sort white blood cells with an enrichment factor of 87 and recovery of 73% at a throughput of 10^7 cells /min. In this work, a novel three dimensional tracking algorithm is developed to analyze video microscopy for fast and accurate extraction of three dimensional trajectories of particles flowing inside the ridged microchannel. The extracted trajectories are used to understand the device working mechanism.

In the second part of this work, we have studied the impact of specific molecular attachment to the diagonal ridges on cell trajectories and thus used it for adhesion based sorting. The unique aspect of this sorting design is the impact of the gap size on cell trajectories and cell kinetics, in which a sufficiently small gap size can lightly squeeze the cells while flowing under the ridged part of the channel to increase the surface area for interaction between the ligand on cell surface and coated receptor molecule but large enough so that biomechanical properties, namely stiffness and viscoelasticity, do not dominate the cell separation mechanism. This way we can flow cells at high flow rate to achieve high throughput, while maintaining sensitivity to adhesiveness. We are able to

successfully sort HL60 and Jurkat cells based on their PSGL-1 expression. We demonstrate 26-fold and 3.8-fold enrichment of PSGL-1 positive and 4.4-fold and 3.2-fold enrichment of PSGL-1 negative Jurkat and HL60 cells respectively. We have also demonstrated the enrichment of PSGL-1 positive Jurkat cells to 3-fold using a five outlet fractionation device. The cells flow with a rate of 0.2 m/s or 0.54 million cells/s.

We believe this simple and cost effective multimodal blood cell sorting device can be used to fulfill the unmet requirements of a point of care diagnostic tool with high throughput and purity.

CHAPTER 1. INTRODUCTION

Blood plays an important role to access biomarkers in clinical diagnosis[1-4]. Blood constituents include plasma and cells, each with 55% and 45% volume fractions respectively. The cellular component of blood consists of erythrocytes (RBCs), leukocytes (WBCs), platelets and circulating rare-cells[5]. These cellular populations have different morphology, including shape and size. The cell population vary in count over a wide range, with erythrocytes (RBCs) 5 X10^9 cells/mL, leukocytes 5-10 X 10^6 /mL, platelets 2-5 X 10^8 cells/mL and rare cells 1 or fewer per mL of blood[6] (Figure 1). These different cell populations must be sorted (process called apheresis), for variety of biomedical processing steps, including diagnostics, pharmaceutical purification, and improved study of cell biology.

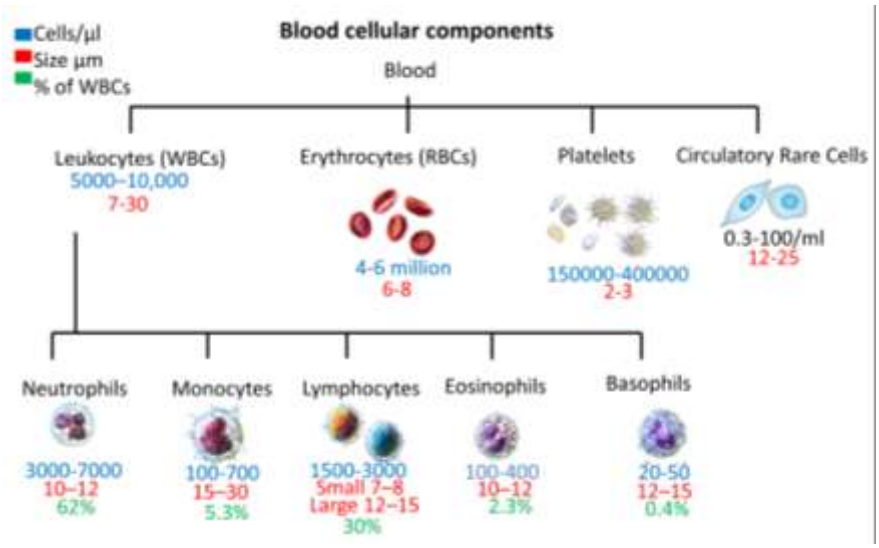

Figure 1 Blood cellular components with different size, shape and abundance. Size is a distinguishing characteristic of blood cells but for many applications one biomarker is insufficient.

In clinical diagnostics, platelet count is an indicator of impaired clotting and a marker for diseases such as leukemia or anemia[7-8]. Immunophenotyping of WBCs to examine their capability to release pro- and anti-inflammatory cytokines is a very effective tool for diagnosis of immune diseases like AIDS and tuberculosis [9-10]. RBCs counts are routinely used to diagnose diseases like anemia, sickle cell anemia, malaria, polycythemia[11]. Isolation of rare fetal cells such as fetal nucleated red blood cells (FNRBCs) from maternal circulation or cord blood is a non-invasive method of obtaining fetal DNA for prenatal genetic screening[12-14] and FNRBCs enumeration is also associated with fetal aneuploidies or pregnancy complications[15].

In cell therapeutics isolation and purification of leukocytes is essential for monitoring disease progression [16] and assessment of patient immune responses to immunomodulatory therapies[9-10]. Removal of leukocytes from blood, leukapheresis, is essential to reduce the white blood cell count in treating leukemic patients as well as to retrieve blood stem cells in patient with hematologic malignancies. [17-18] Removal of all leukocytes before performing a blood transfusion is essential to minimize transmission of cell-associated infectious agents (cytomegalovirus, herpes virus, human T-cell lymphoma virus), graft rejection rates and prevent febrile transfusion reactions[19]. For example depletion of T-cells from umbilical cord blood[20] increases efficacy of stem cell graft treatment[21-23]. Patients undergoing general surgery, organ transplants and trauma treatments frequently require platelet transfusion[24].

In cell biology, isolation of rare circulating tumor cells (CTCs) in blood for downstream molecular and cellular analysis has been of a great interest for both improving

cancer prognosis and understanding the cancer metastatic process[25-28]. Blood cell sorting studies are also carried to identify biomarkers for stem cells[29].

1.1 Design challenges for blood sorting devices

Blood cell sorting systems are designed with requirements like able to process small volume blood samples, high component purity, cell quality, less processing time and high operation efficiency. These technical challenges are further aggravated by needs, such as: (i) removing RBCs from whole blood, (ii) avoiding spontaneous platelet-triggered agglutination, (iii) capturing rare cells such as CTCs from patient blood[30], and (iv) targeting particular WBC subpopulations at various status[31].

1.2 Conventional blood sorting techniques

Conventional macroscale blood sorting techniques include centrifugation, apheresis, chemical lysis and antibody based techniques, fluorescence-activated cell sorting (FACS) and magnetic-activated cell sorting (MACS) [32-39] as shown in Figure 2. Centrifugation is commercially available, easy to conduct and the viability of fractionated blood cells is very high but it does not allow for high separation resolution, requires milliliters of blood for analysis which is not suitable for low-volume processing and requires dedicated labs and trained users. Because many leukocytes are designed to respond quickly to changes in their environment, they can easily be altered by handling procedures during the separation steps. Several studies document that the exposure of cells to improper stimuli during the blood processing steps can alter the original immuno-phenotype of the separated cells.[40-41] For example magnetic bead isolation in MACS can activate sorted cells. If these alterations occur, subsequent analysis may not be able to discriminate between the primary state of

target cells in the blood and the sample preparation artifacts. Also these techniques are inefficient because a significant portion of inactivated platelets are often lost either through high mechanical shear stress[42] or the purification process directly [43].

Macroscale flow-based protocols such as FACS or solid-state immobilization and capture of cells using MACS offers advantages like high specificity, high-throughput, commercial availability but are expensive and cannot reliably handle small number of cells. Fluid shear stresses in some devices and the use of fluorophores and antibodies may affect cell fate and function[38]. The use of FACS and MACs to sort rare circulating cells have limited success due to laborious sample preparations which introduce artifacts or lead to loss of desired cells [30]. Although MACS is cheaper, it has a lengthy protocol and cell loss occurs due to multiple wash steps. [39]

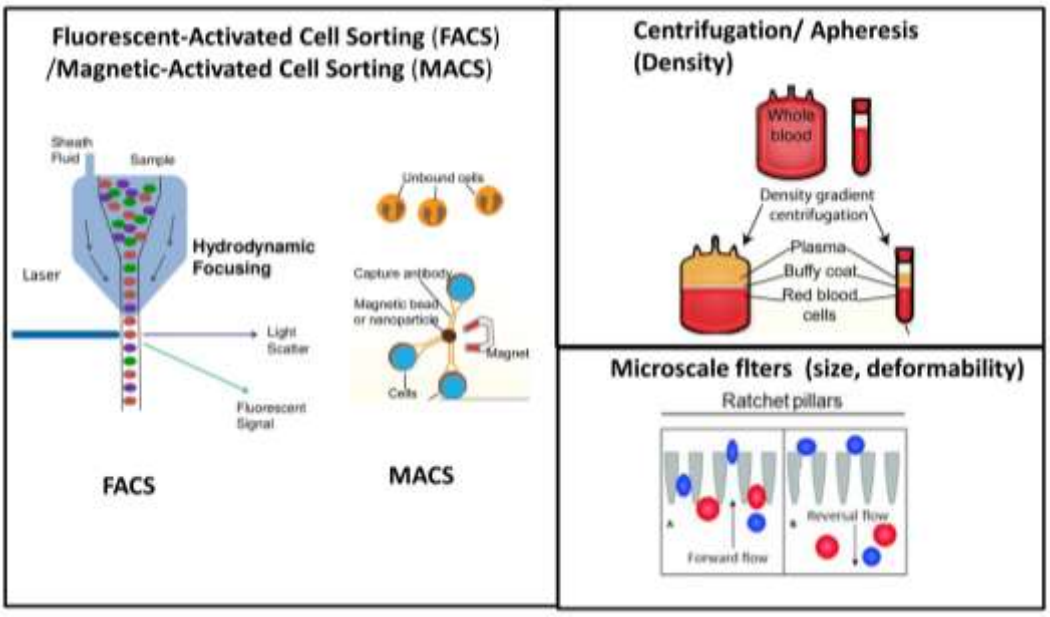

Figure 2 Commercially Available Blood Sorting Techniques. [31]

1.3 Microfluidics platform for sorting blood

Microfluidics offers a promising alternative to the conventional sorting methods since they have the potential to integrate the functionalities of sample preparation and analysis into a single enclosed chip, minimize reagent consumption, and can be inexpensively scaled for processing speed of the desired sample volume[44-46]. The microfluidic cell manipulation methods includes filters[47], hydrodynamic sorting[48], surface affinity sorting[49], magneticly actuated methods[50], acoustophoresis[51], electrical methods[52], aqueous two-phase systems (ATPS)[53], optical methods [54], sedimentation[55] and mimicking phenomena of the microvasculature[56].

Microscale filtration uses variations of size and deformability in cells to sort in which these properties are biomarkers of desired cell traits[57]. Filters are easily integrated with lab on a chip designs, but can only handle very small volumes due to clogging. Deformable rare cells such as CTCs may be damaged or lost as local perturbations in filters create conditions where extrusion through pores occurs, especially as the throughput is increased[58]. The isolation of larger cells from blood may be more challenging as large volume sample is required to get valid results[25].

Hydrodynamic sorting uses cell size and shape as actionable biomarkers. The use of hydrodynamic forces free the chip from using external force fields which simplifies integration into massively parallel systems[59]. Hydrodynamic chips have high resolution but often requires focusing or in co-flows [60] which results in dilution and have low throughput as compared to other microfluidic techniques. Additional passive methods can utilize hydrodynamic effects induced by channel geometry and microstructure[57, 61-63] such as membrane filters (MF) [64-65], deterministic lateral displacement devices (DLD)[60], and inertial microfluidics [57, 66-72]. Inertial microfluidics (IM) features high accuracy and high

throughputs comparable to MF.[68, 70, 73] An advantage of methods such as IM is use of continuous separation without any external control. [57, 62, 74].

Cell molecular interactions regulate important physiological processes such as stem cell homing, immune modulation, and cancer metastasis. Identifying and collecting cells that express desired molecular surface markers will thus benefit a variety of cell therapy and medical diagnostics. Label free separation techniques mentioned earlier that are operated by manipulating physical biomarkers such as size, stiffness and shape to sort cells have been successfully demonstrated during the last decade. Microstructures like grooves and herringbones[75] and techniques like hydrophoresis have been used to demonstrate label free cell sorting based on cell stiffness and shape. But sorted cells using techniques based on size, stiffness and shape do not provide enough specificity to cell type, and correlation to clinical condition. In order to address this problem, more specific label free cell sorting has been demonstrated recently using adhesion as a biomarker. Cell isolation adhesion based techniques based upon antibodies tagged with a fluorescent molecule enable fluorescence activated cell sorting (FACS) [76]and tagged with magnetic nanoparticles to enable MACS [39, 77]. Alternatively, label-free cells can be captured on a solid substrate using affinity based columns. Although FACS[76] offers high purity, with an enrichment of ~100-fold possible per color, the technique does not currently offer the possibility for fractionation into three or more outputs of finer sensitivity to the molecule of interest. In other words it provides a binary picture of the analog expression. With affinity-based methods (Figure 3 right), retrieval of the collected cells is usually difficult and requires harsh and inefficient release reagents. For example, a CD4 cell counting device recently developed[78] which used antibodies to capture CD 4 cells requires successive rinses

with several buffers to enumerate the captured cells. There are also challenges associated with release of affinity based captured cells without perturbing the cells' morphology, viability, molecular content and phenotype. Most common methods[79-80] of cell release by shear requires number of attachment points between the cells' antigens and immobilized surface and can damage fragile cells like CTCs [81].Additional mechanisms like enzymatically release of captured cells has been used to ensure sufficient cell viability.[82]. Also affinity sorting requires long incubation time and low flow rate, resulting in a low throughput despite using parallel channels[83] . Circulating tumor cells (CTCs) have been isolated with high purity and efficiency using affinity based sorting but requires improvement in design simplicity and over all processing time[84]. Low affinity molecules like lectins have been used for sorting cells though affinity columns[85] Binding of lectins depends on factors like metabolic state, stage of cell division and differentiation and surface protein glycosylation. Hence, it is useful for applications like isolating stem cells based on differentiation or homing potential[86-89]. Physiologically weak but very specific to cell type molecules like bacterial adhesion molecules[90], selectins involved in homing of circulating cells[91], and MHC-II molecules on antigen towards the T-cell receptor[92] can be used for molecule specific sorting. Out of these weak but specific molecule based sorting, ligand-selectin based sorting has been of great interest due to its potential applications in understanding the role of PSGL-1 in T cell immune response [93-94] and developing effective therapeutics. The tumor microenvironment can promote tumor growth by suppressing effector T cell responses. PSGL-1 is highly expressed on tumor infiltrating lymphocytes (TILs) that also expressed high PD-1 and TIM-3 inhibitory receptors. PSGL-1 deficiency does not change the trafficking of TILs into tumors but PSGL-1-deficient T cells had

reduced PD-1 expression and increased production of effector cytokines that resulted in delayed tumor growth. Hence, sorting of T cells based on their PSGL-1 expression can be used as an immune checkpoint inhibitor to limit anti-tumor T cell responses in the tumor microenvironment thereby promoting tumor growth[95]. Activated platelets can interact with lung cancer cells through PSGL-1. Inhibiting platelet activation and/or down-regulating PSGL-1 expression may be useful for suppression of tumor metastasis[96]. Selectins – glycoproteins involved in cell trafficking, have been used for cell separation purpose but they offer very low throughput as slow flow rates are required for cells to tether to coated surface [97-98] .

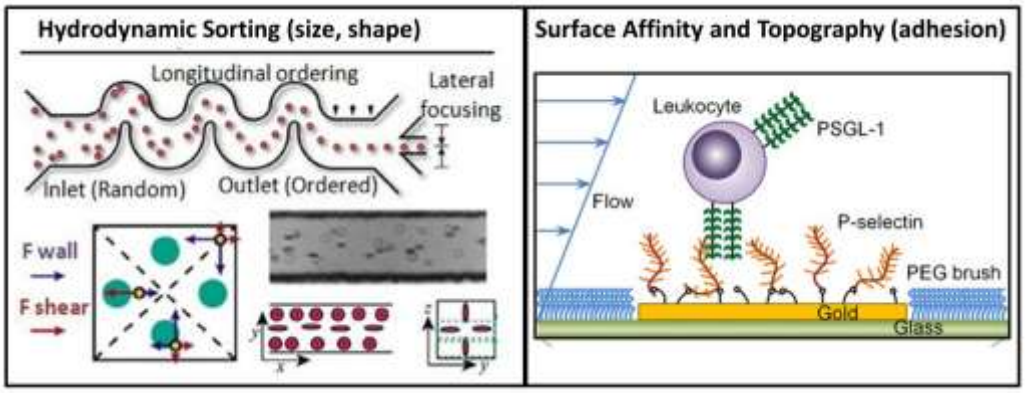

Figure 3 Microfluidic based cell/particle sorting techniques.[31]

Magnetic cell sorting typically use antibody-coated magnetic beads to push tagged cells into different flow streams. These methods are rapid and there is almost no interference to other properties of cells and media but the separation force in these systems decays with distance into flow[50]. It is also very convenient to conjugate antibodies of different affinities to magnetic microparticles. They often operate at low flow rates and dilution in sample preparation is common[99].

Dielectrophoresis uses polarizability and size as bio markers. They are rapid, precise, well controlled and can be easily integrated but have disadvantages including gene expression profiles also affected by this technique and there is also generation of hydrogen and oxygen gases and other undesired chemicals that are harmful to mammalian cells[52]. Elevated temperature due to Joule heating or high frequency are also factors that cannot be controlled.[31]

Acoustophoresis uses acoustic fields to push cells and as a result is highly sensitive to cell size, density and compressibility as biomarkers. Whole blood can be processed using this technique. They are usually used for focusing[51] or size based sorting . Ultrasonic actuation with the operating voltage greater than 10 V peak to peak would have adverse impacts on many important cellular functions[100].

1.4 Size and adhesion based multimodal platform for blood sorting

All the above discussed techniques (except microscale filters) use single biomarker to sort blood cells. Microscale filters use deformability and size but in an interdependent fashion. Using one parameter example size has problem of specificity. We cannot sort subpopulations of WBCs from CTCs and RBCs with high recovery and purity as there is an overlap of cell size range among these cell populations. One of the solutions is to use adhesion for more specific sorting. But adhesion based methods have problems of cell activation and low throughput. Therefore, there is a need for developing multimodal platform that addresses these problems. Among the above mentioned microfluidic blood sorting techniques combined multimodal size based hydrodynamic and surface affinity based sorting techniques offers following, inherent and potential advantages and are a

good candidate for addressing problems with unimodal system: (i) Size and molecule based adhesion are well established label free bio markers for blood sorting, (ii) both sorting mechanism can be integrated in a multi modal module for advanced sorting of target blood cells, (iii) integration of upstream microfluidic blood cell sorting with downstream molecular, cellular and functional analysis on the single-chip platform and (iv) unitary platform allows ease of integration and scalability.

The schematic of proposed multimodal device is shown in Figure 4. It consists of a microchannel with diagonal ridges decorated on top of the channel. These ridges create helical flow field that can be used to sort cells based on their size and adhesiveness. For size based sorting mode, helical flow field created by these ridges alter the position of particles in a size dependent manner. Multiple equilibrium heights would be a problem in this device as height dispersion of same size particle would lead to inaccurate trajectories of particles. But this issue can be addressed by using vertical sheath focusing which would give a more precise control over the trajectories of particles by controlling their height. The same device can switch to adhesive sorting mode by coating the device with cell adhesion molecule specific to target cell population. This way when cells are flown through the device they interact with coated channel and based on these adhesion events alter their trajectories. One major drawback of adhesion based sorting technique is its low throughput as ligand and receptor are needed to come in close proximity to start any adhesive event. The proposed device addresses this issue by optimizing the gap size which is defined as the distance between the bottom of channel and ridge. Gap size is selected to be small enough so that it lightly squeezes the cell to increase surface area for ligand receptor interaction but large enough that stiffness and size won't

play any role in sorting. This optimization enables us to operate at high flow rates with sufficient time and contact area for bonds to form. The proposed multimodal platform can be operated in sequential manner by integrating the two designs back to back on a single chip. This can be very useful for sorting WBCs from rest of the blood cells by first sorting blood sample based on size and then sorted WBCs through adhesion sorting part of the chip to specifically sort WBCs with high purity and throughput.

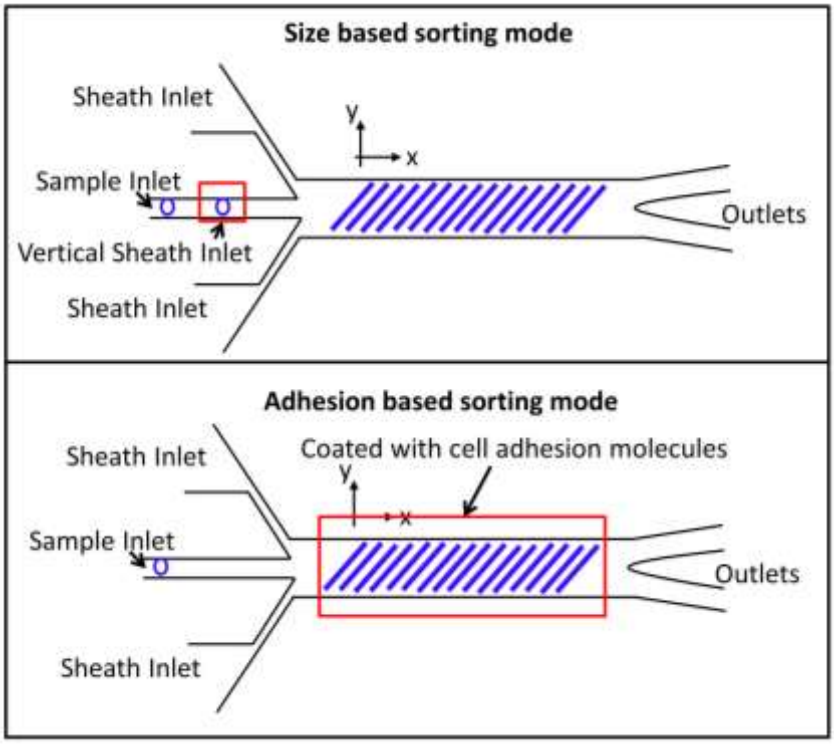

Figure 4 Conceptual schematic of multimodal blood sorting device.

The rest of the thesis has been divided into four chapters. The trajectories of particles flowing under ridged microchannel are investigated in the second chapter, which gives understanding of how vertical focusing can substantially improve size based sorting. A three dimensional tracking algorithm based on, on and off focus diffraction is developed to track particle trajectories in ridged microchannel and is used in this study. In Chapter 3,

an optimized design for the ridged microchannel with vertical sheath focusing for size based sorting is developed based on the findings of the Chapter 2. Results for white blood cells sorted from human blood using the optimized device are also presented. Next, in Chapter 4, we first understand the behavior of model cell lines HL60 and Jurkat flowing under the P-selectin coated device and developing a force model using experimental and simulated data. This study enables us to understand the adhesion based sorting mechanism. We also study the cell interaction with coated device at different flow rates. Finally, in Chapter 5, we discuss the potential applications and future of the proposed multimodal cell sorting device.

CHAPTER 2. INVESTIGATING RIDGED MICROCHANNEL FOR SIZE BASED SORTING

Note: Parts of this chapter are a modified version of the paper "Three-dimensional particle tracking in microfluidic channel flow using in and out of focus diffraction." Flow Measurement and Instrumentation 45 (2015): 218-224.

2.1 Introduction

Ridged microchannel has been previously reported to be used for cell sorting based on biophysical markers like stiffness [75, 101], size [102-103], adhesion [49, 98]and viscoelasticity [104].Although, the cited work on size and adhesion based ridged microchannel microfluidics offers high purity but at the cost of throughput and fabrication complexity. In this chapter ,we have investigated the interaction of particles with slanted ridges decorated on top of the channel to understand how the three dimensional focusing of the particles along with secondary flow which is created by the ridges,[103] would affect the particle trajectory. We have also studied the effect of inertia on particle trajectories for different channel geometries and flow rates. Inertial forces become dominant with increase in flow rate but this affect can be minimized by changing channel geometry.[57, 59, 105] A novel three dimensional tracking algorithm is developed using on and off focus diffraction which is used to determine three dimensional trajectories of particles using two dimensional video data. The extracted particle trajectories would help us better understand the sorting mechanism and enable us to come up with potential solutions to improve the throughput without using complex design and fabrication steps.

2.2 Microfluidic device

In this section the basic structure of the device is presented. The device consist of a microchannel with length L, width W and height H as shown in Figure 5.Top of the microchannel is decorated with ridges with width w ,height Hr and inclination angle of θ degree. The distance between the bottom of the channel and the ridge is defined as the gap size Hg. The distance between two consecutive ridges is defined as d. In size sorting device particles with diameter D are considered small if D<=2Hg and are considered large if D>=2Hg. There are two horizontal sheath inlets, one sample inlet and in the modified device which is discussed in chapter 3, one vertical sheath inlet has been added. There are multiple outlets at the end of the channel to collect the sorted sample.

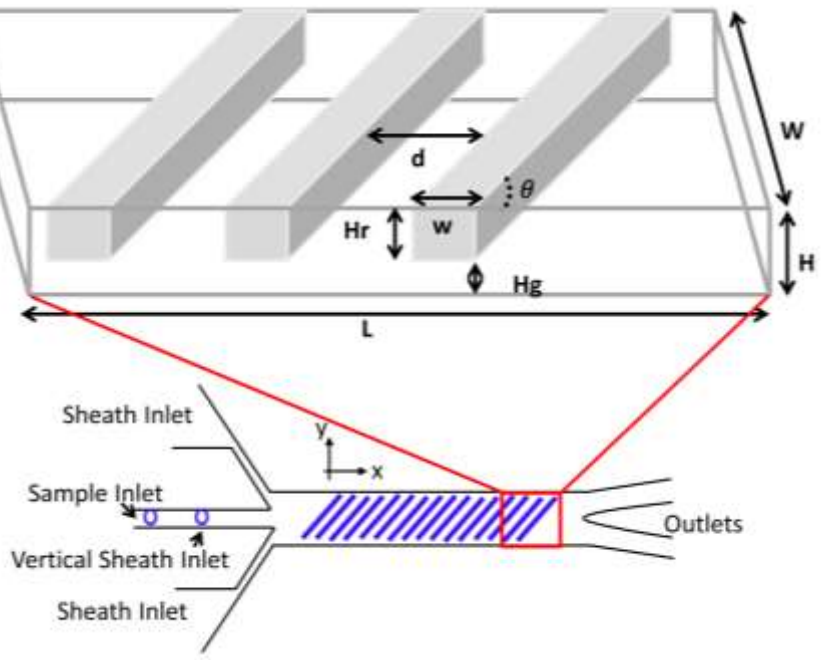

Figure 5 Bottom figure shows the proposed microfluidics for size based sorting with two horizontal sheath inlets, a sample inlet and in the modified version of the device a vertical focusing sheath inlet. The device has multiple outlets. The device parameters are defined in enlarged image on top.

2.3 Material and methods

2.3.1 Microfluidic device fabrication

The microfluidic device with gap size of 6.5µm was fabricated by replica molding Polydimethylsiloxane (PDMS) (Sylgard 184 Dow Corning Corp) on a permanent mold. The mold is made from SU-8 2007 using a two mask photolithography process. The mold dimensions were characterized with profilometry (Dektak 150 profiler) and verified with confocal microscopy imaging (Olympus LEXT). Uncured PDMS was mixed in a 10:1 ratio of elastomer to curing agent, then poured onto the SU-8 molds to a thickness of 1 cm and cured in an oven at 60 °C for 6 hours. The cured PDMS layer was cut and peeled off the mold and inlet and outlet holes were formed with a 1 mm biopsy punch. The PDMS device was treated with oxygen plasma (Harrick plasma cleaner PDS 32G) for 2 minutes then bonded to a glass microscope slide. To study the trajectories of particles the device with dimensions: L= 5.5 mm, W= 1000 µm and H= 25 µm. The ridges are w=20 µm wide and distance between two consecutive ridges is d=50 µm. The ridges are inclined at θ=45 degrees.

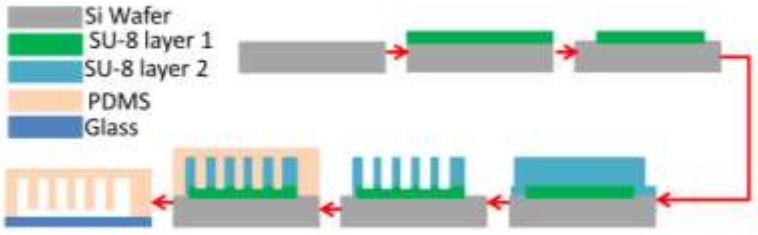

Figure 6 Process flow for fabrication of sorting device.

2.3.2 Sample preparation

Spherical polystyrene particles of 3 µm, 4 µm, and 6 µm diameters (Bangs Laboratories Inc.) were used in the flow experiments. Dispersions were prepared in deionized water with a concentration of approximately 2000 particles/µL.

2.3.3 Experimental setup

The particle solution was contained in a syringe and mounted on a syringe pump (PHD 2000 Harvard Apparatus), which infused the suspension at a controlled flow rate (0.0001 - 0.05 mL/min) through capillaries connected to a microfluidic channel. The microfluidic chip was mounted on an inverted microscope (Nikon Eclipse Ti). Particle trajectories were captured with a 40X objective and a high-speed camera (Phantom V7.3 Vision Research). In order to accurately record the trajectories of particles, high resolution (1150 by 1150 pixels) and high frame rate (≥3000 fps) videos were recorded for analysis.

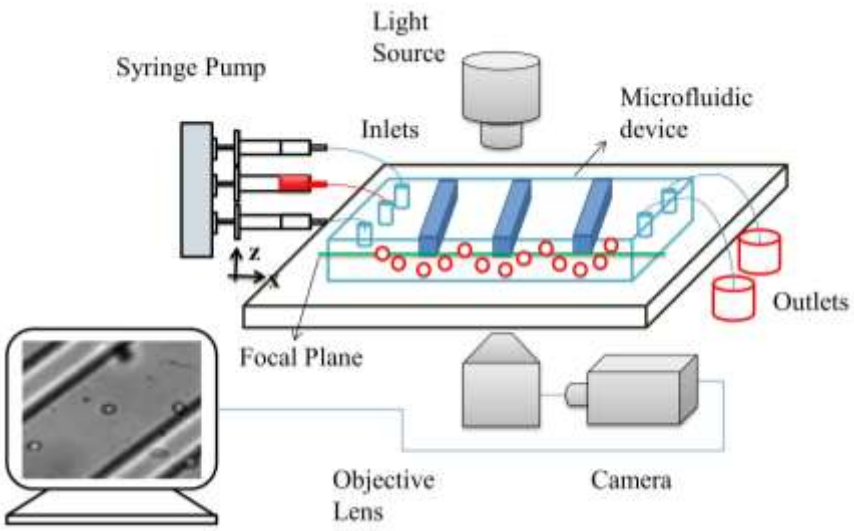

Figure 7 Experimental setup showing the microfluidic devices placed onto the microscope and a schematic of particles flowing through the device. The video frames are captured using a high speed camera and displayed on a computer.

2.4 Data analysis

We have used a customized MATLAB particle tracking code to analyze three dimensional coordinates of particle trajectories. Three-dimensional particle tracking is important to accurately understand the motion of particles within complex flow fields. We show that three-dimensional trajectories of particles within microfluidic flow can be extracted from two-dimensional bright field video microscopy. The method utilizes the defocusing that occurs as particles move out of the objective focal plane when viewed through a high numerical aperture objective lens. A fast and simple algorithm based on cross correlation to a set of reference images taken at prescribed amounts of defocus is used to extract out-of-plane particle position. In-plane particle position is determined through center point detection and therefore the particle position in all three dimensions can be constructed at each time point. Particle trajectories at high flow velocity of greater than 2 mm/s can be tracked by utilizing a high speed camera to obtain unblurred images. Three dimensional computational fluid simulations are used to validate the particle tracking methods.

2.4.1 Background

Conventional video microscopy depicts particle motion projected onto a plane defined by the focus of the objective. For many applications, visualization of motion in the third dimension is required to fully understand the trajectory of particles. Three-dimensional tracking particularly benefits visualizing particle motion in complex flow fields such as that in biomedical devices [106-109] and physiological systems. Several methods can be used to track particles in three dimensions. Laser Doppler velocimetry [110] utilizes

the wavelength shifts due to particle motion within the path of multiple lasers to reconstruct particle motion. Particle image velocimetry (PIV) measures the position and velocity of particles by pulsing a laser and observing the illuminated locations with microscopy [111]. Extending this technique, two cameras can be positioned along two Cartesian axes to track particles along all three dimensions [112-113]. Such systems can be complex to implement, however, and require careful alignment of the optical components which results in reduced observational volume that is limited by the optical depth of field in two dimensions. Recently, a single camera combined with multiple objectives was used to track particles in three-dimensions [114]. Single camera systems can also observe changes in the particle z-position through out-of-focus motion with respect to a fixed position, such as the water-glass interface [115], though this technique may be prone to aberrations in z-motion for large out-of-plane particle motion.

We here have developed an accurate and simple method for three-dimensional particle tracking within microfluidic channel flow that utilizes a single objective and a single high-speed camera. The method combines standard two-dimensional particle tracking from video [116] and a correlation algorithm that determines out-of-focus particle motion to additionally compute the third dimension. The out-of-focus correlation algorithm utilizes the contrast change and incremental changes in blurriness of the particle image that occurs as the particle moves in relation to the focal plane, as demonstrated in studies of particles actuated with a piezo-driven stage [117]. We have validated the algorithm for measuring particle out-of-plane motion flowing in a microfluidic channel by utilizing cross correlation of the particles to a set of reference images of a known position. To improve the resolution of the z-axis motion, interpolation of the reference images was implemented

to achieve submicron resolution. We have utilized this method to track the three dimensional trajectories of particles flowing at high speeds through a microfluidic channel.

2.4.2 Particle tracking algorithm

2.4.2.1 Lateral position algorithm

The two-dimensional image analysis tool is based upon the open source code PolyParticle Tracker optimized for noisy backgrounds [116]. A full description of the lateral position determination was described previously [116]. Each frame of the video was extracted through MATLAB routine and the image was smoothed to remove discretization noise by convolution with a Gaussian function. The convolution is given in terms of image intensity I(x,y) by the following equation:

$$I(x,y) = \sum_{i=-w}^{w} \sum_{j=-w}^{w} I_{raw}(x+i, y+j) e^{\frac{-i^2+j^2}{4\lambda^2}} \quad (1)$$

in which 2w+1 is the extent of the boxcar averaging used to model background in each frame and is an integer larger than a single sphere's apparent radius in pixels, but smaller than an intersphere separation. The correlation length, λ, is set to 1, and w = 3λ in order to sufficiently approximate the unbounded convolution. The local maximum or minimum in $I(x,y)$ determines the position of the particle (x_0, y_0) in each extracted image. For each extrema, the adjacent points of inflexion (x_0, y) and (x, y_0) were found. The initial radius R_0 is estimated as the mean distance to these four points of inflexion. To determine resolution below the pixel dimensions, a sub-pixel refinement was utilized [116] with

estimated position $(x_{0\,,}y_0)$ and radius R_0 by fitting the intensity map of the image $I(x,y)$ defined as:

$$I_{fit}(x,y) = \sum_{i=0,j=0}^{i+j=4} P_{ij}x^i y^i \tag{2}$$

The fit was weighted at each pixel by the Gaussian function:

$$W(x,y) = exp^{\frac{-\alpha(x^2+y^2)}{R'^2}} \tag{3}$$

in which R' is the estimated radius and α is the decay length set to the radius of the particle, which was determined from the image. The particle center was determined by the local maximum of the polynomial fit. A polynomial fit offered several advantages. Firstly, the fit is not sensitive to the edges of a particle but most sensitive to pixels well within the borders of the particle image. Secondly, the fit is optimized to identify spherical or elongated shapes. The third advantage is that, unlike the previous methods, the procedure of determining the particle center is inherently insensitive to the image background [116]. In order to link particle position from multiple frames to create a trajectory, we assume that the initial coordinates in the proceeding frame and choose a frame rate such that each particle will not move further than its own radius between two adjacent frames.

2.4.2.2 Axial position estimation algorithm

The images of a micrometer-scale particle appear to be very different when out-of-focus. As shown in Figure 8, the in-focus image of a microparticle has sharp edges with high contrast, while the out-of-focus image is diffuse with concentric diffraction rings. In general, the above-focus mages are distinct due to the inherent aberrations caused by the objective lens [115]. Therefore, once the relationship between the off-focus image of the particle and its axial position is established, it is possible to determine the axial positions of the particle from the acquired off-focus images. We determined the out-of-plane position of each particle by the degree of defocusing of the particle [118], evaluated by a correlation algorithm comparing the image to a set of reference images of a similar particle at specified amounts of defocusing. The reference image scale includes a single particle in focus and various degrees of out of focus by calibrated adjustment of the microscope objective. The set of reference images used in these experiments are shown in Figure 8. The degree of defocus is also related to the number and thickness of concentric diffraction rings, which accounts for uniqueness of the cross correlation approach. We utilized this feature of defocused images of microparticles to obtain a z-position scale. This scale can then be compared to a particle of interest to determine its z-position through a cross-correlation analysis. The cross-correlated algorithm was implemented using a MATLAB routine based on previous studies [118]. We take $[(x_1, y_1), (x_2, y_2), \ldots . (x_N, y_N)]$ and $[(a_1, b_1), (a_2, b_2), \ldots . , (a_N, b_N)]$ as the pixel coordinates for analyzed image and reference image respectively, in which N2 represents the feature size. The cross- correlation output matrix is calculated as a double matrix with $[(x_1 + a_1, y_1 + b_1), (x_2 + a_2, y_2 + b_2), \ldots . , (x_N + a_N, y_N + b_N)]$ pixel coordinates with $[c_1, c_2, \ldots . , c_N]$ corresponding correlation coefficients. From this output matrix we extract the x and y pixel coordinates

which correspond to the maximum value of correlation coefficient. This maximum value determines the relative likeness of the particle of interest and the reference image in each frame.

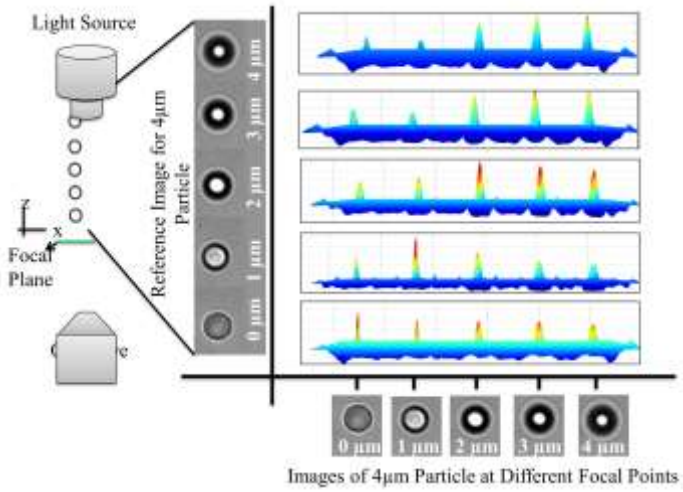

Figure 8 Reference images taken with different focal points for a 4 µm particle. Cross correlation coefficients are calculated between the particle images at known z-positions and the reference images. The z-position of the particle can thus be determined from the degree of defocus and is also related to the number and thickness of concentric diffraction rings.

To increase the resolution of the particle z-height, we utilized interpolation between adjacent reference images. The reference images were recorded with 1 µm spacing. We generate additional interpolated reference images as shown in Figure 9. Images are formatted in MATLAB as a 3D array (MxN'x3) where M, N' are the dimensions of the image and 3 layers for Red, Green and Blue layers. Values for each color layer of each pixel span 0 to 255. Starting with a set of images of the same particle at different depths (with the particle having the same position in each image, and that position being the center), and assuming that the change in the focus of the particles is continuous, we set the value of each pixel to be a function of the depth so that we have 3*M*N' functions. Using

the values of the pixels in the given set of images as initial values and applying spline interpolation to each function, we interpolate the value of each pixel at any given depth within the range of depths of the set of the reference mages. The interpolated values form an array which is then used to create the image. Selected interpolated images were compared with the original reference images and we found the relative error to be less than 2% using the MATLAB routine imshowpair. Figure 9 shows the interpolated images between reference images for 1 µm and 2 µm focal points, with a step size of 0.1 µm. When comparing a particle to the reference, the image was automatically cropped and centered to accurately determine the cross correlation coefficient. The center of the particle is determined using three points on the circumference and assuming circularity [119].

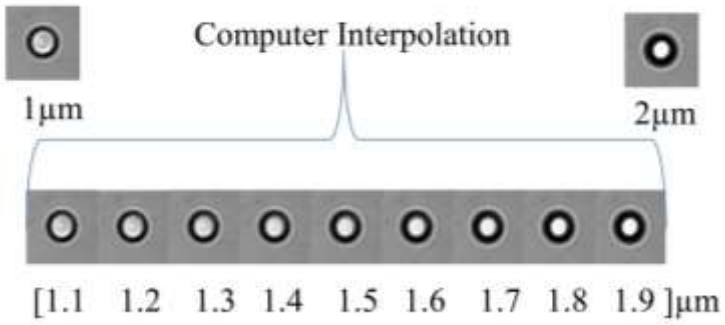

Figure 9 Utilizing two reference images at the focal points 1 µm and 2 µm, a set of interpolated images can be generated with a step size of 0.1 µm.

2.4.3 Results and discussion

For this study the microchannel with the top of the channel decorated with diagonal ridges generates helical recirculation and lateral pressure gradients , which results in helical trajectories of particles, as shown by experiments [107, 120-121] and simulation [122].

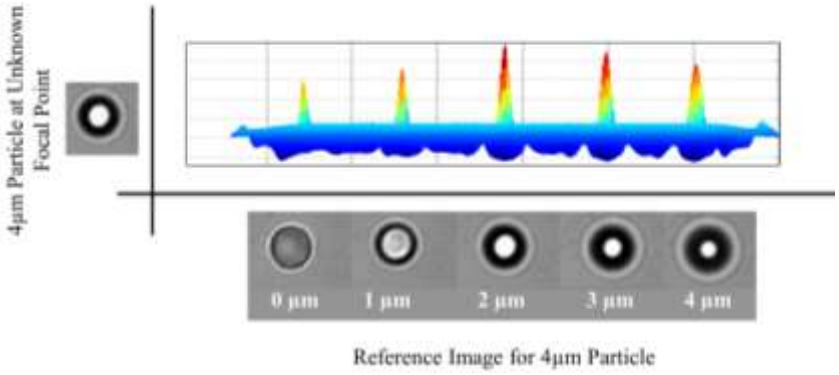

Figure 10 Determination of the z height is tested by calculating the cross correlation coefficient between a particle at an unknown z-position and the reference images.

The particle x and y coordinates for each time point were calculated as described in the methods. The z coordinate for each time point was determined through calculation of the cross correlation coefficient to the set of defocused reference images, as described in the methods. The calculation of the cross correlation coefficient of a particle from a typical still frame is shown in Figure 10. The z-position at each time point was combined with the calculated x- and y- coordinate to generate a three dimensional position. The analysis continued for all frames in the video to obtain a full three-dimensional trajectory for particles of various sizes.

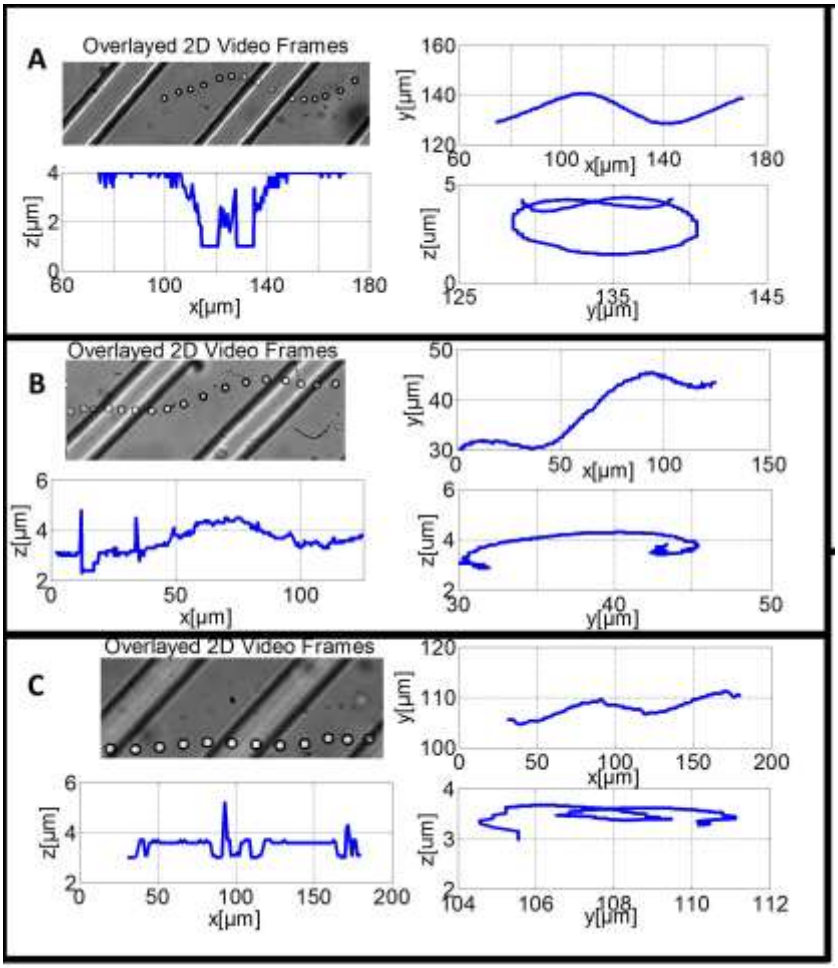

Figure 11 Experimentally calculated trajectories during one period of motion between ridges for A) 3μm B) 4μm and C) 6μm particles.

In Figure 11 we show the multiple axes views for 3 μm, 4 μm, and 6 μm particles and the overlayed 2D video frames. As expected from previous studies, we observe a sinusoidal motion in x-y plane and the x-z plane[107, 120-122]. The three dimensional visualization of the trajectory indicates helical motion. Previous studies have indicated that the trajectory should be particle-size dependent, in which larger particles having smaller magnitudes of y- and z- motion [122].Examining the x-y trajectories of particles with different sizes, we notice that the $\Delta y/ridge$ for the particles varies inversely with particle size, as expected from published reports [121]. This is further confirmed in Figure 12 which shows

the calculated $\Delta y/ridge$ and $\Delta z/ridge$ for different size particles. Hence, the methods presented in this work can be used to better understand how microfluidic flow can be utilized for particle size separation [120, 122].

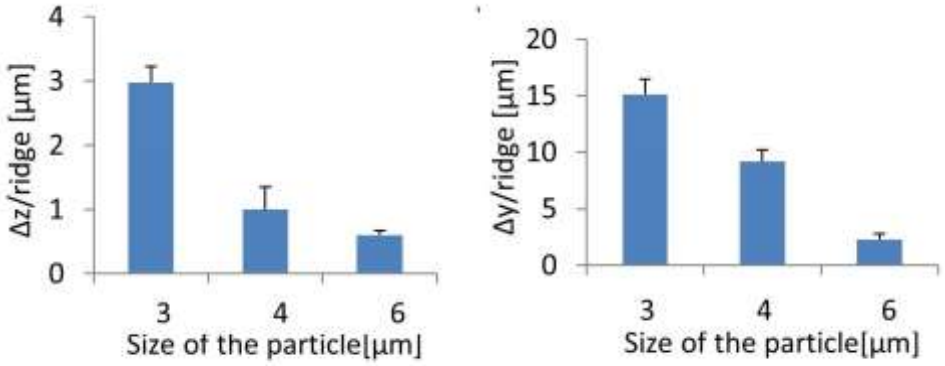

Figure 12 Data extracted from the computed trajectories show that different size beads move with different amplitudes in z (Δz/ridge) and show different amounts of transverse motion (Δy/ridge). The size dependence of Δy/ridge can be utilized for size-based separation.

To further validate the tracking results, we compare our measured trajectory to that obtained by previously validated computational fluid dynamics simulations [122]. Figure 13 shows the comparison of z-positions of simulated and experimental results of a particle flowing within the channel. The simulations fully considered the geometry of the device used, the size of the particles, and the flow rates used in the experiment. The results show that the tracked z-positions closely match the computationally expected path.

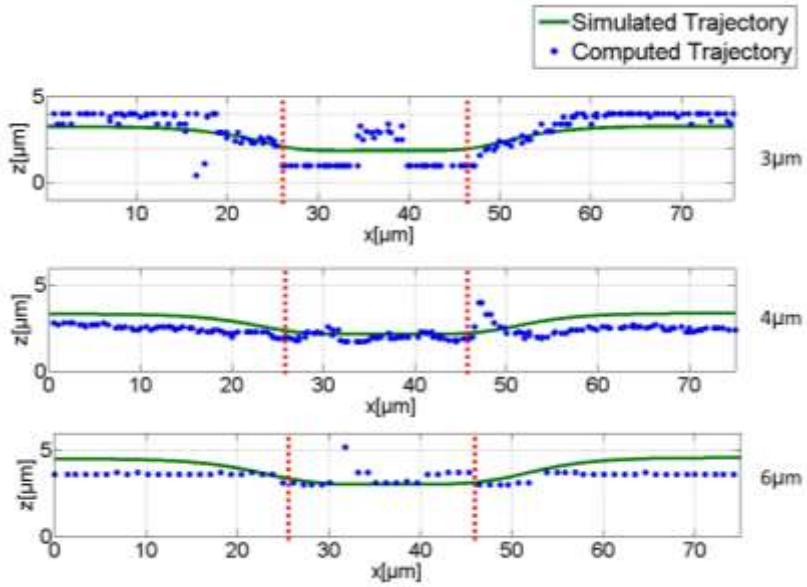

Figure 13 Comparison of the x-z experimental trajectories with the computationally simulated trajectories for different size particles.

The relative error between the experimental and simulated trajectories is calculated and shown in Figure 14. The error is found to be maximum where the particles are traversing under a microchannel ridge (x position range: 25 to 50μm). This is due the presence of channel features in the frames that that are not present in the calibrated reference images. One simple solution to remove this error is to utilize interpolation between the points where particle enters and leaves a ridge. Overall, the average error is approximately 25% which is acceptable as the particles are closely following the simulated trajectories [123]. Other sources of error include the estimation errors due to spatial sampling and noise [117]. We can improve the performance of the algorithm by using smaller step sizes in the generated reference images.

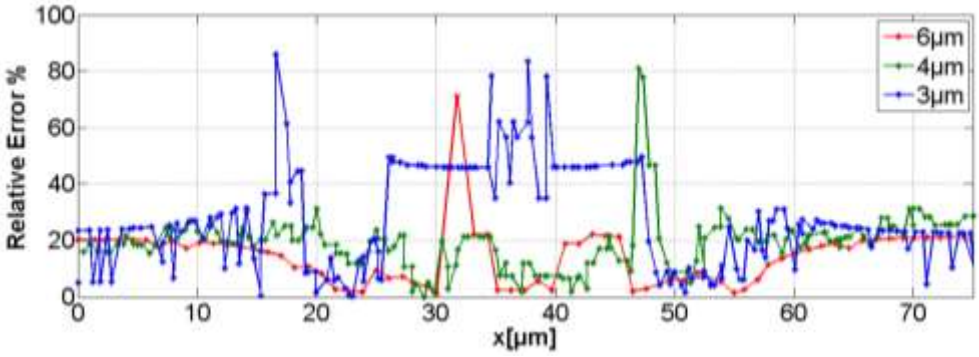

Figure 14 The relative error between the experimental and simulated trajectories during a typical trajectory, with the typical error between 20%-25%.

2.4.4 Conclusion

The results of particle trajectories suggests there exist a relationship between the size of the particle and the lateral distance it travels between two consecutive ridges in a ridged micrichannel and this relationship can be exploited to sort particles/cells based on their size.

2.5 Testing capability of size sorting device without vertical focusing

Based on the findings of previous section (2.4) we tested the size sorting device. Same device with following modification in device geometry is used: W=560 μm, L=3.8mm and Hg=8 μm. Spherical polystyrene particles of 4 μm, and 7 μm diameters (Bangs Laboratories Inc.) were used in the flow experiments. Dispersions were prepared in phosphate buffered saline (PBS) solution with a concentration of approximately 2000 particles/μL. To prevent bead adhesion, 0.01% v/v Tween 20 was added to flow media. Separated cells were collected at the outlets and were analyzed with an Accuri C6 flow cytometer (BD Biosciences).

2.5.1 Results and discussion

The performance parameter which is considered suitable for biological sample sorting [57, 105] we are using here is Enrichment factor which is defined as follows.

$$Enrichment\ Factor = \frac{\left(\frac{\%\ of\ Targeted\ Cells}{\%\ of\ Non\ Targeted\ Cells}\right)_{Outlet}}{\left(\frac{\%\ of\ Targeted\ Cells}{\%\ of\ Non\ Targeted\ Cells}\right)_{Inlet}} \quad (4)$$

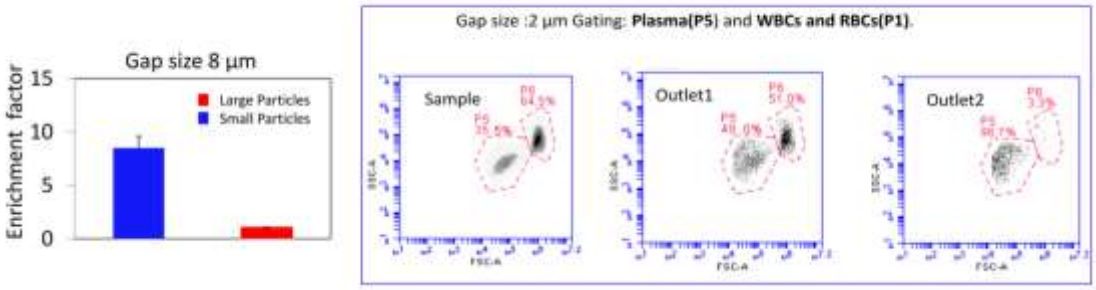

Figure 15 On left the chart showing results of separation. The device is able to separate 4 µm particles from 7 µm with a substantial enrichment of number density of 8.5-fold. On right, flow cytometer data showing platelet separation from RBCs and WBCs in whole blood.

The results in Figure 15 (left image) show that the small particles are substantially enriched by a ratio of percentages of outlet to inlet of 8.5-fold. However the enrichment of larger particles is substantially inferior, due to the variation in trajectories of the smaller particles. Therefore, this design of the microfluidic sorting is ideal for the applications where small size particles are required to be separated from the heterogeneous mixture. One example of this need is the separation of platelets from whole blood as is demonstrated in Figure 15(right image). The applications with whole blood, the width of the channel must be considered to avoid high shear rates which can activate platelets [124].

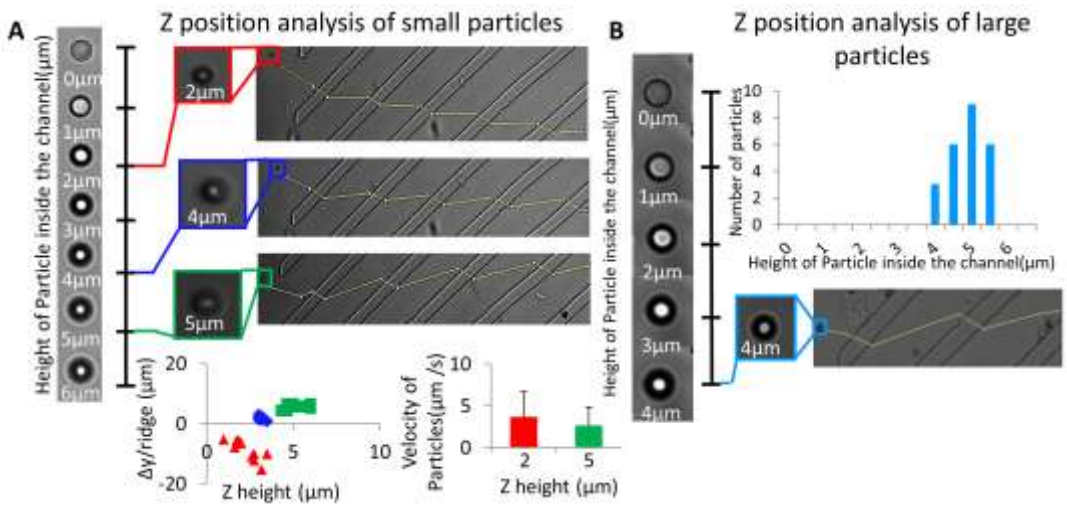

Figure 16 A) The scale on left is showing the reference images of 4 μm particles at different heights inside the channel .The trajectories on the right shows the 4 μm particles at different height which is determined by comparing it to the reference scale on left.

To address the deficient enrichment of larger particles, we demonstrate that there exists a z-position dependent phenomenon which leads to dispersity of smaller particle trajectories. As shown in Figure 16 A the smaller particles (4 μm diameter) entering the ridged part of the channel can arrive at different vertical positions as determined from out-of-focus images acquired at a constant focal plane. Hence smaller particles at different z-positions, as indicated by different color markers (red for 2 μm, blue for 4 μm, and green for 5 μm heights) move in either positive or negative y-direction trajectories. In contrast, Figure 16 B shows that larger particle (7 μm diameter) entering the ridged part of the channel uniformly remain in focus at same vertical height and move in the positive y-direction. The histogram of large particle heights in Figure 16 B shows that unlike the smaller 4 μm size particles, most of the larger 7 μm particles enter the ridged channel at same height due to steric hindrance of the ridged features. Figure 16 B (bottom left figure) shows the plot between the Δy / ridge and the diameter of bright diffraction ring, a surrogate

for the height of the particle inside the channel using the technique described previously [125]. That particles of different heights move with different transverse trajectories results from the vortex flow fields created by the diagonal ridge, such that the fluid at the channel center is transported in the net positive y direction, whereas the fluid located near the vertical channel walls moves in the negative y direction as shown by computational fluid dynamics simulations shown in work .[126] The particles at different z-positions not only move in different directions but also with different speed (Figure 16, bottom right), as is expected from the simulated height-dependent velocity gradient[126]. This effect is harnessed to create the separation among particles with different z positions.

2.5.2 Conclusion

Based on experimental data we demonstrate that there exist a z position dependency on particle lateral position and by controlling z position of the particles we can substantially increase the purity of sorted sample.

CHAPTER 3. SIZE BASED SORTING

3.1 Introduction

Based on the analysis of trajectories in Section 2.4 and size sorting results in Section 2.5, in this chapter we propose, design, fabricate and test a novel improvement to microfluidic sorting devices that uses three-dimensional focusing of the sample to a position that optimally amplifies the size-dependent trajectory differences of differential secondary flows. The result is an increase in the purity of size-sorted particles in comparison to unfocused flow. Our simulated and experimental data reveal for the first time that positioning particles in three-dimensional space can be used to better leverage the differential lateral movement of particles with different sizes as they flow in microchannels with transverse secondary flows, or possibly to improve positioning of particles with inertial channels with multiple equilibrium positions. This technique performs inexpensive, continuous-flow, high throughput clog free size based sorting of millions of particles/cells in a minute without any pre and post-processing. We have also demonstrated high throughput isolation with high recovery of white blood cells from human blood.

3.2 Methods

3.2.1 Microfluidic device fabrication

The microfluidic devices with different gap size were fabricated by replica molding Polydimethylsiloxane (PDMS) (Sylgard 184 Dow Corning Corp) on a permanent mold as described in chapter 2.The separation device has two sets of dimensions: 5.5 mm channel length and 560 μm channel width and 25 ridges and 2.5 mm channel length and 317 μm

channel width and 11 ridges. All devices have 22 μm channel height. The ridges are 20 μm wide and distance between two consecutive ridges is 180 μm. The ridges are at the top of the microchannel and are inclined at either a 30 or 45 degrees.

3.2.2 Sample preparation

Spherical polystyrene particles of 2.19, 4, 7.06 and 9.94 μm diameters (Bangs Laboratories Inc.) were used in the flow experiments. Dispersions were prepared in phosphate buffered saline (PBS) solution with a concentration of approximately $2X10^4$ particles/μL. To prevent bead adhesion, 0.01% v/v Tween 20 was added to flow media. For white blood cell separation, fresh human blood was withdrawn from healthy donors using protocols approved by the Georgia Institute of Technology Institute Review Board[103]. Blood samples were collected in citrate coated vials and used immediately after collection. The blood sample was diluted 1:10 in PBS before separation experiments.

3.2.3 Experimental setup

Same setup as described in chapter 2 and Figure 7 was used. Both x-y positions of particles were collected as well as the vertical position of the particles using an out-of-focus tracking algorithm developed previously [127]and explained in chapter 2.In order to accurately capture the cell trajectories with sufficient accuracy to determine the vertical position, we operated the high speed camera at a minimum of 3000 frames per second with a minimum resolution of 640 by 480 pixels for all videos and images. Separated particles and cells were collected at the outlets and were analyzed with an Accuri C6 flow cytometer (BD Biosciences). Purity of leukocytes is determined using the antibody cocktail - anti

CD45 –APC, anti CD61-PE, and anti CD235a-FITCI (GlycophorinA) from Biolegend, following manufacturer's protocols.

3.2.4 Finite element simulation

Finite element simulations were performed using COMSOL Multiphysics software (COMSOL Inc., Burlington, MA). Simulations were performed for channel widths of 317 and 560μm and ridge inclination angles of 30 and 45 degrees. PDMS was selected as material of interfacing structure. Sample to vertical sheath flow rates ratios of 0.22, 0.71 and 2.3 were used in the simulation to determine their effect on sample vertical confinement. The flow profiles in the channel were obtained by solving the Navier-Stokes equations for incompressible fluid using Fluid-Structure Interaction physics. At the outlet, the pressure was set to zero with no viscous stress on the boundary. Due to low Reynolds's number of fluid, it was assumed that the suspended particles would follow the fluid streamlines.

3.3 Results and discussion

3.3.1 Modelling with finite element methods

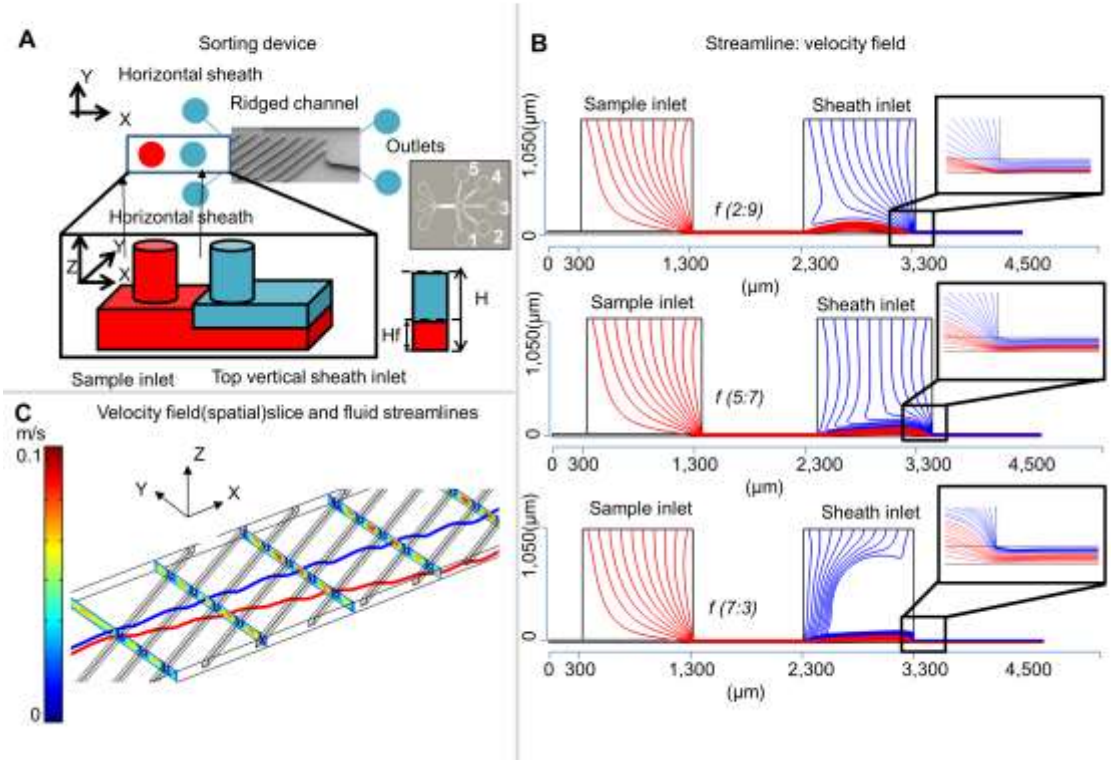

Figure 17 A) The proposed device to control the z-position of the particles as they enter the ridged channel using vertical sheath. H and Hf are the heights of the channel and focused streamline respectively. B) COMSOL simulations for different sample to sheath flow rate ratio (f). As the vertical sheath flow rate increases the sample flow streamlines are pushed down. C) COMSOL simulations show the velocity field under the ridge and the lateral deviation of streamlines as they enter the ridged part of channel at different heights.

.

We have used COMSOL to study the effect of vertical sheath on streamlines entering the ridged microchannel. Figure 17 A shows the schematic of the improved device.

There are four inlets: two of them are for horizontal sheath focusing and the remaining two are for sample and vertical sheath focusing.

3.3.1.1 Inlet design

The focused simulated streamlines at different *f* (*f* is the ratio of sample to vertical sheath flow rates) are shown in Figure 17 B. We have made the point particle assumption for theses simulations and have assumed that the particles are following the streamlines. The results indicate that as we decrease *f*, the focused sample streamlines are pushed at the bottom of the channel. While optimizing the inlet design we looked at the critical parameters including distance between the sample and vertical sheath inlets and their alignment as the former can build up the negative pressure from vertical sheath to sample inlet when *f* is decreased and can push the particles back into the inlet sample which affects the throughput of the device as shown in Figure 18 The accurate alignment of the sample and vertical sheath inlets is important for the efficiency of the device so that no particle could escape the vertical sheath pressure due to inlet misalignment. Figure 17 C shows the simulated streamlines at different heights in the device which also confirms that vortex created by diagonal ridges alter the lateral position of streamlines depending on their initial z position before they enter the ridged part of the channel.

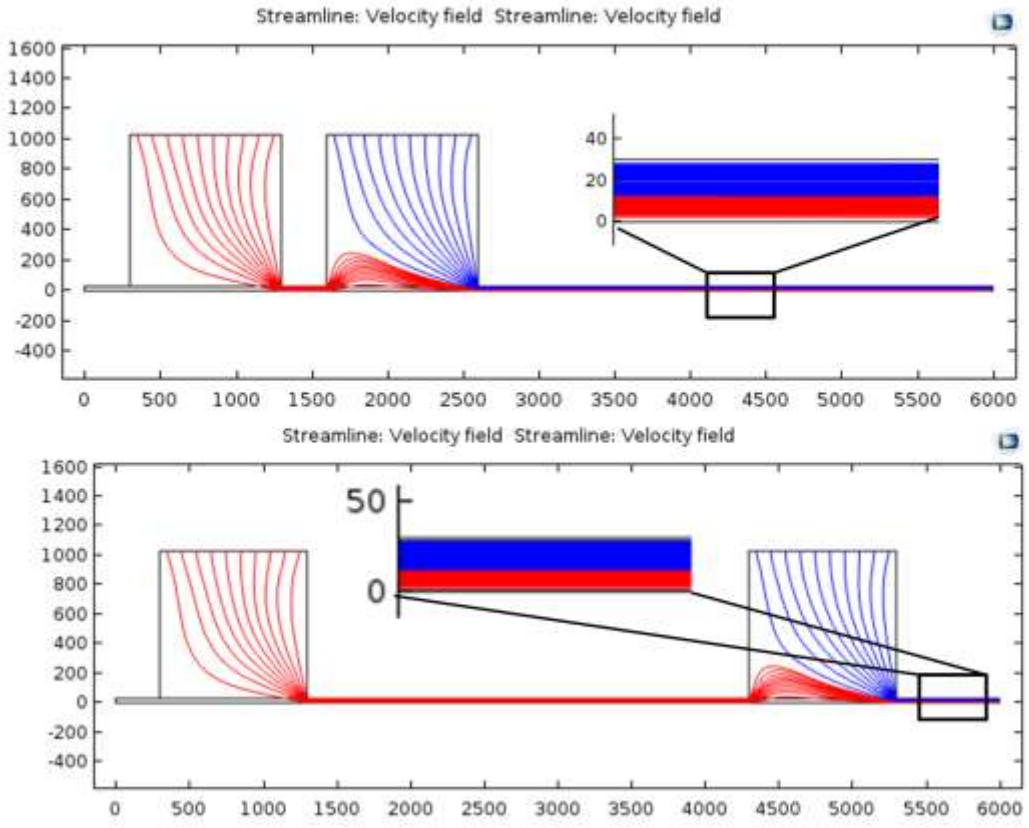

Figure 18 COMSOL simulations showing when distance between the sample and vertical sheath inlets is changed from 300 to 3000 µm, there is no change in the vertical focusing of sample and no back flow is observed.

A couple of horizontal sheath inlets inclination angle designs were also simulated as shown in Figure 19 and the inclination angle of 45 degree was selected to avoid sharp edges (as in case of 90 degree) in order to avoid bubbles during flow experiments.

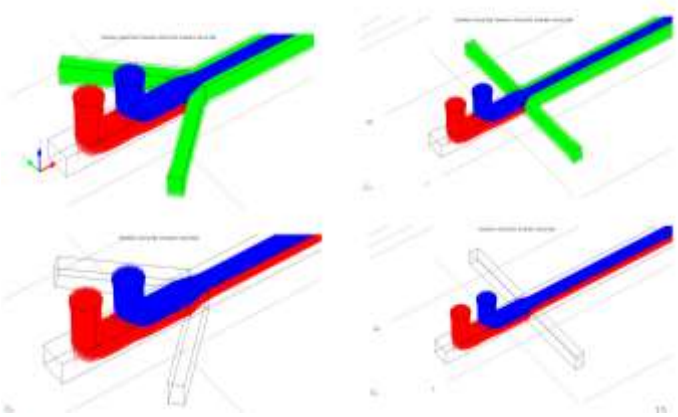

Figure 19 Effect of horizontal sheath inlet inclination angle on vertically focused streamlines.

We have selected 2000 µm distance between sample and vertical sheath inlets as it would be difficult to punch inlets with biopsy punches with smaller distances. The diameter of inlets is selected to be 1000 µm based on commercially available biopsy punches.

3.3.1.2 Ridge design

The aim of this study is to sort blood cells based on their size. Since platelets size range from 2-3 µm ,RBCs 6-7 µm and WBCs >8µm ,we have designed devices with two gap size of 10 µm and 8 µm.The former is used to sort WBCs from RBCs plus platelets in blood. The latter is designed to be used to sort RBCs from platelets from the sorted heterogeneous population of RBCs plus platelets (sorted by 10 µm device). For this study we have optimized our device design for channel width and inclination angle of ridges for a given channel length and number of ridges.

Figure 20 Oscillation of small particles in wide channels.

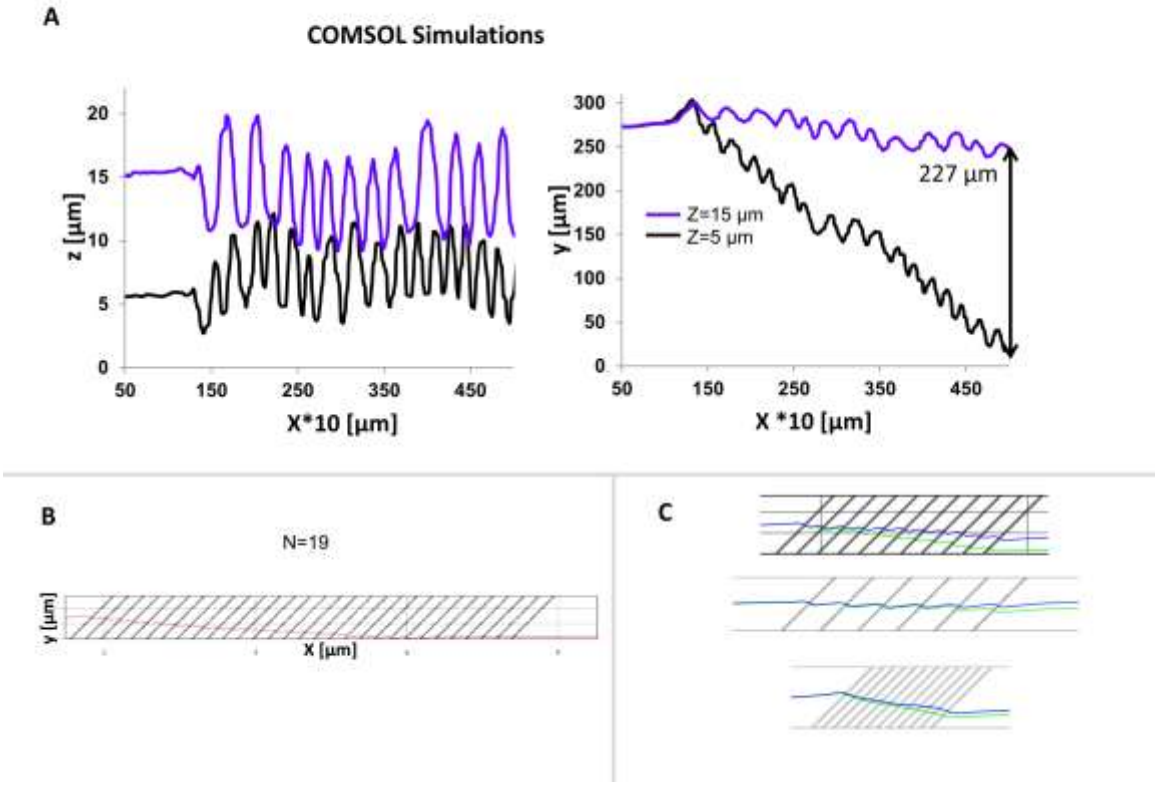

Figure 21 A) Showing the simulated streamlines at different z positions. B) Device length and number of ridges optimization for a given width. C) Showing interdependency ridge frequency and distance between them for a given inclination angle. Blue (Z=15 µm) and Green (Z=3.5 µm).

Enrichment suffers due to a reversal of particle trajectories that occurs once particles reach the channel walls for an un-optimized design, as shown in Figure 21. This effect is due to the circulating velocity vortex formed by diagonal ridges inside the channel, which can be solved by optimizing the channel length or number of ridges for a given

channel width to avoid the reversal of particle translation due to circulating flow at the edges of the channel. In Figure 21A simulated streamlines are shown at different heights of 15 and 5 μm and their lateral displacement difference is 227 μm. In order to achieve this displacement difference following values are used for device geometry: L= 4.5mm, W=560 μm, θ =30 degree, d=180 μm and N=17. This way we can select device geometry parameters for a desired lateral displacement difference through iterative simulation of Comsol model. In Figure 21B an example of simulated streamlines is shown where N= 17 and L=5mm for W=560 μm could be used to prevent oscillation of particles. Figure 21C shows the interdependency of ridge frequency and distance between them for a given inclination angle. The top figure shows the optimized θ=45 degree, N=11 and d=180 μm. The bottom two figures show that N= 6 with d= 380 μm and N= 12 with d=50 μm are not optimized channel geometry if we needed a W=560 μm and L=5.8mm with θ=45 degree to sort particles with high efficiency as can be seen from very small lateral displacement difference in the streamlines at heights blue (z=15 μm) and green (z=3.5 μm).

For width optimization, we have used channel widths of 560 and 317 μm with 20 μm width of ridge and distance between the two consecutive ridges is 180 μm and ridge inclination angle of 45 degree. The number of ridges are optimized to 25 and 11 for W= 560 and W= 317 μm respectively. For inclination angle study, 45 and 30 degree angles are used with 560 μm width. Simulation results for optimized channel length, width, inclination angle and number of ridges are shown with flow experiment data in section and have matched well with the experimental trajectories.

3.3.1.3 Outlet design

We have used two (only for adhesion study) and five outlet designs as shown in final mask design with serpentine outlets to prevent channel flow biasing by increasing the flow resistance between the inlet and outlet of the channel. Table 1 shows the variables for the final mold design in Figure 22

Table 1 Device design variables.

Device Design	**Width (μm)**	**Number of Ridges**	**Inclination Angle θ**	**d (μm)**
A	317	11	45	180
B	560	25	45	180
C	560	25	30	180

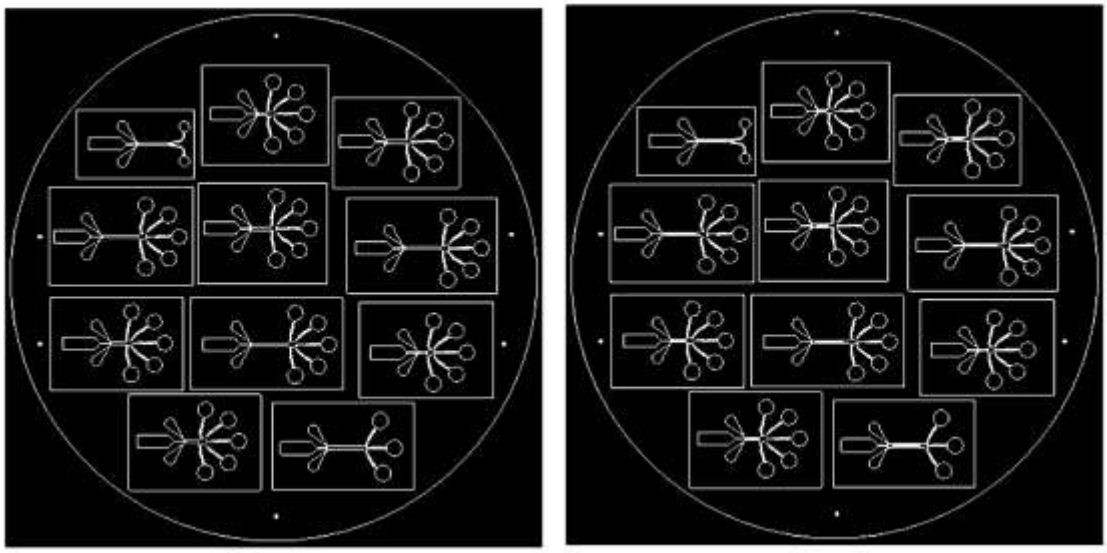

Figure 22 Final mask design without (left) and with (right) ridges.

3.3.2 Trouble shooting during device fabrication and flow experiment

We have used the same two step photo lithography to fabricate the final mask design (Figure 22). In this section we are going to list down the problems and troubleshooting we did during fabrication and flow experiments.

Although we aligned the mask and wafer using alignment marks during the mask aligning step of fabrication, our final mold was showing misalignment Figure 23 A. The reason for this problem was that there were liquid residues Figure 23 A (bottom) after etching and were not dry fully by nitrogen pump which led to the non-uniform spinning of second layer. One of the solutions is to use nitrogen for drying until you are sure that no residues are left by inspecting under the microscope or by hard bake for 60 s at 95 degree C.

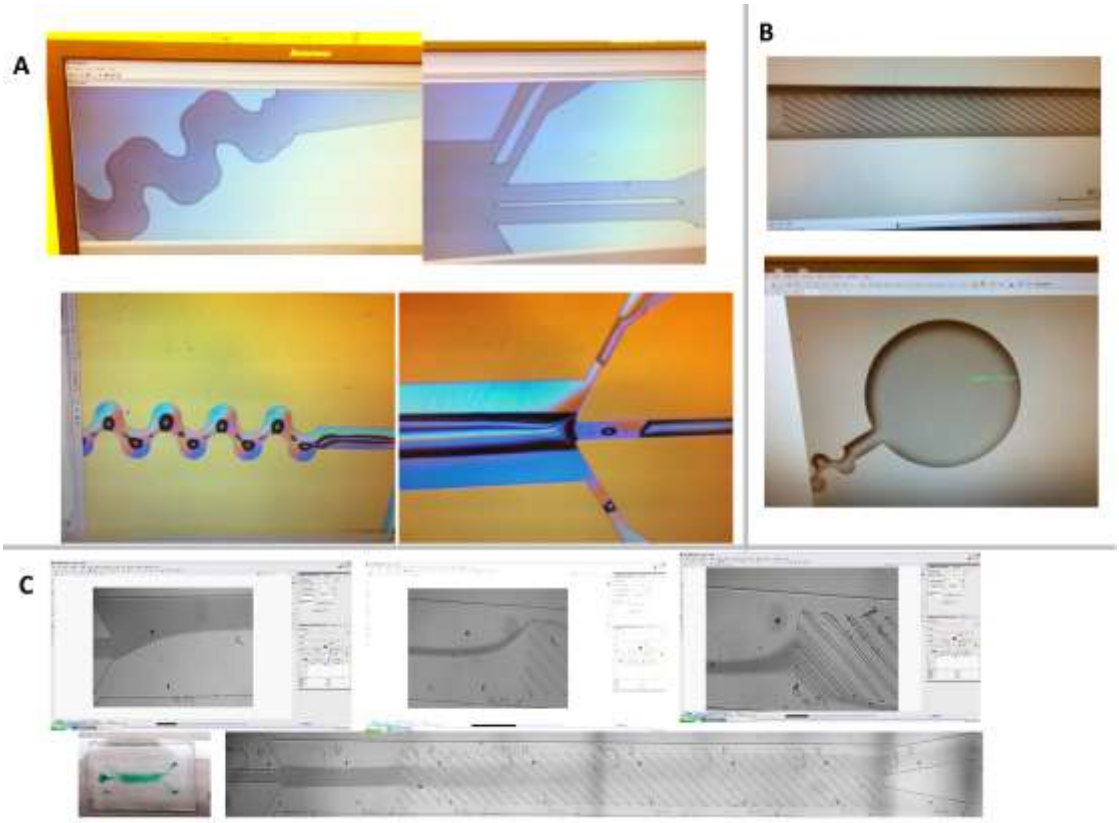

Figure 23 A) Showing misalignment in fabricated mold design (top). Liquid residues on final mold (bottom). B) Fabricated mold. C) Color dye used to optimize the flow rates for horizontal sheath.

During the flow experiments we have used color dye to optimize the flow rates for horizontal sheath as all particles/cells should enter the ridged part of the channel at lateral position of W/2. Figure 23 C. This also helped us to figure out if any of the inlets is blocked or if the syringe pumps working properly or not.

3.4 Results and discussion of flow experiments

The goal of vertical sheath is to position all small particles in the channel to the same equilibrium position such that they follow the same trajectory. To mathematically and experimentally determine the height of smaller particles (4 μm) entering the ridged part of

the channel after vertical sheath focus, we use theoretical model for predicting the height of two-dimensional hydrodynamically focused streams in rectangular microchannels (details can be found in Appendix A.2) and video microscopy to examine the vertical position of particles.

For video microscopy, still-frame images of particles are cropped from the videos recorded at different sample to vertical sheath rates of f= 0.9, 0.8 and 0.7. Figure 24 A explains the procedure we used to estimate the z position of particle inside the channel. Each particle in the channel is compared to two reference images for the cross correlation analysis at a vertical focal plane of 5 μm and 2 μm. The templates at different f are shown in Figure 24 B. The particles with square boxes in calculated cross correlation template in Figure 24 A show that they are at different z-position as compare to the z position of the reference image. The cross correlation coefficient calculated from the algorithm in Figure 24A is plotted in Figure 24 C and D. As the flow rate of vertical sheath is increased, the particles are positioned more narrowly to the 2 μm z-position. This result suggests increase in the enrichment of large particles with increased flow rate of vertical sheath results as more small particles confined to bottom of the channel move in opposite y-direction compared to large particles.

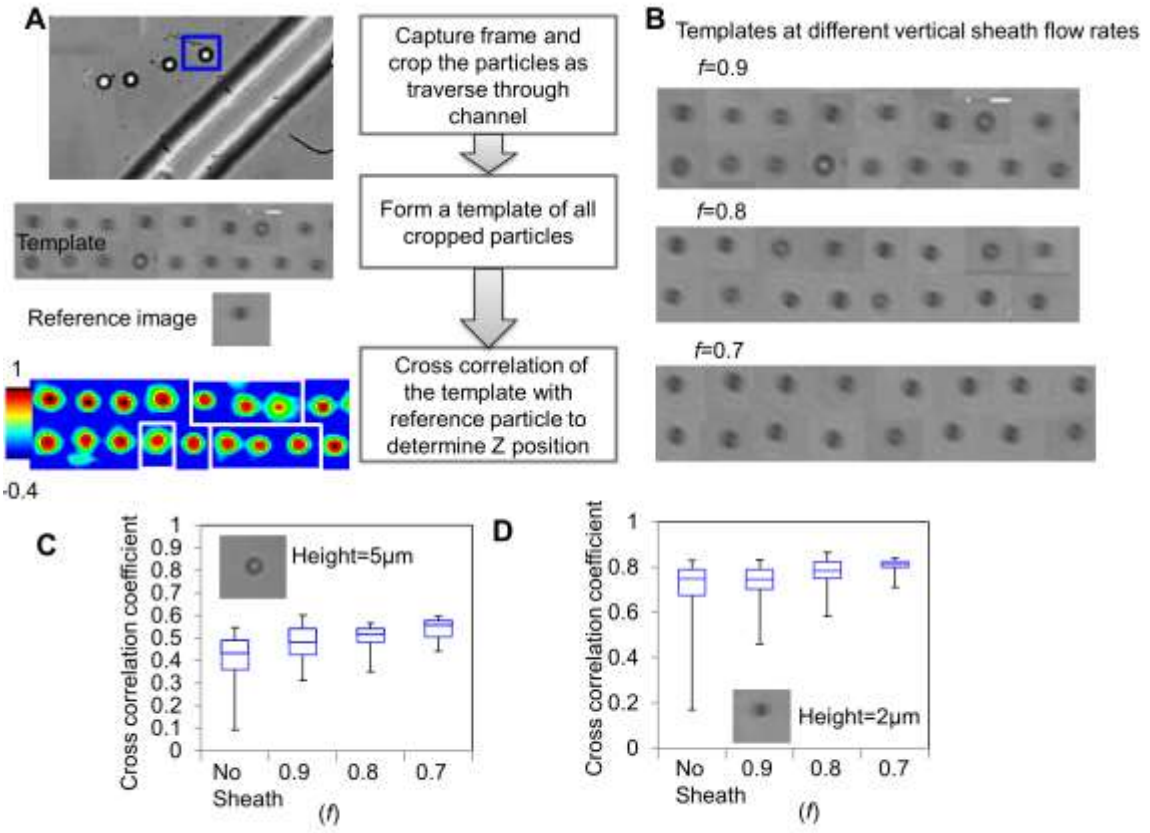

Figure 24 A) Algorithm showing how height of particles is estimated using cross correlation with a reference image at a known height. B) Templates showing the particles entering the ridged part of the channel at different vertical sheath flow rates. C) Cross correlation data estimating the height of the particles at different vertical sheath flow rates by comparing the templates in fig. 3b with reference image at height 5 µm and D) 2 µm.

2 and 7 µm particles were sorted in the width and angle optimization of the device. Gap size of 8 µm was used. Figure 25 A shows the enrichment factor of small and large particles at f =0.5 .The smaller width channel device has significantly lower enrichment as compare to 560 µm channel width device. This is due to the high wall lift forces acting on particles inside the channel and decreasing the relative size based lateral displacement. This can also be seen in Figure 25 B (experimental data) and can also be confirmed from simulated trajectories in Figure 25 C. Due to high inertial lift forces there is not much

lateral separation between 2 and 7 µm particle trajectories which led to the decrease in relative depth difference between two sized particles as they move along the channel, hence decreasing the efficiency of the device. The enrichment factors for different inclination angles show that 30 degree device has significantly high enrichment and almost 100 % purity for small particles. This can be explained looking at the experimental trajectories. Small and large particles are experiencing more opposite velocity field (as explained in Figure 16A (bottom right figure)) at same y position inside the channel in case of 30 degree device and hence are separated quickly with relatively high resolution. Also, this improvement is not angle dependent but frequency dependent because if we decrease number of ridges equals to encounter in 45 degree angle case , Figure 25C (very bottom) the lateral separation would decrease.

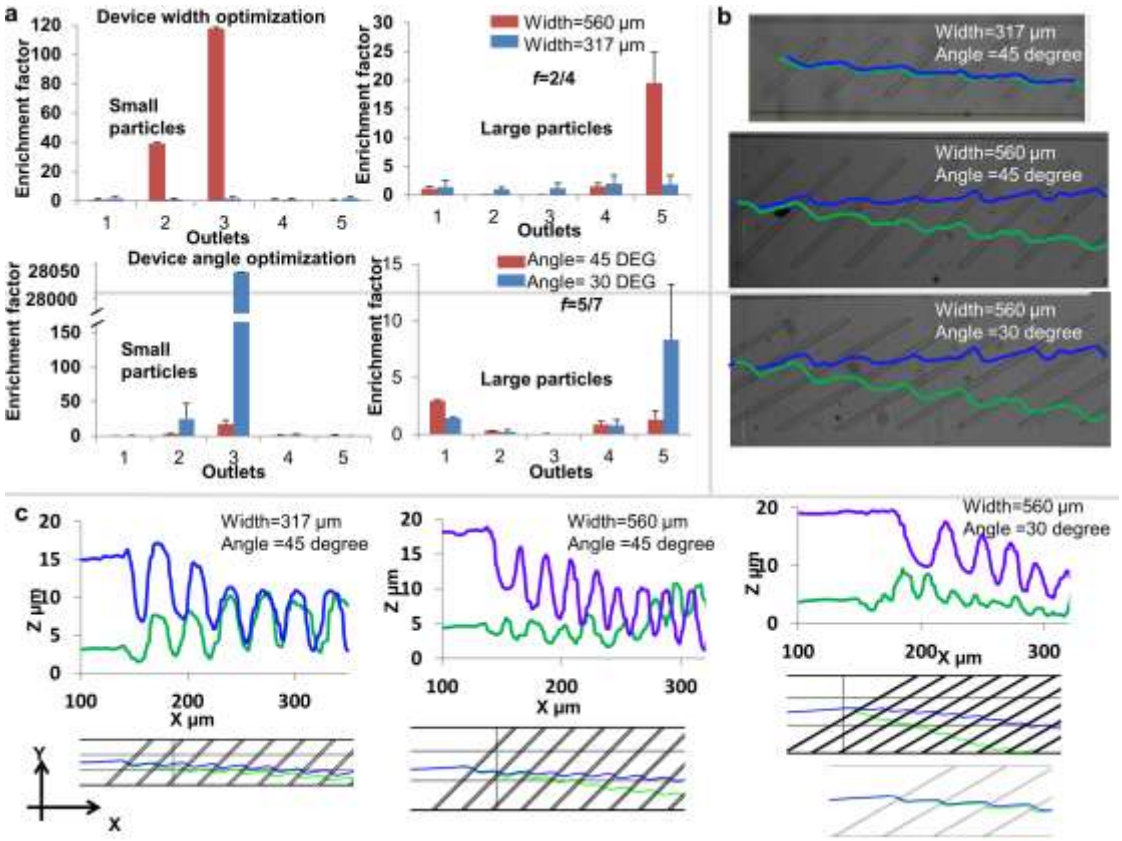

Figure 25 A) Enrichment factors for large and small particles for width (top) and angle (bottom) optimization studies. B) Experimental trajectories and C) simulated streamlines for design A, B & C.

We have also optimized the flow rate ratio for best device efficiency. The estimated height of small particles was calculated using the model described in Appendix A.2 for different flow rate ratios. The device design used was 560 μm in width and 45 degree inclination angle. The gap size was 8μm Figure 26 A shows the enrichment of small (117.8) and large (19.5) particles was highest at *f*=0.5.

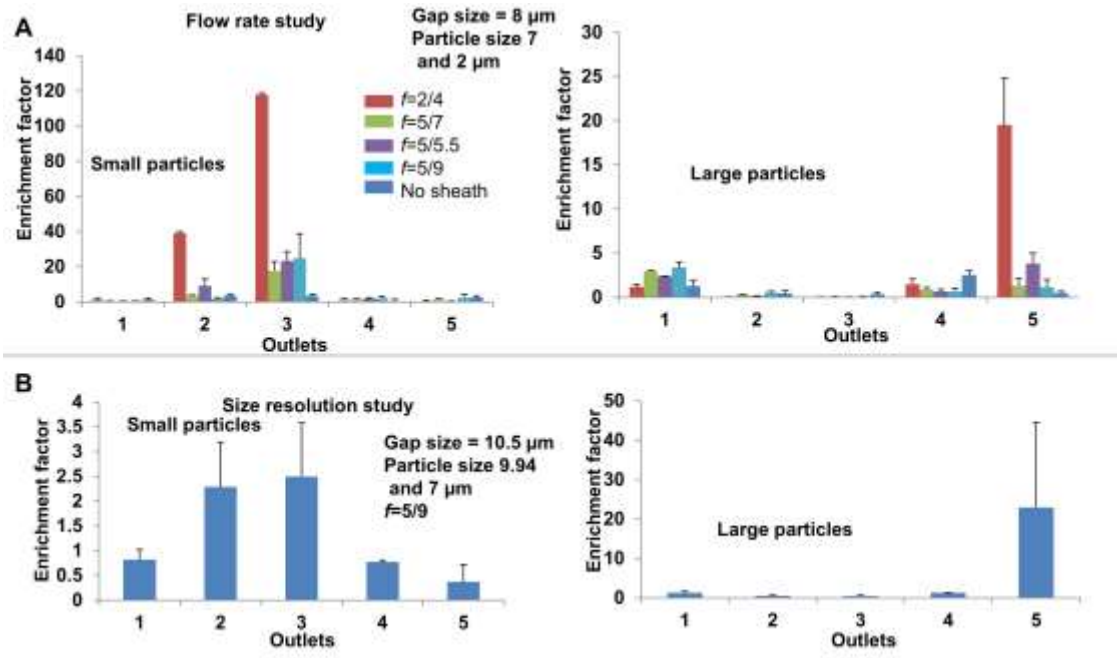

Figure 26 Small and large particle enrichment factors for A) Different flow rates and B) resolution study.

Figure 26 A shows the improvement of sorting enrichment with and without vertical sheath for 8 μm gap size, 560 μm width and 45 degree inclination angle. Small particle are enriched to 117.8 folds from 3.4 with purity of 99.9% and large particles are enriched to 19.5 folds from 2.5 with purity of 70% after incorporating vertical sheath focusing.

Resolution (Difference between particle sizes (µm) of proposed device was also studied using a 10.5 µm gap size device with 560 µm width and 45 degree ridge inclination angle. 9.94 and 7 µm particles were sorted with an enrichment of 23 and purity of 90% for large particles and 2.4 and 99 % for small particles as shown in Figure 26 B. The throughput of the device was 2.8 X 10 ^ 6 particles / min which is superior as compare to the recent studies Table 2. The details of flow rates used for different optimization studies are summarized in Table 3.

Table 2 Particle sorting comparison

Reference	**Mechanism**	**Throughput 100*particles/min**	**Enrichment (Large)**	**Enrichment (Small)**	**Resolution (µm)**
[128]	Inertial separation	1090	6.38	10000	5
[129]	Hydrodynamic filtration with no inertia	548	39	10000	6.9
[129]	Hydrodynamic filtration with no inertia	548	15.6	10000	5.1

[130]	Inertia and Secondary flow	186	17.9	41	4.4
[131]	Hydrophoretic	2.6	10000	10000	3
[132]	Hydrodynamic Filtration	200	46.6	124	7.3
OUR WORK	Vertical sheath, Hydrodynamics	28000	13	10000	5

Table 3 Estimated *Hf* for different studies

Study	**Sample Flow rate (ml/min)**	**Vertical Sheath Flow rate (ml/min)**	**Horizontal Sheath Flow rate (ml/min)**	**Qi/Qs**	H_f **(Calculated) µm**
Width Optimization	0.02	0.04	0.05	2/4	6.5

Angle Optimization	0.05	0.07	0.05	5/7	3.54
Flow rate Study	0.02	0.04	0.05	2 /4	6.5
	0.05	0.07	0.05	5/7	8.125
	0.05	0.055	0.05	5/5.5	9.285
	0.05	0.09	0.05	5/9	6.9
Vertical sheath study	0.02	0.04	0.05	2/4	6.5
Resolution Study	0.05	0.09	0.05	5/9	7.7

3.5 Depletion of WBCs (Leukapheresis)

Leukapheresis, is essential to reduce the white blood cell count in treating leukemic patients as well as to retrieve blood stem cells in patient with hematologic malignancies.[17-18] Removal of all leukocytes before performing a blood transfusion is essential to minimize transmission of cell-associated infectious agents (cytomegalovirus, herpes virus, human T-cell lymphoma virus), graft rejection rates and prevent febrile transfusion reactions[19]. For example depletion of T-cells from umbilical cord blood[20] increases efficacy of stem cell graft treatment[21-23]. Conventional macroscale WBCs sorting techniques include centrifugation, apheresis, chemical lysis and antibody based techniques, fluorescence-activated cell sorting (FACS) and magnetic-activated cell sorting (MACS).[32-39] Centrifugation is commercially available, easy to conduct and viability of fractionated blood cells is very high but it does not allow for high separation resolution, requires milliliters of blood for analysis which is not suitable for clinical settings and dedicated labs and trained users are pre -requisites. Microscale flow-based protocols such as FACS or solid-state immobilization and capture of cells using MACS offers advantages like high specificity, high-throughput, commercial availability but are expensive and cannot reliably handle small number of cells. The use of fluorophores and antibodies may affect cell fate and function[38] ,Alternatively, WBCs can be sorted from RBCs using microfluidics including hydrodynamics[129, 133], inertial sorting[130, 134], hydrophoretic[131], microfilter[135] , magnetic[136] and DEP[137]. The limitation of hydrophoretic, magnetic and DEP approaches is low separation throughput and in case of micro filters, it's not continuous. Whole-blood

approaches include cross-flow microfiltration[138], deterministic lateral displacement (DLD)[139] and WBC margination[140-141]. WBC margination provides a simpler separation approach based on a hemodynamic phenomenon, however, a major challenge arises from the dependence of WBC margination on channel geometry, hematocrit, flow rate, and RBC aggregation, which can restrict separation throughput and cause variability in separation efficiency. We demonstrate size based leukapheresis, which offers higher or comparable throughput with cutting edge techniques with high recovery and no pre or post processing of samples for analysis and isolation. The design used for this application has a gap size of 10.5 µm with channel width of 560 µm and ridge inclination angle of 30 degree.10.5 µm gap size was selected as red blood cells and platelets are in the range of 2- 8µm and white blood cells are >8µm .Hence, WBCs are sorted and collected at the top outlet. The WBCs were removed at a depletion of 87 folds and at a high throughput of 0.1X10^8 cells /min with recovery of 73% as shown in Figure 27.

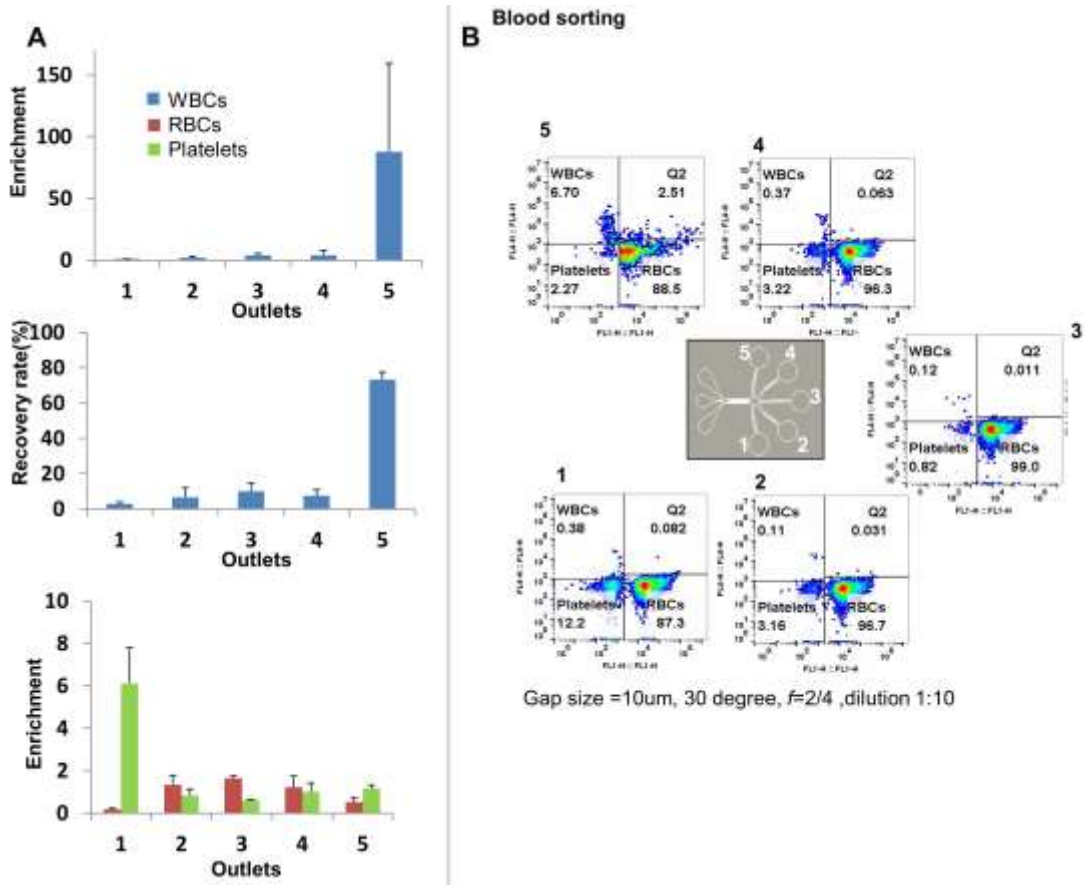

Figure 27 A) Enrichment factors for WBCs (top), platelets, RBCs (bottom), and recovery rate of WBCs (middle). Recovery rate is defined as the percentage of WBCs at targeted outlet to total number of WBCs collected. B) Flow cytometer characterization of WBC sorting.

Comparison with other cutting edge technologies can be found in Table 4. Flow cytometry data for centrifugation is shown in Figure 45 which shows that this device performs better to deplete more platelets from WBCs sorted population. Leukaphresis requires milliliters of blood to be processed in shortest time possible. We cannot process whole blood with high enrichment (less than 3-fold) and recovery rate as increase in blood cell concentration affect the vertical focusing of cells due to small channel dimensions.

Proposed solution to address this problem is to use either large foot prints or use parallel channels similar to previous studies[73], to increase throughput. Another assumption we made here we are not considering shape and thickness of RBCs. This may affect the purity of WBCs in large particle outlet as in case of resolution study we were getting >89% purity of large spherical beads where shape is spherical and thickness is not variable for small particles.

Table 4 WBCs sorting comparison.

Reference	**Mechanism**	**Throughput**	**Recovery**	**Enrichment**
		10^8 cells /min		
128	Hydrodynamic filtration with no inertia	0.1	80	3329.33
141	Deterministic Margination with no inertia	7.5	80	50
131	Hydrophoretic	0.00024	85	210
135	Filter with back flush	1.87	72	148
136	Magnetic	0.000415	97.4	
137	DEP	0.0085	92.1	7

[138]	Cross flow filtration	0.835	27.4	
[130]	Inertial separation	0.019	89.7	
[134]	Inertial separation	0.5	98.4	20
[139]	DLD	0.415	99	
[133]	Hydrodynamic filtration	0.1		29
[140]	Margination based separation	0.015	94	46
OUR WORK	Vertical sheath, hydrodynamics	0.1	73	87

3.6 Conclusions

We have described a novel microfluidic device capable of improved purity of size-dependent separation of particles by positioning particles at the optimal position in three-dimensional space to exaggerate the size-dependent trajectory differences. The unique aspect of this sorting design is the use of three-dimensional focusing of the sample to a position that optimizes the differential secondary flows. Using vertical focusing, we are able to separate 2 μm particles from 7 μm with a substantial improvement in enrichment of sorted number density in comparison to unfocused flow. We demonstrate 8-fold increase

of the purity of the larger particles (from 2.5 to 19.5–fold enrichment factor) and a 35–fold increase in the purity of smaller particles (from 3.4–fold to 117.8–fold). This is the first time that a device with 3D focusing has been reported to improve the purity of samples using size sorting. The proposed technology can further be improved for higher purity enrichment of particles by modifying channel geometry and gap size. It can also be integrated with separation techniques using different biomarkers like stiffness and viscoelastic deformation.

CHAPTER 4. ADHESION BASED SORTING

4.1 Introduction

This chapter will focus on the second part of this work, which is molecule specific adhesion based cell sorting. Cell surface molecular adhesions govern important physiological processes such as stem cell homing, immune modulation, and cancer metastasis. However, due to a lack of effective separation technologies sensitive to cell adhesion, it is challenging to specifically sort cells based upon molecular adhesion. While, label-free separation microsystems typically sort cells in a manner dependent on size, stiffness, and shape but do not provide sufficient specificity to cell type based upon molecular expression. While flow cytometry can offer higher specificity due to labeling of cells via antibodies, the separation is binary and does not allow greater functionality such as the fractionation of cells into subpopulations of high, medium, and low adhesiveness. We here develop a novel microfluidic approach capable of high throughput separation of cells based upon surface molecule adhesion. The ligand receptor pair used in this study is PSGL-1 and P-selectin. In this chapter, we will first discuss physiology of P-selectin /PSGL-1 interaction and therapeutic and diagnostic importance of PSGL-1. This will help to understand the commercial and scientific (in terms of understanding cell biology) importance of this study.

4.2 P-selectin and PSGL-1 binding

Selectins, including P, L and E belongs to family of cell adhesion molecules. [142] They mediate carbohydrate –protein interaction with specific ligands on leukocytes initializing rolling and tethering on endothelial cells. The physiological importance of cell adhesion mediated by selectin includes extravasation of leukocytes, homing of lymphocytes and infiltration or metastasis of malignant cells including leukemia and cancer cells [143].Of theses P-selectin is one of the important receptors expressed on activated platelets with about 10,000 copies/cell [144]and is stored in platelet R-granules, as well as endothelial Weibel-Palade bodies. P-selectin is type 1 transmembrane protein containing C-type lectin-like domains (CTLDs). The single CTLD in P-selectin, which binds sugars, is called carbohydrate recognition domain (CRD). The CRD is projected away from the membrane by a long, flexible neck, which contains an epidermal growth factor, EGF-like domain adjacent to the CRD, plus nine Sushi domains, a transmembrane domain and a short cytoplasmic domain.[145] After the activation of platelets, P-selectin is expressed on the platelet surface, which can bind to its receptor PSGL- 1, a dimeric membrane mucin on circulating leukocytes, as shown in Figure 28. Its CRD interacts with leukocyte glycoproteins, and its architecture, coupled with the glycan-binding properties of its CRD, results in weak tethering and rolling of leukocytes on endothelia, under shear flow conditions.

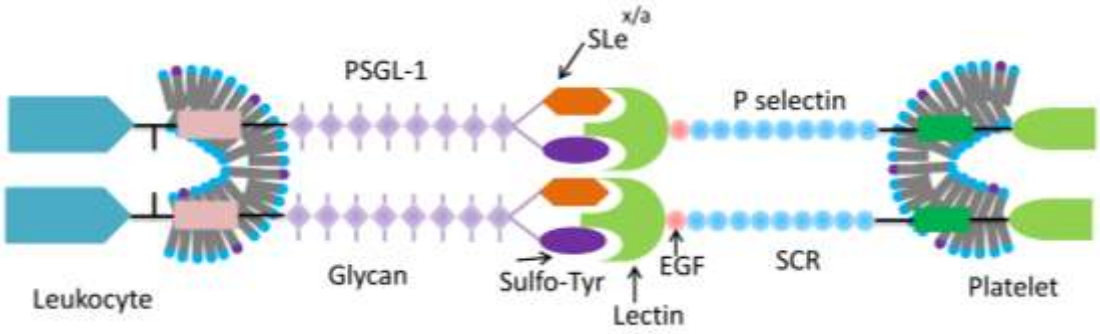

Figure 28 P-selectin and PSGL-1 structures and their binding.

The weak and transient selectin-mediated interactions is followed by strong and stable integrin-mediated interactions, which arrest circulating leukocytes and lead to their migration across the endothelium as shown in Figure 29[145-146].

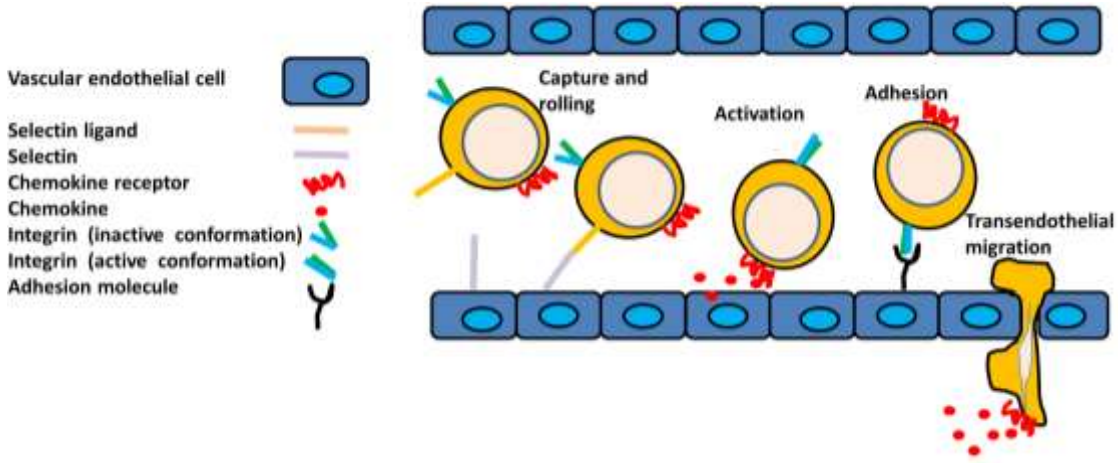

Figure 29 Interactions between selectin and selectin ligand form weak bonds that slow the flow of leukocytes, promoting initial cell capture and rolling.

4.3 Why P-selectin interaction with PSGL-1 is so important??

P-selectin glycoprotein ligand-1 (PSGL-1) is a glycoprotein found on white blood cells including T cells, endothelial cells and many other hematopoietic cells that can bind

to all three members of the selectin family through the N-terminus of the extracellular domain[147-149] but binds with the highest affinity to P-selectin [150-152]. This binding depends on post-translational modifications that are cell type and context dependent [153]. PSGL-1 contributes to both cell migration as well as play role in migration independent tasks and in monitoring immunity against various diseases.

4.3.1 Role of PSGL-1 in cell migration

PSGL-1 is known for its fundamental role in regulating immune cell recruitment to sites of inflammation. It is required in neutrophil migration into inflamed peritoneum [154], recruitment of CD8+ T cells into the inflamed colon [155]and of CD4+ T cells into responding lymph nodes [156]and inflamed retina [157]. It also helps in regulation of localization of macrophages, dendritic cells, and B cells in the lamina propria at steady-state [158]. Platelets also utilize PSGL-1 to adhere to vasculature [159], suggesting that its importance in pathogen clearance. One of the examples involves PSGL-1/P-selectin interactions, crucial for neutrophil recruitment and host defense against Salmonella typhimurium [160].

4.3.2 Facilitating inhibition/promotion of leukocyte response

PSGL-1 contributes to control of Streptoccus pneumonia by promoting phagocytosis by neutrophils through binding to the capsular polysaccharide and cell wall autolysin, LytA[161]. On the other hand, Enterovirus 71 has been found to utilize the selectin-binding domain of PSGL-1 as a primary receptor to infect leukocytes, and this supports viral replication. [94]These examples suggest that PSGL-1 can be directly targeted by bacteria and viruses to promote or inhibit leukocyte responses.

4.3.3 Migration-independent functions of PSGL-1

In Myeloid cells PSGL-1 inhibits proliferation of human hematopoietic stem cells (HSCs) in response to ligation by P-selectin or anti-PSGL-1 antibody in vitro.[162] In human dendritic cells (DCs), where engagement by P-selectin or anti-PSGL-1 induces the expression of genes which are associated with immune inhibition, and promotes their ability to induce regulatory T cells in vitro.[163] Neutrophil adhesion is up regulated by PSGL-1 ligation in the absence of chemokine.[164]

4.3.4 Role of PSGL-1 in T cells

It has been reported that PSGL-1 on T cells dampens TCR signals, limits survival of effector T cells, and promotes immune inhibitory receptor expression, there by supporting establishment of exhaustion in viral and tumor models. PSGL-1-deficiency enhances T cell anti-tumor immunity to melanoma. Multi-functional anti-viral T cells with PSGL-1 deficiency promotes viral control and T cell survival is reported to be increased in PSGL-1 deficit T cells after chronic virus infection[153, 165].

4.4 Material and methods

4.4.1 Immobilization of protein

We will first briefly discuss the pros and cons of available protein immobilization surfaces and techniques and which one is suitable for our work. Starting with immobilization surfaces, silicon and glass surfaces has been used for decades because of mature micro fabrication industry mostly in inorganic microfluidics and coated with metals

for applications like electrochemical analysis.[166] For better chemical resistance PMMA [Poly (methyl methacrylate)], PS (polystyrene), and COC (cyclic olefin copolymer) have been used. Paper has been used for point of care devices due to low cost, simple assay visualization, and simple reagent immobilization.[167] PDMS (polydimethylsiloxane), a silicon-based organic polymer that has popular for decades because of its low cost, rapid and prototype-friendly fabrication and optical transparency. PDMS offer unique advantages for a microfluidic platform which includes 3D structures inside microchannel for higher protein capture capacity,[168-169] resulting in improved immunoassay sensitivity or enzyme conversion rates. Due to transparency it makes optical imaging possible. In contrast to rigid substrates such as silicon and glass, microfluidic actuators such as valves and pumps can be readily formed in a microdevice[170]. Irreversibly sealing with glass can be formed by PDMS to make microchannels using plasma treatment. Multiple layers of PDMS can be stacked yielding multifunctional microfluidic devices. Drawbacks of PDMS includes not suitable for harsh environments needing robust packaging and toxicity. As related to protein immobilization, PDMS is hydrophobic in native form, so proteins tend to readily and nonspecifically bind to the surface but this problem can be easily addressed by blocking of the adsorptive surface before an assay is completed. Hence, due to advantages including optical imaging, low cost, ease of fabrication and allowing incorporation of 3D structure, PDMS is a suitable choice for this study.

Next, when selecting immobilization technique factors including sample matrix, protein property, buffer constituents, and assay performance metrics (e.g., sensitivity, reusability, selectivity, and reproducibility), conformability for high quality reproducible

assays,[171] orientation in specific immobilization ,density control so that steric hindrance from other immobilized protein is minimum are needed to be considered. More details can be found on immobilization strategies for protein microarrays,[171] enzyme immobilization inside microfluidic chips,[172-173] microfluidic immunoassays [172, 174].Molecular mechanism of protein immobilization methods can be categorized into physisorption, bioaffinity interaction, covalent bond Figure 30, and combinations of the three mechanisms.

In physisorption proteins are adsorbed to various surfaces via intermolecular forces such as electrostatic, hydrophobic, van der Waals, hydrogen bonding interactions, or combination .It is usually achieved by incubating surface with protein solution or through continuously flowing over it. Generally weak, relatively less stable than covalent and bioaffinity binding but no complicated chemistry and reagents are required.[175] In some cases, physisorption happens instantaneously (i.e., high kon) compared to covalent or bioaffinity bonds that usually requires a substantial incubation time. This technique has a wider choice of buffer system, compared to widely used covalent bonding through primary amines where popular amine-based buffers (e.g., Tris, glycine) cannot be used. If environmental factors like pH, ionic strength, temperature and surface conditions [176]are controlled accurate reproducibility of the protocol is possible. Bioaffinity adsorption exploits specific naturally existing binding phenomena. Bioaffinity interaction yields relatively stronger, highly specific, and oriented protein immobilization [171-172]but high cost, variable affinity, and short shelf life of antibodies make it unsuitable for point of care or disposable devices. Covalent immobilization involves surface activation via reactive

reagent reacts with amino acid residues on the protein exterior to form irreversible linkage[172]. Advantages include high and stable protein coverage. Disadvantages include reduced activity of proteins (by forming linkage on active sites), toxic reagents, complicated chemistry and long incubation time.[175]

Therefore, for this study simple, fast physisorption protocol has been used, as we need a cheap method for disposable micro devices.

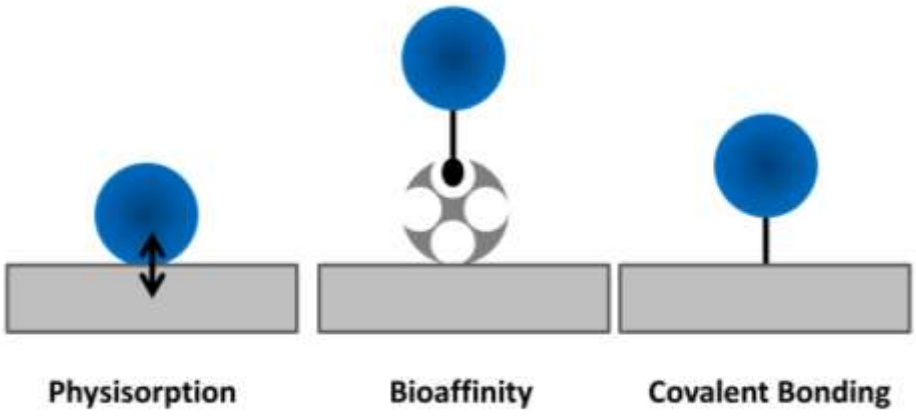

Figure 30 Protein Immobilization techniques.

4.4.2 Microfluidic device fabrication

Fabrication of adhesion based sorting device follow the same process flow and protocol as described in chapter 2 .We have designed the ridged microchannels to have gap sizes of 9.3 µm for Jurkat cells and 10.3 µm for HL60 cells, which imposes a cellular strain of 15 %. The channel width is 560 µm and length 3.8 mm. The ridges are 20 µm wide and distance between two consecutive ridges is 70 µm. The ridges are at the top of the

microchannel and are inclined at a 30 degree. We have used three and five outlet devices for this study.

4.4.3 Sample preparation and experimental setup

Jurkat cells (CRL-1990) and HL60 (CCL 240) were purchased from ATCC. Cells were cultured and maintained in RPMI-1640 medium (Sigma) with the addition of 10% FBS (Millipore Sigma) and 1% Penn strip. Cells were incubated at 37 degree C with 5% carbon dioxide. Recombinant human P-selectin was purchased from R&D Systems (Minneapolis, MN) and resuspended in PBS at (cp = 3 µg/mL). The assembled device is degassed in a vacuum chamber for 10 min, filled with P-selectin solution by pipetting, and then incubated at room temperature. After 3 hours incubation, the device was washed with 1% bovine serum albumin (BSA). Cells suspended in culture media at 0.5 × 10^6 or 1 × 10^6 cells/ml were flowed into the device at 0.0045, 0.045 and 0.09 mL/min using a syringe pump. A high speed camera (Phantom V 7.3 Vision Research) and inverted microscope setup was used as described in [127]. Following collection at outlets, cells were incubated at 37 degree C with blocking solution for 15 min and then incubated for 30 min with primary monoclonal antibodies and then, after wash with PBS, for 30 min with fluorescently labeled secondary antibodies at final concentrations of 30 and 50 µg/mL respectively. The concentration for antibodies was determined by running a titration experiment. Between primary and secondary antibodies incubation and after secondary antibody incubation and flow analysis, cells are washed with PBS. For detection of cell-surface PSGL-1, we used mouse anti-human PSGL-1 clone KPL-1 (Millipore Sigma). We used secondary antibody PE-conjugated goat anti-mouse IgG (Invitrogen). Solutions composed of primary and

secondary antibodies were pre incubated for at least 1 hr prior to incubation with cells. Cells were analyzed with flow cytometer (BD Accuri).Fluorescent imaging was used to check the degree of detachment of P-selectin after flow experiment. For this purpose, we used 1% FITC BSA (Millipore Sigma) as a blocking agent. In order to measure the activation of cells, antibodies, anti CD69-FITC and CD11b-APC (all purchased from Biolegends Inc.) were used according to manufacturer's manual. Samples were analyzed using BD Accuri flow cytometer. Expressions of CD69 and CD11b were compared for all the three cases of activation experiments.

4.4.4 Cell stiffness measurement with atomic force microscopy

We utilized atomic force microscopy to accurately verify the stiffness of cells. All cells were measured in suspended states after slight attachment to the surface. To measure cells in suspended state, a monolayer of poly-L-lysine (MW 300,000 Millipore Sigma) was grafted onto the glass slide substrate. This operation provided anchorage of the cell to the glass substrate while maintaining roundedness of morphology for cells and improved the cell stability during the AFM measurements. We carried out our AFM experiment immediately after the washing step and poly-L-lysine cell attachment treatment and all measurements were finished within 2 hours. We did not observe a change in measured stiffness during the course of these measurements. Measurements were conducted using a MFP-3D AFM (Asylum Research) attached to an inverted optical microscope (Nikon Eclipse Ti). A silicon nitride cantilever with a spring constant measured to be 37.1 pN/nm and a spherical tip was positioned above the center of individual cells before indentation. Prior work showed that the Young's modulus is a function of loading force and loading

rate [177]. The force-indentation curve was obtained for each measurement at a 40% strain and then analyzed with a Hertzian model for a spherical tip (Wavemetrics, IgorPro software routines) from which the Young's modulus values were calculated.

4.4.5 Fluid Flow Simulations

Finite element simulations of fluid flow were performed using COMSOL Multiphysics software (COMSOL Inc., Burlington, MA). Simulations were performed for channel width of 560 μm and ridge inclination angles of 30 degrees. PDMS was selected as the material of interfacing structure. The flow profiles in the channel were obtained by solving the Navier-Stokes equations for incompressible fluid using Fluid-Structure Interaction physics. At the outlet, the pressure was set to zero with no viscous stress on the boundary. Due to low Reynolds number of the fluid, it was assumed that the suspended particles would follow the fluid streamlines.

4.5 Results and discussion

The sorting device shown in Figure 31A uses the flow of cells through a microchannel decorated with diagonal ridges and coated with P-selectin specific to PSGL-1. The bottom glass surface of the microchannel was also coated with P-selectin. For negative control, flow experiments were conducted without P-selectin incubation of the device. First, we examined the behavior of the device with and without P selectin. Figure 31 B shows the trajectories of Jurkat cells flowing through the device with (black) and

without (blue) P-selectin coating. The trajectories indicate that the adhesion force induced by ridges and P-selectin coated bottom glass surface on cells as they flow results in a net lateral displacement that distributes the cells at different y positions hence at different outlets based on the binding between P-selectin on device surface and PSGL-1 on cell surface. The cells flowing in the device without P-selectin follow the fluid streamlines, as no adhesion force is present in this case. The unique aspect of this sorting design is the use of optimized gap size Hg, defined as the distance between the ridge and bottom of the channel, to lightly squeeze the cells while flowing under the ridged part of the channel while offering a high surface area for specific interaction between the cells and ligand molecules coated on the ridges.

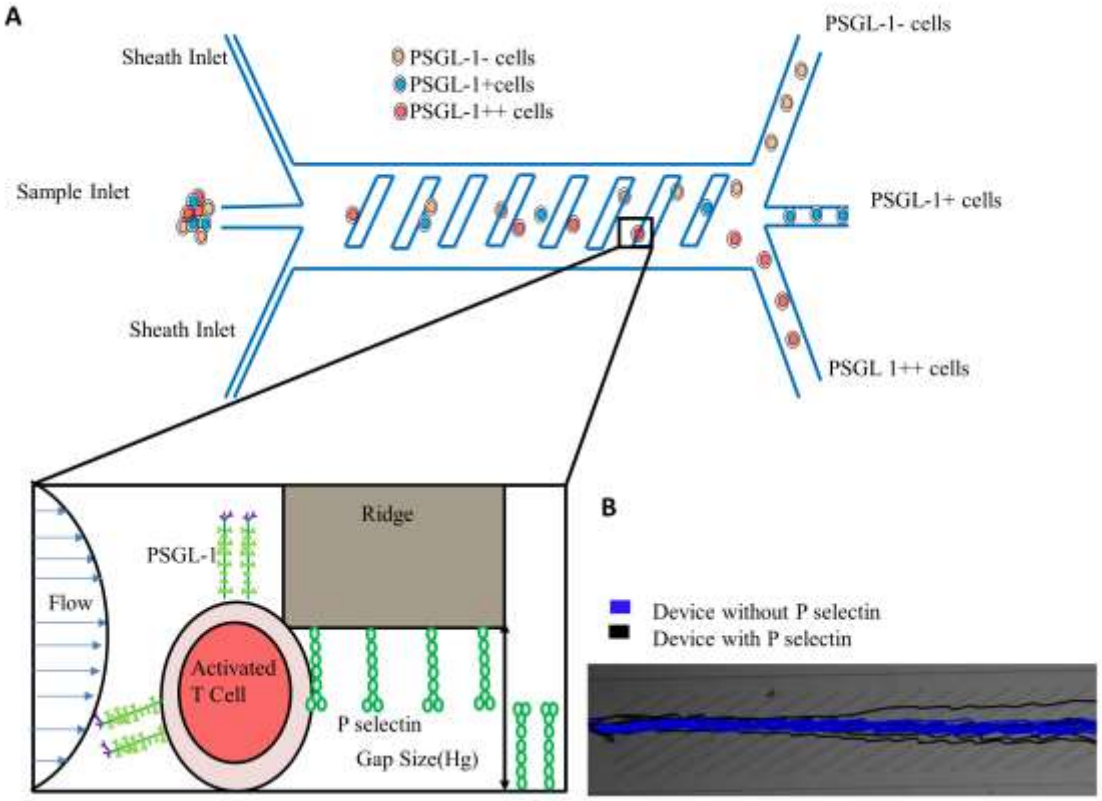

Figure 31 A) Adhesion based sorting device. The top figure shows sorting device consists of ridges and bottom surface of the device coated with cell adhesion molecules. The bottom enlarged figure under the ridge shows the device working mechanism. As the cell flows under the ridge it is slightly squeezed to increase the surface area between the cell ligand and the adhesion molecule on coated ridge to enhance adhesion sorting efficiency. B) Shows the trajectories of Jurkat cells flowing through the device with (black) and without (blue) P-selectin coating. The trajectories (black) indicate that the adhesion forces on cells when they flow under the ridge results in a net lateral displacement that distributes the cells at different y positions hence at different outlets based on the binding between P-selectin on device surface and PSGL-1 on cell surface. The cells flowing in the device without P-selectin follow the fluid streamlines, as no adhesion force is present in this case.

Next, we examined the behavior of HL60 and Jurkat cell lines using the proposed device. The gap size was optimized so that it was large enough for biomechanical features, such as stiffness and viscoelasticity, not to dominate the cell separation mechanism. In

these flow experiments we used 9.3 μm gap size for Jurkat cell sorting as our lab has previously reported the optimized gap size for stiffness separation of Jurkat cells is 8 μm[75]. 9.3 μm gap size is small enough to lightly squeeze Jurkat cells as they have 11 μm diameter. For HL60 cell study we used 10.3 μm as they are 12 μm in diameter. The ridges were designed to be 20 μm wide which is larger than the diameter of the cells used in this study and hence does not affect the device sorting efficiency[49]. P-selectin was used as a cell adhesion molecule which is a specific receptor for PSGL-1 (P-selectin glycoprotein ligand 1) ligand found on surface of HL60 and Jurkat cells and shows binding to P-selectin coated surfaces [49, 178]. To characterize the sorting of different cell types by the device we examined cells after treating them with primary and secondary antibodies as described in methods and using flow cytometry.

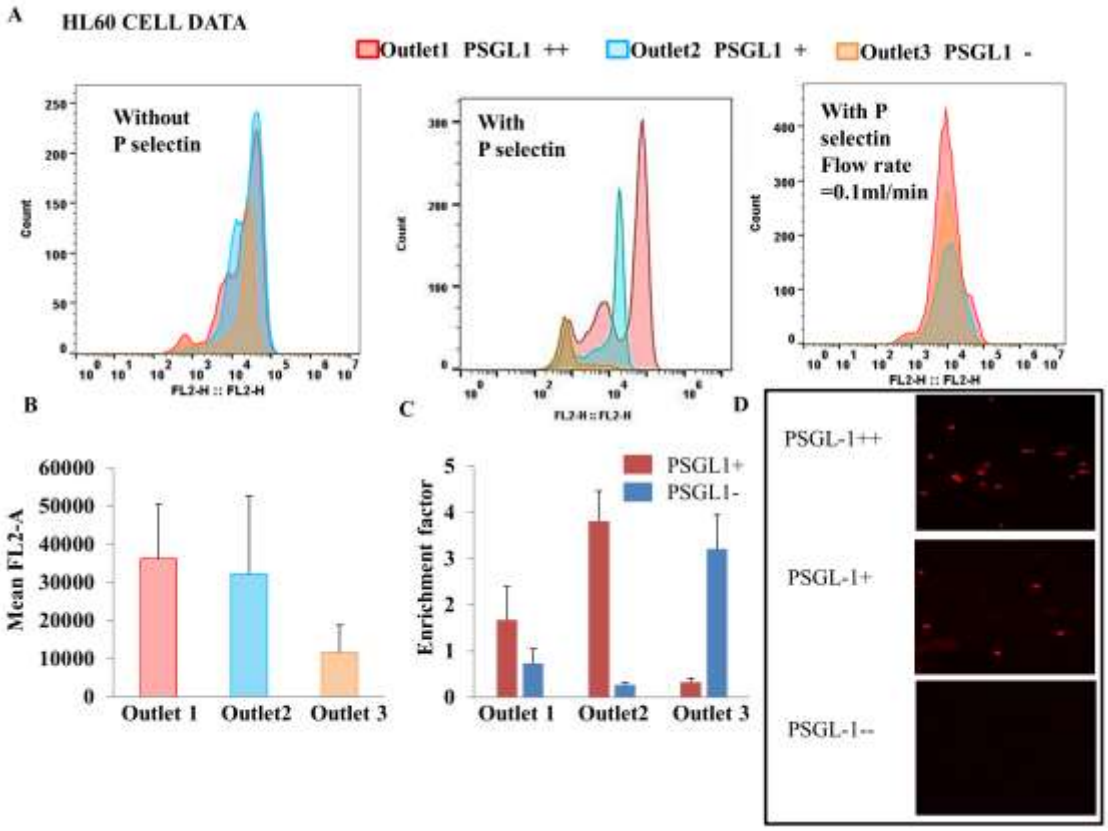

Figure 32 A) Shows the flow cytometer data for HL60 cells collected at different outlets showing a peak shift in their mean fluorescent values only in the case when device is coated with P-selectin and flow rate is 0.045ml/min. The second and third top figures show the data with no P-selectin coated device (flow rate 0.045ml/min) and with coated P-selectin device but flow rate of 0.1ml/min. There is not any significant shift in the fluorescent peak values for the last two cases. B) Shows the mean fluorescent values at different outlets, C) shows the enrichment factor and D) shows the images of cells at outlets all for P-selectin coated device and 0.045ml/min flow rate case.

We are able to separate HL60 and Jurkat cells based on its expression of PSGL-1 ligand by using a single ridged channel coated with P-selectin. HL60 cells were flowed at 0.045 and 0.1 ml/min of flow rates in the device with P-selectin incubation and at 0.045 ml/min without P-selectin incubation. The flow cytometer data for outlets for the three different cases is shown in Figure 32 A. To study the impact of sample flow rate on

adhesion based sorting, we conducted experiments at a higher flow rate of 0.1 ml/min. For higher rates, we see the adhesion dependence of outputs faces an upper limit of flow rate we do not see any sorting of cells as shown in flow cytometer data in Figure 32 A (right). We have observed a peak shift shown in Figure 32 A (middle) for the case of 0.045ml/min with P-selectin incubation. This suggests that at high flow rates there is not enough time for cells to adhere with the coated surface and are distrusted in three outlets evenly. There is also a lower limit of flow rate as the whole device is coated with P-selectin and flowing cells at slow flow rates results in adhesion of cells to top surface or side of the ridges and affecting sorting efficiency due to these nonspecific bindings (Figure 48). Figure 32 B shows the fluorescent mean values of collected sample at different outlets for 0.045ml/min flow rate with P-selectin incubation (two way ANOVA and Ad hoc Tukey tests on the collected data were run and found out there is a significant difference in fluorescent mean values of three outlets). The flow rate utilized of 0.045 ml/min was substantially higher than used in other microfluidic label-free adhesion based sorting. We demonstrate 3.8 and 3.2-fold enrichment of PSGL-1 positive and negative HL60 cells respectively as shown in Figure 32 C. We have also used fluorescent microscopy to validate outlet characterization of our device as shown in Figure 32 D. The PSGL-1++ outlet in Figure 32 D shows more cells with secondary antibody attached to them, hence showing more PSGL-1 expression.

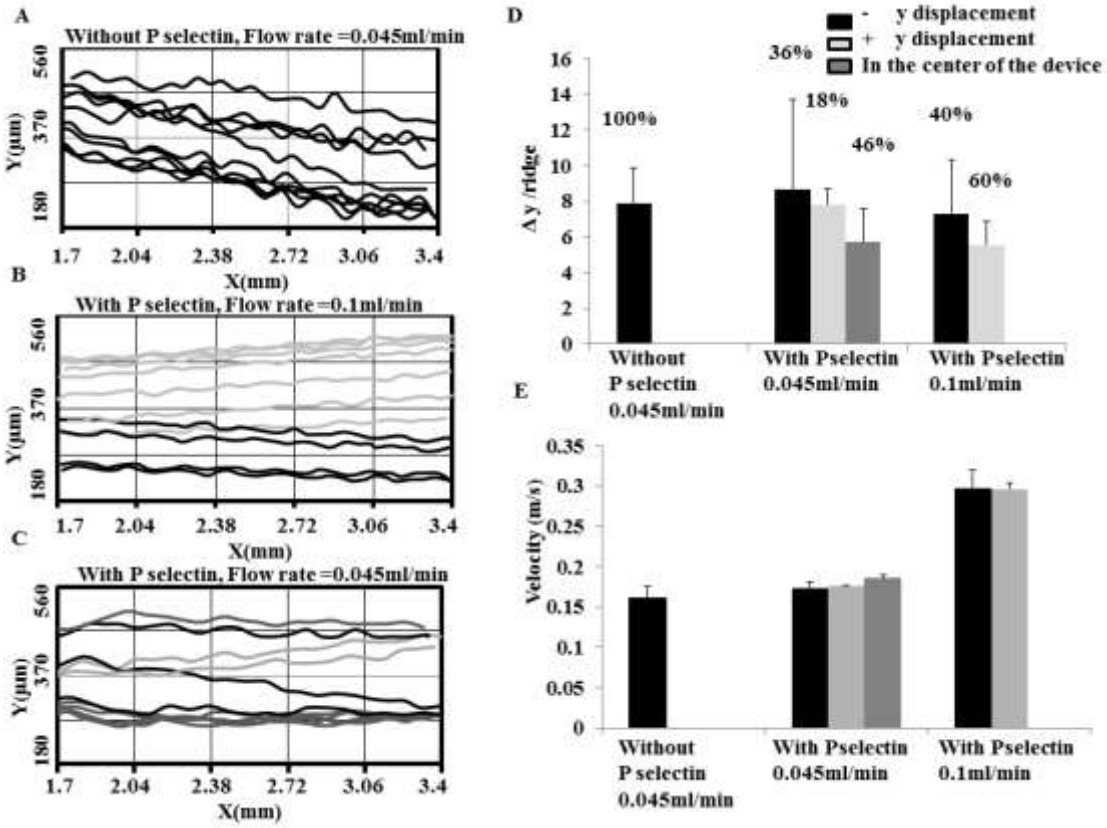

Figure 33 Trajectories with and without P-selectin incubated device at different flow rates and their Δy/ridge and velocity analysis based on data extracted from these trajectories.

Figure 33 analyzes the trajectory of HL60 cells with and without P selectin functionalization and at increased flow rates. In Figure 33D, the data from trajectories are extracted to determine the lateral displacement of cell flows between two ridges, defined as Δy/ridge. The trajectories for un-coated devices show displacement only in negative y direction whereas the P-selectin coated device shows displacement with a range of values, either positive, negative or in the middle of the device. Analysis of trajectories of cells at high flow rate of 0.1 mL/min for P selectin coated device in Figures 33D and 33E shows that 40% of the cells are dis-placed in negative y direction with 7.3 μm and 60% in positive

y direction with 5.3 µm Δy /ridge and at much higher velocities as compared to 0.045mL/min flow rate. This lack of enrichment at high flow rates (Figure 32A right) indicates hydrodynamic forces dominate adhesive forces, in part due to larger hydrodynamic forces and in part to in-sufficient time for cells to form adhesions with the coated surface. Therefore, low enrichment of cells based on adhesion is observed at a flow rate of 0.1 mL/min

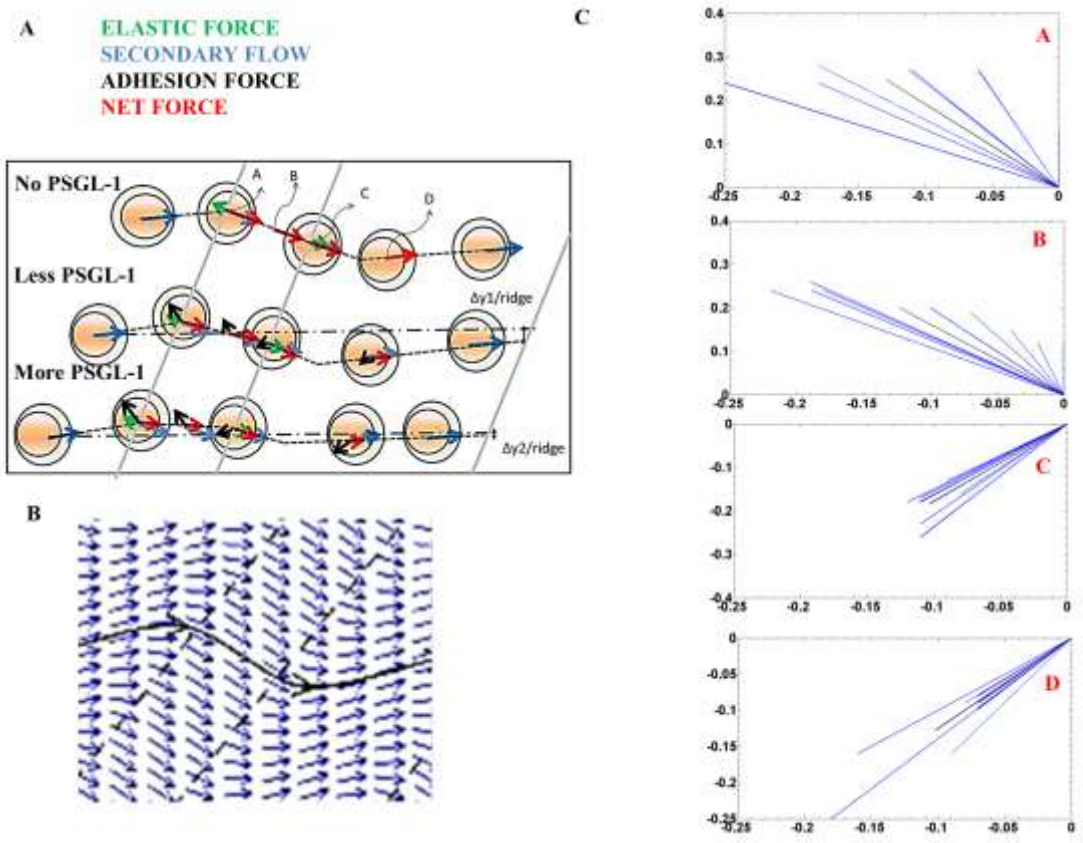

Figure 34 A) Force model explaining the direction of adhesion, elastic, secondary flow and resultant forces for cases without P-selectin coated ridges(top trajectory), with P-selectin coated ridges (bottom two trajectories). B) CFD simulations C) Adhesion force vector extracted from experimental data (trajectories) for cells at three different positions inside the channel as marked A, B, C and D in Figure 33 A. The average adhesion force vectors at different points are indicated in black.

The results in Figure 34 A shows the force model from our understanding of trajectories of cells (Figure 35), flowing through device with and without P-selectin. The adhesion force which is the only unknown is determined using vector addition .Cells propelled by fluid flow experience a secondary flow force (blue arrow) due to these diagonal ridges inside the microchannel and an elastic force [75, 179](green arrow). The direction of secondary flow is in positive y direction outside the ridge and in negative y direction under the ridge as shown in simulated data in Figure 34 B [75]. Thermodynamically, the elastic force is associated with the gradient of system free energy due to cell elastic deformation and, therefore, is in the direction perpendicular to the ridge. The elastic force has opposite directions when a cell enters and leaves a constriction. We have first calculated the elastic force, which is perpendicular to the ridge by vector addition, and using the resultant force from the trajectory of cell entering the device with no P-selectin. The secondary flow force is determined using drag force equation or CFD simulations. Elastic force that primarily acts at point A and C was calculated by vector subtraction of resultant force from secondary flow force in uncoated device. Using this calculated elastic force, we determined the adhesion force for the P-selectin coated device. By examining the second and third trajectories of cells entering the coated ridge in Figure 35 B, cells are experiencing an adhesion force in the upward direction at point A and B and in downward direction at point C and D, resulting in either a net positive or negative y displacement. On the other hand, cells flowing through the uncoated channel are following the fluid flow streamlines. The force model in Figure 34 A explains the working mechanism of adhesion based sorting. When the cells enter the ridge coated with P-selectin ,Figure 34 A second

and third trajectories, cells experiencing secondary flow force in negative y direction, adhesion force (black arrow) in positive y direction and very weak elastic force because of optimized gap size ,perpendicular to the ridge ,the net resultant force (red arrow) will be in positive y direction. Same is the case at point B but with less adhesion force. Now, when the cell leaves the ridge, the adhesion force is acting in negative y direction and secondary flow force has started acting in more positive y direction, the resultant force will force the cell to move in positive y direction but due to coated bottom glass surface the cell which are expressing more PSGL-1 would adhere to the bottom surface and experienced a more adhesive force (point D) and would move in net negative direction. As the cell expresses more PSGL-1, hence stronger adhesion force, the trajectory of cell will have lesser Δ y/ridge in + y direction as shown in Figure 34 A, third trajectory (Δ y1/ridge < Δ y2/ridge in +y direction). Hence, cells with more PSGL-1 experience less net positive lateral displacement as compare to trajectories of cells with less Cells flowing through the device without P-selectin coated ridges will move with the fluid flow streamlines. Since cells in the stream are located near the bottom channel wall with weak elastic force and no adhesion force they are transported by the circulating flow, created by ridges, in the negative transverse direction as shown in Figure 34 A top trajectory) and Figure 35 A and explained in Figure 36.

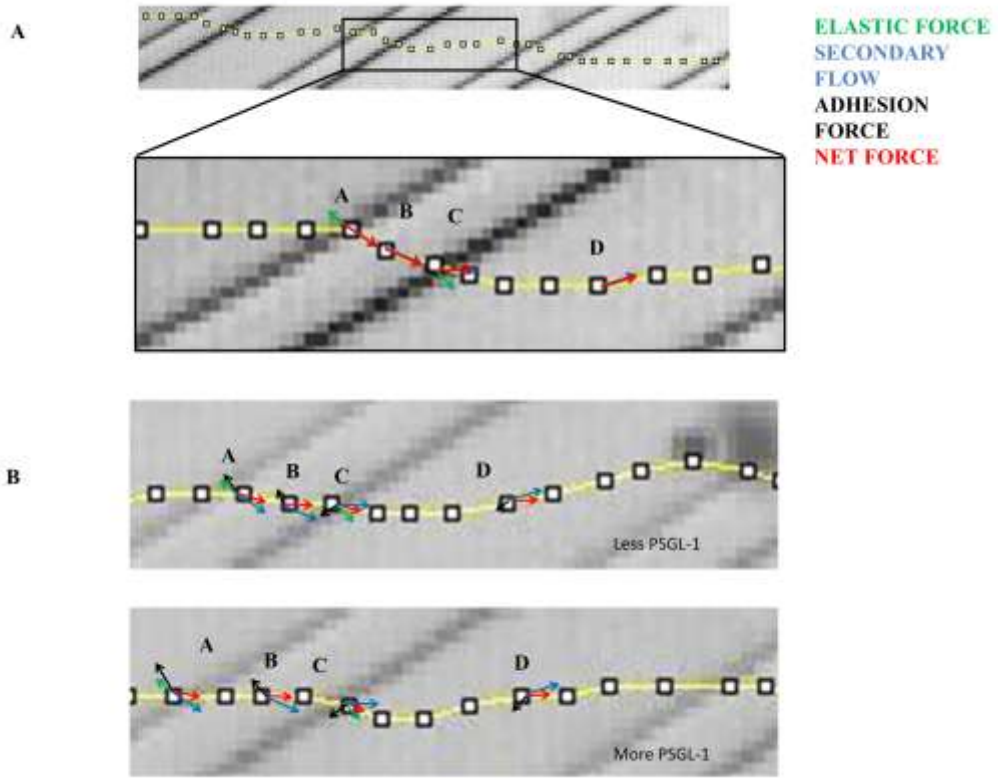

Figure 35 Adhesion force vector is determined from trajectories of cells from flow experiments. A) Shows trajectories of cells flowing with and B) without P-selectin coated device.

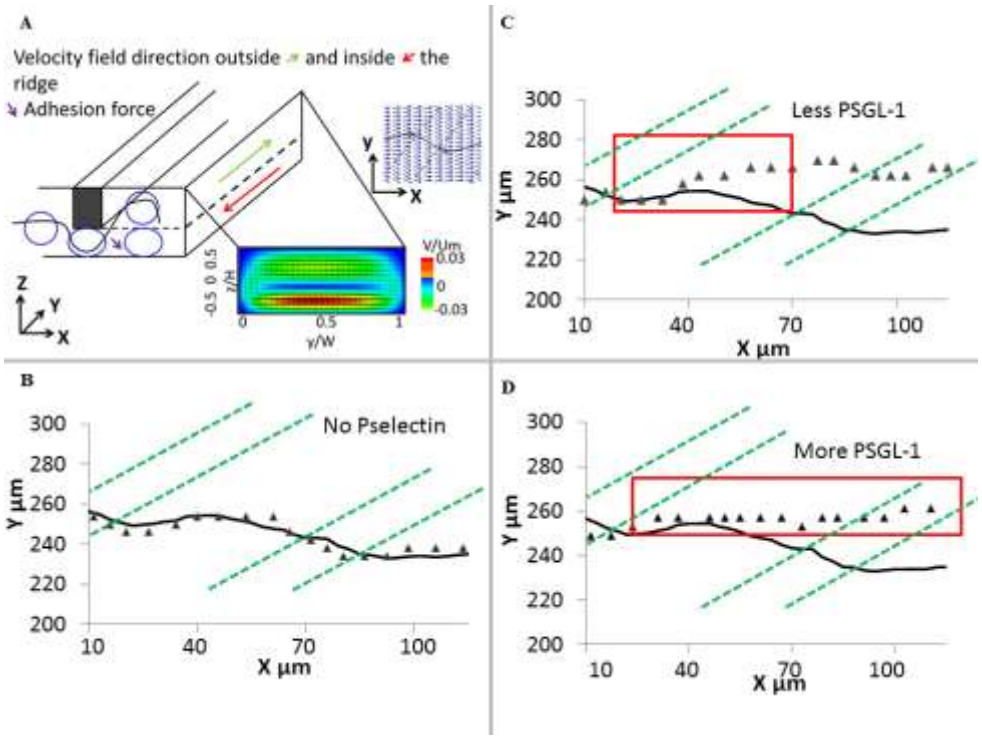

Figure 36 A) Schematic explaining the adhesion mechanism using secondary flow field. As cells flow under the ridge, they bind to P-selectin.When they leave the ridges cells with more ligand expressed on their surface resist the secondary drag force and stay adhered to bottom of the channel and experience the flow in negative y direction (red arrow).On the other hand cells with less ligand detach from the surface and enter the stramline in positive y direction (green arrow). B) Showing the cell trajectory in without P selectin coated device, C and D) trajectories of cells with less and more PSGL-1 respectively with P selectin coated device and all are compared with streamline at the middle height of the gap size with z velocity set to zero.

The working mechanism of device is explained in Figure36 A. As cells flow under the ridge, they bind to P-selectin and when leaving the ridges cells with more ligand expressed on their surface resist the secondary drag force and stay adhered to bottom of the channel and experience the flow in negative y direction (red arrow). On the other hand, cells with less ligand detach and pull away from the surface and enter the streamline in positive y direction (green arrow). Cells flowing through the device without P selectin

coated ridges move with the fluid flow streamlines. The trajectories of Jurkat cells are compared with COMSOL streamline at height equals to half of the gap size in xy-plane (Figure 36 B, C and D). Cells closely follow the simulated streamline in the case of a device with no P selectin. Since cells in the stream are located near the bot-tom channel wall with weak elastic force and no adhesion force, they are transported by the circulating flow, created by ridges, in the negative transverse direction as shown in Figure 4B. In the case of less PSGL-1 on the cell surface (Figure 36C), as a cell leaves the ridge it is pulled off and detached from the surface and follows the streamlines that moves up in y direction. On the other hand a cell with more PSGL-1 (Figure 36D) is attached to the surface once it enters the ridge and rolls nearly straight on the bottom glass sur-face as it leaves the ridge.

Gap size optimization was also done using 14 and 9 μm gap sizes as shown in Figure 37 A and B. After cell separation, we examined cell stiffness collected at three outlets as shown in Figure 37 C, which indicates that stiffness was not a determining factor in the cell sorting mechanism. Fluorescent imaging (Figure 38) of our device after the flow experiment verified that P-selectin was not removed after flow experiments. Therefore, P-selectin coating remains intact throughout the flow experiment.

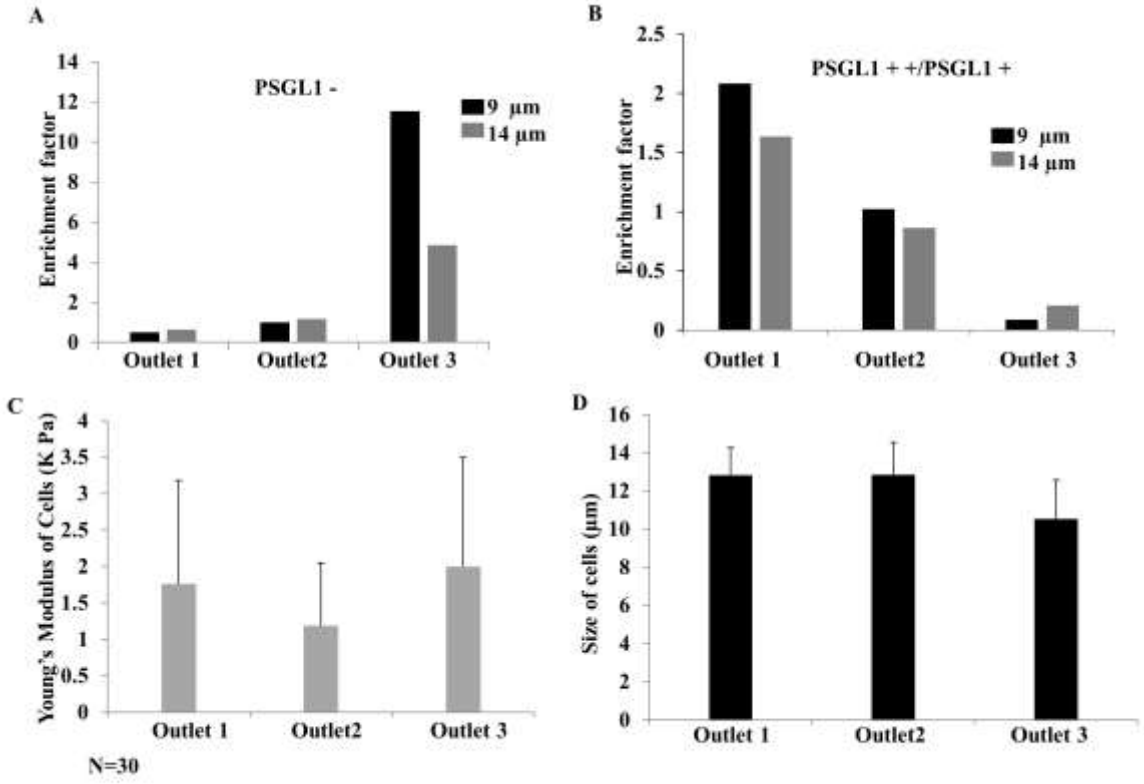

Figure 37 A and B) Shows the enrichment factors for PSGL-1 ++/PSGL-1 + and – Jurkat cells for gap size optimization of the adhesion based sorting device. As the gap size is changed from 9 to 14 µm, the device efficiency decreases as indicated by the enrichment factors. C) Young's modulus of HL60 cells collected at different outlets measured using AFM and D) their size using ImageJ .The data suggests that the device can sort by adhesion, with minimal effect of mechanics.

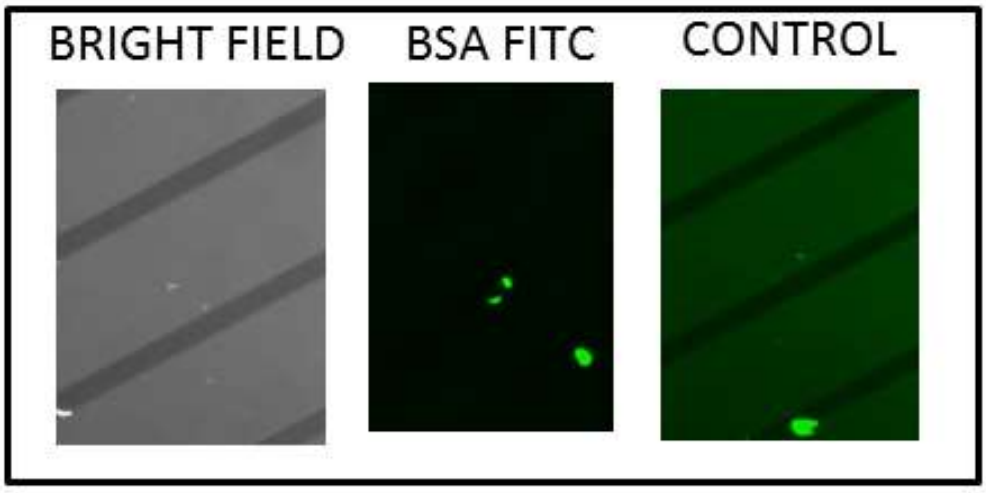

Figure 38 Images showing P-selectin coated device after flow experiment treated with FITC BSA for detecting non specific binding or in other words detachement of P-selectin in bright field (left) and flouresecent (right) microscopy.

We have also demonstrated 26 and 4.4-fold enrichment of PSGL-1 positive and negative Jurkat cells respectively s shown in Figure 39 A, B and C. We have also observed the fractionation of single cell line based on the ligand it expresses at such high flow rates with significant population enrichment as shown in Figure 39 D. The fractionation results show promising applications of this device in comparison with FACS that gives binary results for analog world. In addition, FACS is not suitable for rare cell sorting, as it requires a minimum sample size to accurately sort cells. Hence, this device offers unique capability of fractionating rare cells.

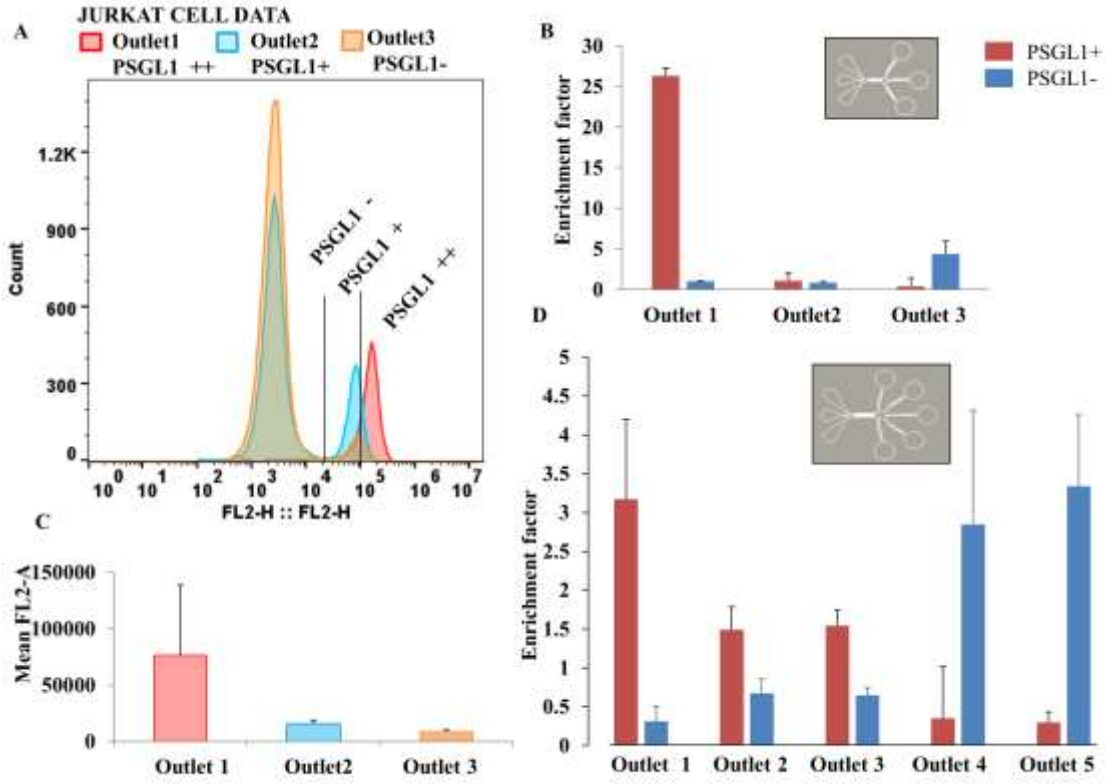

Figure 39 A) Shows the flow cytometer data for Jurkat cells collected at different outlets showing a peak shift in their mean fluorescent values. B) Shows the enrichment factor for three outlet device and C) for five outlet device.

We have conducted three sets of experiments in order to compare activation of cells due to PSGL-1 and P-selectin binding. CD69 which is an activation inducer molecule and classical marker CD11b are used to detect the activation of cells .Both markers are up-regulated upon activation[180]. In the first experiment we incubated Jurkat cells with P-selectin for 24 hours at 37 degree C with 5% Carbon dioxide .In the second experiment we incubated Jurkat cells for 2 hours with P-selectin coated PDMS surface (PDMS surface was first activated by incubating it with P-selectin for 3 hours at room temperature) at 37 degree C with 5% Carbon dioxide and in the third experiment Jurkat cells are collected

after sorting through the proposed device. Expressions of CD69 and Mac-1 (CD11b) were compared for all the three experiments using flow cytometry. The results in Figure 40 shows there is slight up regulation of activation markers after cells are incubated with P-selectin for 24 hours but very significant change when removed from P-selectin coated surface. There is no change in expression of activation markers in case of cells collected after sorting. These results indicates no cell activation of sorted sample as there is very short binding time between P-selectin and PSGL-1 while cells are flowing through the device and also association and dissociation is gentle enough that it does not activate cells.

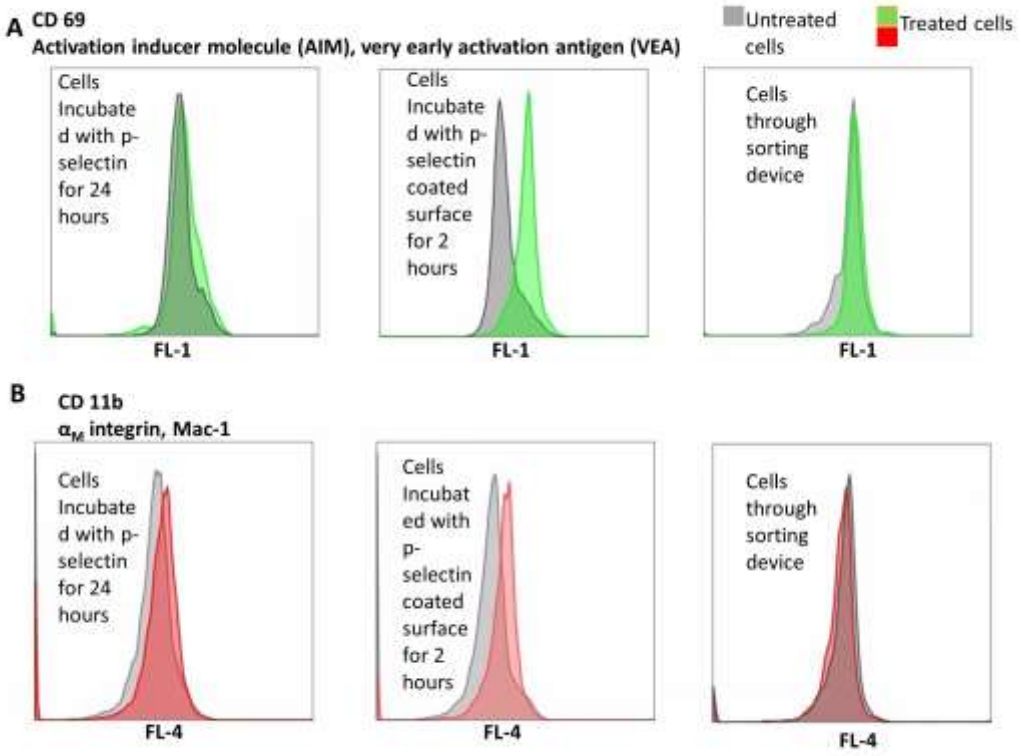

Figure 40 A) CD 69 (Very early activation antigen) and B) CD11b markers are used to study if the cells are activated after sorting. Results are compared with cells

incubated with P-selectin for 24 hours and cells incubated with P-selectin coated surface for 2 hr. There is a significant up regulation of activation markers after cells removed from P-selectin coated surface. There is no change in activation markers in case of cells collected after sorting.

.

4.6 Conclusion

We successfully separated Jurkat and HL60 cell lines based on their differential expression of PSGL-1 ligand by using a single ridged channel coated with P-selectin. We demonstrate 26-fold and 3.8-fold enrichment of PSGL-1 positive and 4.4-fold and 3.2-fold enrichment of PSGL-1 negative Jurkat and HL60 cells respectively. We have also demonstrated the enrichment of PSGL-1 positive Jurkat cells to 3-fold using a five outlet fractionation device. The cells flow with a rate of 0.2 m/s, which corresponds to 0.54million cells/s and is an order of magnitude higher than previous adhesive based sorting approaches.

CHAPTER 5. CONCLUSION AND FUTURE WORK

In this study, we have developed a novel multimodal microfluidic device capable of improved purity of size-dependent separation of particles as well as molecule specific adhesion based cell sorting. Intellectual contribution is summarized as follows:

- High throughput cell/particle size based sorting microfluidics using vertical focusing in a ridged microchannel.
- High throughput molecule specific adhesion based sorting and fractionation platform.
- Three dimensional tracking of particles in micro flow platform using in and off focus diffraction

In size based sorting, particles were placed at the optimal position in three-dimensional space to exaggerate the size-dependent trajectory differences. This is achieved by incorporating a unique aspect of sorting design by utilizing three-dimensional focusing of the sample to a position that optimizes the differential secondary flows. Using vertical focusing, we are able to separate 2 μm particles from 7 μm with a substantial improvement in enrichment of sorted number density in comparison to unfocused flow. We demonstrate 8-fold increase of the purity of the larger particles (from 2.5 to 19.5–fold enrichment factor) and a 35–fold increase in the purity of smaller particles (from 3.4–fold to 117.8–fold). This is the first time that a device with 3D focusing has been reported to improve the purity of samples using size sorting. Using this technology we demonstrated size based

leukapheresis, which offers higher or comparable throughput with cutting edge techniques with high recovery and no pre or post processing of samples for analysis and isolation. The WBCs were removed at a depletion of 87 folds and at a high throughput of 0.1X10^8 cells /min with recovery of 73% .These results suggest that the proposed device can be used as a commercial leukapheresis with parallelization (Figure 41) as it offers high throughput, high depletion and recovery rate of WBCs with ease of batch fabrication and low cost. One concern is toxicity of PDMS that needs to be addressed. We also ran preliminary experiment to sort leukocytes from cord blood to be used in cheap production of CD 34 + and CD 11b +cells that can be differentiated into endothelial cells to treat Krabbe diseases[181] Figure 42. The proposed technology can further be improved for higher purity enrichment of particles by modifying channel geometry and gap size[103]. It can also be integrated with separation techniques using different biomarkers like stiffness and viscoelastic deformation.[75, 104] Our device is simple with small foot prints, cheap, offers clog free or self-cleaning platform with high throughput and enrichment. The proposed z-focusing approach can be extended to separate nanoparticles by using smaller gap size and using optimized flow rate ratios.

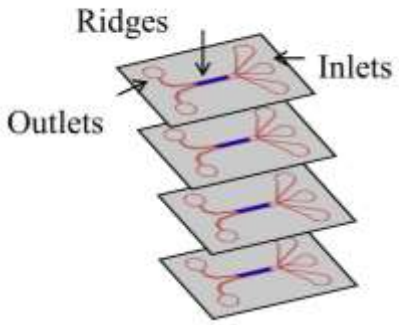

Figure 41 Parallelization of proposed device.

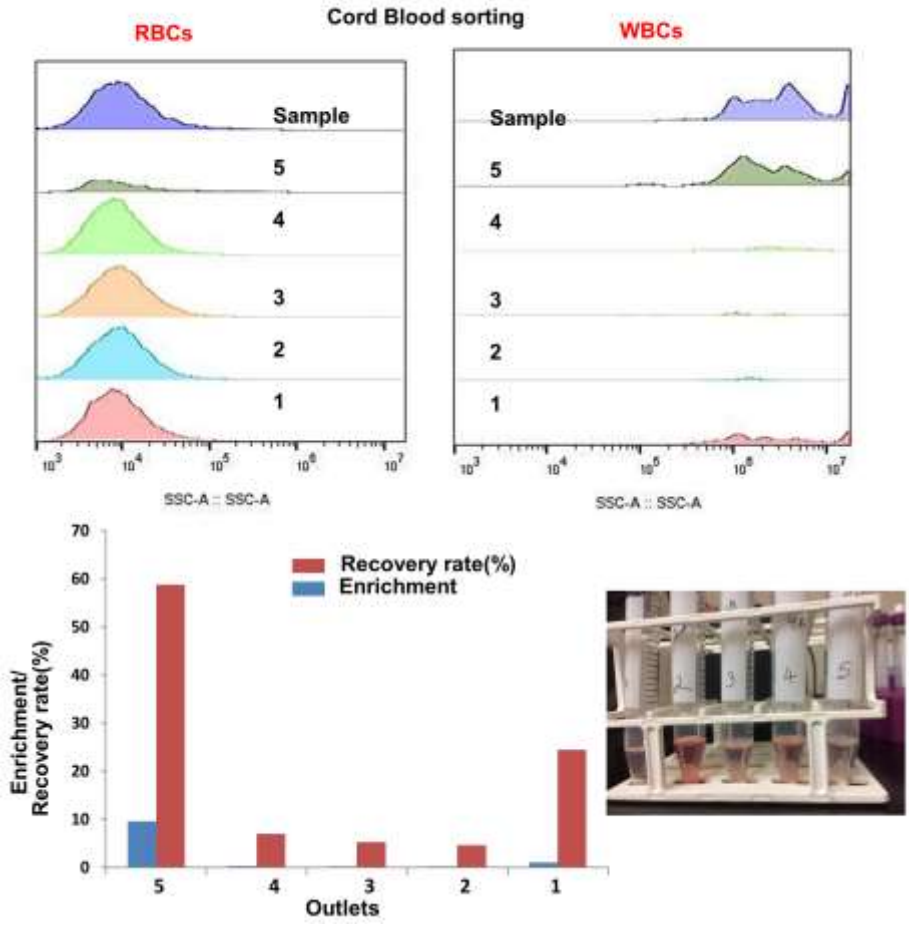

Figure 42 Cord blood sorting.

We have also demonstrated that sorting device is capable of high throughput separation of cells by differences in specific cell adhesion. As a proof of principle of the method, we have separated Jurkat and HL60 cell lines based on their differential expression of PSGL-1 ligand by using a single ridged channel coated with P-selectin. We demonstrate 26-fold and 3.8-fold enrichment of PSGL-1 positive and 4.4-fold and 3.2-fold enrichment of PSGL-1 negative Jurkat and HL60 cells respectively. We have also demonstrated the enrichment of PSGL-1 positive Jurkat cells to 3-fold using a five outlet fractionation device. We demonstrated separation of a single cell type into subpopulations of cells that are highly adhesive, moderate adhesive, and low adhesive. Such an approach may find use in downstream analysis and selection of cells for a highly expressed adhesive phenotype. There is no dependence on stiffness, size and charge of cells. Single input with self-focusing to reduce reagent use and improve ease of use has been successfully employed in this work. Device self-cleaning capability allows less interrupted fluid flow and that prevents compromising the flow with clogging.

Adhesion based sorting can produce signal changes in the cells. Beads used for binding and pulling down cells can activate them so is the high shear release of captured cells[182]. Studies have also indicated that engagement of selectin ligands on leucocytes directly transduces signals[183]. For example, interactions of PSGL-1 with immobilized P-selectin rapidly induce tyrosine phosphorylation of multiple proteins [184].However, the data presented shows that increase in tyrosine phosphorylation is observed at least 2 minutes after P selectin and PSGL-1 binding. Our device provide another application where cell sorting is possible without cell activation due to very short binding contact between

receptor and ligand. Unlike MACS and panning, the separation can quantify the amount of surface antigen on a cell and also eliminate the limitation posed by the choice of antibodies is limited within a pool of commercially available antibodies, which in turn limits the separation targets to those cells with specific markers[105]. This is the first study that shows fractionation of single cell line based on ligand expression with high flow processing rates for significant adhesive cellular enrichment. One of the potential applications for fractionation of single cell line is sorting T cells based on the density of CD20 required to activate T cells expressing a CD20-specific CAR (chimeric Ag receptor). Potential targets for CAR-based therapies are cell surface antigens expressed at higher densities on cancer cells, and these densities typically vary from one target to another. A recent study investigated the density of CD20 required to activate T cells expressing a CD20-specific CAR [185].Using cell lines that expressed CD20 at various densities (very low to high, approximately 200–200 000 molecules/cell), can be removed using the proposed device instead of the CAR-CD20 T cells mediated lysis of cells expressing the lowest detectable level of CD20.

Further, work can be done using the device to sort CTCs and multiple biological cells to sort simultaneously with high throughput. The proposed device also offers direct measurement of transient nature interaction between important physiological ligands and interacting cells. It can be used as a tool to monitor stem cell differentiation [186] .It also has potential applications in measuring degree of changes in adhesion signature of cancer cells[187-188], hence better therapeutics.

The ligand based sorting also has potential applications in understanding the role of PSGL-1 in T cell immune response and developing effective therapeutics. Activated platelets can interact with lung cancer cells through PSGL-1. Inhibiting platelet activation and/or down-regulating PSGL-1 expression may be useful for suppression of tumor metastasis [96]. Clinical trial can be run based on the sorted T cells with our device.

The availability of a number of cell adhesion molecules which are tied to important physiological phenomena has made this a rich topic with many possible avenues of investigation. Identifying and collecting cells that express desired molecular surface markers will thus benefit a variety of cell therapy and medical diagnostics .For example bacterial adhesion molecules[90], selectins involved in homing of circulating cells[91], and MHC-II molecules on antigen towards the T-cell receptor[92] can be used for molecule specific sorting. However, understanding these interactions and eventually building up a robust and accurate microfluidics is challenging and more experimental work needs to be done.

APPENDIX A

A.1 3D Particle tracking MATLAB code

```
% using polyparticle tracking free ware track x and y coordinates and load them into
workspace
% following function will determine the height of the particle
Function[Z]=Height(x,y,frame_in,frame_out,file,reference)
% x and y are coordinates tracked by 2D tracking software
% frame_in and frame_out are start and end number values of frames from the video to be
analyzed
%file is the name of video with type. Example Video.avi
%reference is the name of reference image template with type. Example Template.png
x=round(x);
y=round(y);
l=frame_out-frame_in;
xpeak=x;
ypeak=y;
mov=aviread('file',frame_in:frame_out);
for(i=1:1:l)
[im,map]=frame2im(mov(i));
a=rgb2gray(im);
```

```
i2=imcrop(a,[x(i)-20 y(i)-21 40 42]);% cropping image of particle
b=imread('reference');
c = normxcorr2(i2(:,:,1),b(:,:,1));
[max_c, imax] = max(abs(c(:)));
[y, x] = ind2sub(size(c),imax(1));
xpeak(i)=x-20;
ypeak(i)=y-21;
end
% The Z value is then compared with the calibrated Z values
Z=xpeak;
for(i=1:1:l)
      if (Z(i)>=113)&(Z(i)<205),Z(i)=0;
       elseif (Z(i)>=205)&(Z(i)<289),Z(i)=0.5;
       elseif (Z(i)>=289)&(Z(i)<373), Z(i)=1;
       elseif (Z(i)>=373)&(Z(i)<455),Z(i)=1.5;
       elseif (Z(i)>=455)&(Z(i)<541),Z(i)=2;
       elseif (Z(i)>=541)&(Z(i)<617),Z(i)=2.5;
       elseif (Z(i)>=617)&(Z(i)<699),Z(i)=3;
   else Z(i)=Z(i-1);
   end
   i=i+1;
end
```

In order to interpolate between multiple images, all the images should be the same size, and the center of the particle should be at the same location in each of the images. We

wrote a program that requires a set of images whose center is located inside the particle, and output a set of images of the same size with the center of the particle located at the center of each image. The program locates 3 points at the circumference of the circle ((x1, y1) , (x2 , y2), (x3 , y3))and then uses the following set of equations to locate the center of the circle (X, Y).

$$N_1 = \begin{vmatrix} (x_2^2 + y_2^2) - (x_1^2 - y_1^2) & y_2 - y_1 \\ (x_3^2 + y_3^2) - (x_1^2 - y_1^2) & y_3 - y_1 \end{vmatrix} \qquad N_2$$

$$= \begin{vmatrix} x_2 - x_1 & (x_2^2 + y_2^2) - (x_1^2 - y_1^2) \\ x_3 - x_1 & (x_3^2 + y_3^2) - (x_1^2 - y_1^2) \end{vmatrix} \tag{5}$$

$$D1 = \begin{vmatrix} x_2 - x_1 & y_2 - y_1 \\ x_3 - x_1 & y_3 - y_1 \end{vmatrix} \tag{6}$$

$$X = \frac{N_1}{2D1} \quad Y = \frac{N_2}{2D1} \tag{7}$$

After obtaining the centralized images, we created a loop that creates a function for each pixel in the image, and interpolates the value of that pixel for the given depths. The code used to achieve this is shown below. This results in a set of interpolated images at the desired depths.

```
function [] = imgInterp(ImageNames, Depths, interpType, outputDepths, outputFormat)
```

```
NumOfInputImgs = length(Depths);

for index = [1:NumOfInputImgs]

Images{index} = double(imread(ImageNames{index}));

end

[ImageX ImageY ~] = size(Images{1});

for ImgDepth = outputDepths

OutputImage = zeros(ImageX, ImageY, 3);

for colour = [1:3]

for i = [1:ImageX]

for j = [1:ImageY]

Yvals = zeros(1,NumOfInputImgs);

for index = [1:NumOfInputImgs]

Yvals(index) = Images{index}(i,j,colour);

end

OutputImage(i,j,colour)= interp1(Depths,Yvals,ImgDepth, interpType);

end
```

```
end

end

imwrite(uint8(OutputImage),['InterpImage',num2str(ImgDepth,2),'.jpeg'], outputFormat);

end

end
```

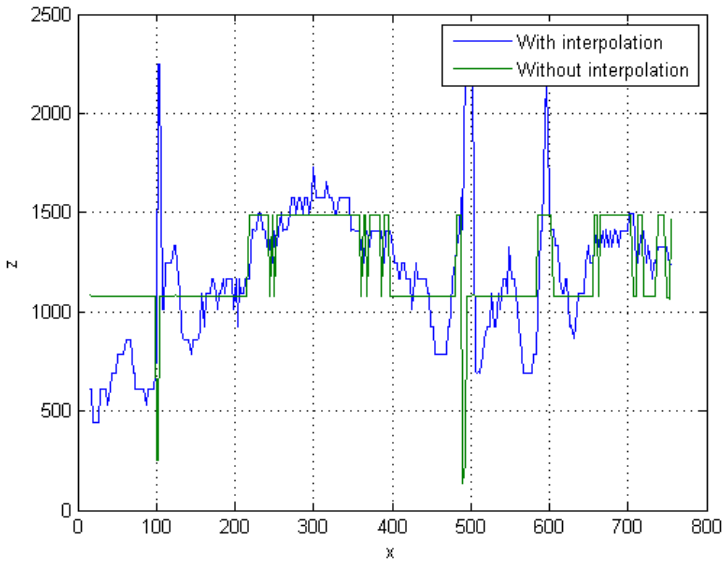

Figure 43 Tracked trajectories without and with interpolation .The resolution of trajectory is improved with interpolation.

A.2 A mathematical model for predicting the height of hydrodynamically focused streams in a rectangular microchannel

The three dimensional hydrodynamic focusing was implemented in a similar manner previously described[189]. The model for predicting the height of 2 D hydrodynamically focused streams in a rectangular microchannel is given in Figure 44 and derived as described previously[190]. Following assumptions are made: (i) Flow in the microchannel is steady and laminar. (ii) Fluids are Newtonian. (iii) Fluid has the same density in the inlet, sheath and outlet channel.

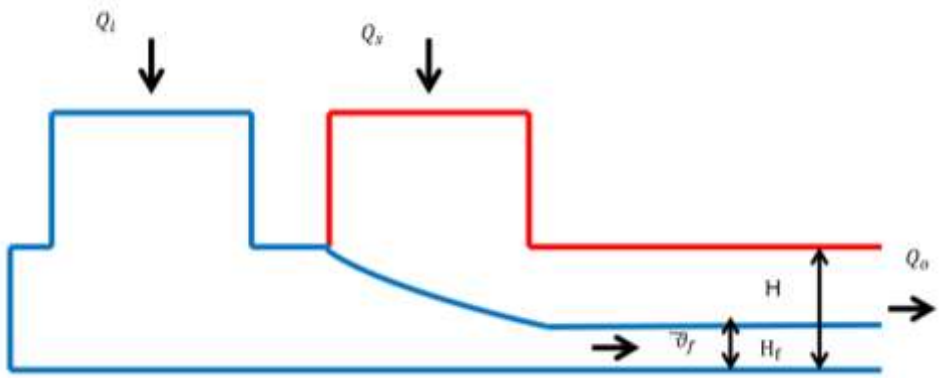

Figure 44 Schematic of mathematical model.

According to the principle of mass conservation, the amount of fluid passing through the inlet channel must equal to the amount of fluid passing through the dimension of the focused stream, i.e.

$$H_f = \frac{Q_i}{\bar{v}_f X\ W} \tag{8}$$

H is the height and W is the width of the channel, H_f is hydrodynamically focused stream and $Q_i$and Q_s are volumetric flow rates of the sample and sheath channel inlets. The total amount of fluid passing through the outlet channel must equal the total amount of fluid supplied from the inlet and sheath,

$$\bar{\vartheta}_o = \frac{Q_i + Q_s}{HX\ W} \tag{9}$$

Therefore, the relationship between the height of the hydrodynamically focused stream and the volumetric flow rates of the inlet channel and the sheath can be expressed as

$$\frac{H_f}{H} = \frac{Q_i}{(Q_s + Q_i)\gamma} \tag{10}$$

where the velocity ratio $\gamma = \bar{\vartheta}_f / \bar{\vartheta}_o$ is to be found. $\bar{\vartheta}_f$ and $\bar{\vartheta}_o$ are the average flow velocities in the focused stream and the outlet channel, respectively. The Reynolds number is generally very small in microfluidic devices. Since viscous effects dominate in low Reynolds number flows, the entrance length in the microchannel is very short. Therefore,

the flow in the outlet channel can be assumed to be fully developed. Hence, the basic equation of the flow is given by

$$\frac{\partial^2 u}{\partial y^2} + \frac{\partial^2 u}{\partial z^2} = \frac{1}{\mu}\frac{dp}{dx} = const \tag{11}$$

where u(y, z), dp/dx and μ are the stream wise velocity, pressure gradient and fluid viscosity in the outlet channel, respectively. Imposing the no-slip condition on the channel wall, Equation 11 can be solved as

$$u(y,z) = \frac{4W^2}{\mu\pi^3}\left(\frac{-dp}{dx}\right)\sum_{n=0}^{\infty}(-1)^n X\left\{1 - \frac{\cosh[\frac{(2n+1)\pi y}{W}]}{\cosh[\frac{(2n+1)\pi H}{2W}]}\right\}\frac{\cos[\frac{(2n+1)\pi z}{W}]}{(2n+1)^3} \tag{12}$$

Equation 12 is the well-known Poiseuille velocity profile for flow through a rectangular channel. Integrating equation 12 along the y-direction, the stream wise average velocity $\bar{u}(z)$in the rectangular microchannel can be expressed as

$$\overline{u(z)} = \frac{1}{W}\int_{-\frac{W}{2}}^{\frac{W}{2}} u(y,z)dz$$

$$= \frac{8W^2}{\mu\pi^4}\left(\frac{-dp}{dx}\right)\sum_{n=0}^{\infty}\frac{1}{(2n+1)^4}X\left\{1-\frac{\cosh\left[\frac{(2n+1)\pi y}{W}\right]}{\cosh\left[\frac{(2n+1)\pi H}{2W}\right]}\right\} \quad (13)$$

The average velocities in the outlet channel, $\overline{\vartheta}_o$, and the focused stream, $\overline{\vartheta}_f$, can be obtained from equation 10. The velocity ratio, γ, is then given by

$$\gamma = \overline{\vartheta}_f/\overline{\vartheta}_o = \frac{\frac{2}{H_f}\int_0^{H_f/2} u(y)dy}{\frac{2}{H_f}\int_0^{H/2} u(y)dy} = \frac{\left\{1-(192W/\pi^5 H_f\sum_{n=0}^{\infty}\frac{1}{(2n+1)^5}\frac{\sinh(2n+1)\pi H_f/2W}{\cosh(2n+1)\pi H_f/2W}\right\}}{\left\{1-(192W/\pi^5 H\sum_{n=0}^{\infty}\frac{\tanh(2n+1)\pi H/2W}{(2n+1)^5}\right\}} \quad (14)$$

Equation 14 reveals that γ is dependent on the aspect ratio. When aspect ratio ε $= H/W \rightarrow 0$, a parabolic velocity profile is formed across the channel height and is independent of the position across the channel width (i.e. the velocity profile is 'plug-like' across the channel width). Under such conditions, γ = 1.0.[191] From this mathematical model we found a range of flow rate ratios that positioned particles in a consistent z position range for improved consistency of transverse flow fields and thus improved size sorting.

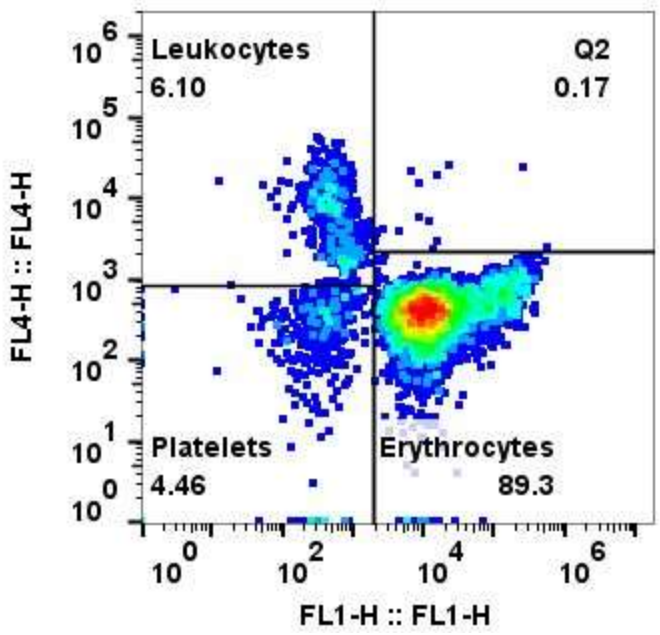

Figure 45 Centrifugation flow cytometry data. The buffy coat extracted from centrifuged blood sample shows mixture of erythrocytes and platelets along with leukocytes. Leukocytes are enriched by 54 –fold which is substantially less as compare to the optimized device.

A.3. Activation study

In this section we determined the activation of T cells in our study using model kinetic discrimination in T-cell activation [192] and bond density using AFM data and Bell's equation.

The ligand receptor interaction results in biochemical reactions which may or may not result in final product or positive activation signal. The positive or negative signaling depends on the association and dissociation rates of these interactions. The model in Figure 46 calculates these negative and positive signals based on association and dissociation constants and determine if the cells are activated or not.

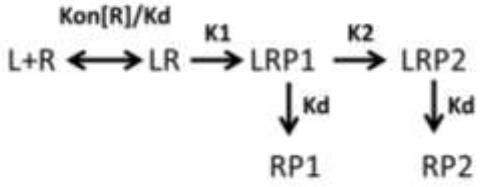

Figure 46 Schematic of kinetic model.

The kinetic model has assumed density of ligands (L) is small as compared to receptors(R). In a steady-state condition, ligand L binds to and dissociates from the receptor (R)

$$L + R \overset{K_{on}[R]/Kd}{\longleftrightarrow} LR \tag{15}$$

The first intracellular biochemical reaction results in covalent modification denoted LRP1.

$$LR \overset{K1}{\rightarrow} LRP1 \tag{16}$$

At this point, one of two events is possible. The receptor may be modified further, producing a second product LRP2 or the ligand dissociates.

$$LRP1 \overset{K2}{\rightarrow} LRP2 \tag{17}$$

$$LRP1 \overset{Kd}{\rightarrow} RP1 + L \tag{18}$$

In this simple model, the modified receptor RP1 leads to a negative (incomplete) signal, whereas the modified receptor RP2 leads to a positive (complete) signal. Positive and negative signals are related to three factors: the number of binding events per ligand per time (B'), the fraction of ligand-bound T-cell receptor that reacts to form LRP1 (f'), and the fraction of LRP1 that reacts to form LRP2 (p') versus the fraction of LRP, that fails to react prior to ligand dissociation (q'). The number of binding events is based on a steady state approximation of the serial engagement model [193].Quantitatively B' = 1/(D' + 1/Kd), where D' = 1/(Kon receptor concentration),f' = k1/(K1 + Kd), p' = K2/(K2 + Kd), and q' = 1 – p' = Kd/(K2 + Kd). The fraction of binding events leading to LRP2 is f'.p' and the fraction of binding events leading to LRP1 but not LRP2 is f'.q'. Positive and negative signals per ligand per time are P = B'.f'p' and Q = B'f'q' respectively. K1=10, K2=1 and Ton= 4400K. The dissociation constant (off-rate) varies over three orders of magnitude from 0.02 /s under zero force up to 15 /s under external applied forces for P-selectin /PsGL-1 interaction [194].The results Figure 47 indicate that positive signal dose not reach or even close to the activation value (peak value in graph).

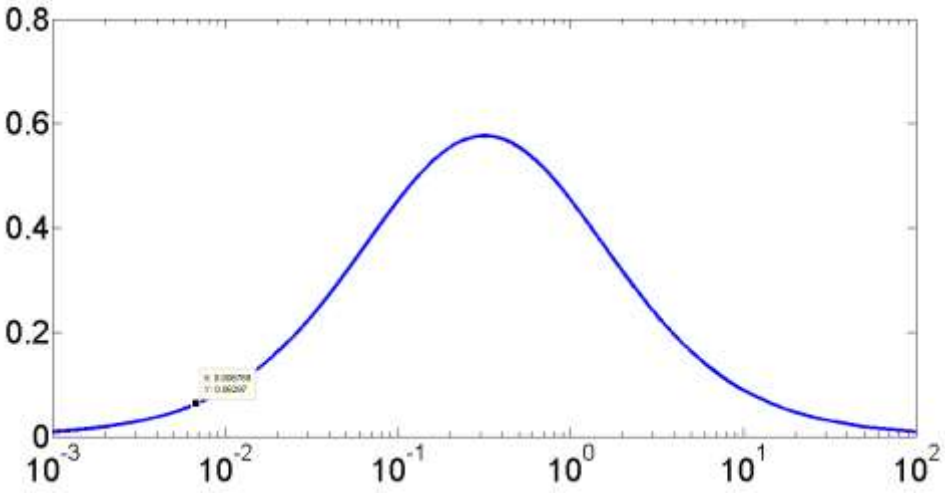

Figure 47 Positive signal plotted as a function of dissociation constant.

We have also calculated the bond density at each point using Bell's equation [195]

$$N_r = \frac{F_D}{f_c} \tag{19}$$

Where F_D is the fluid drag force which is the secondary flow force and f_c is the critical force per potential bond to resist the drag force. f_c is the adhesion force at each point. The bond density at points A,B,C and D are also calculated using equation [196] where bonds are considered to spring like in nature.

$$F_A = K\, N_r X_d \tag{20}$$

Where F_A is the adhesion force, K is the transient spring constant for P-selectin /PSGL-1 binding (0.00048 N/m [196]) and X_d is the total lateral distance before the bond dissociation due to fluid flow. The calculated values are very close for bond densities using the above

equations .Now if we calculate the bond density with modification of $X_d = \beta' - \lambda'$, where β' is the stretched bond length and λ' is the unstretched bond length and are equals to 79 nm [197] and 10nm [196] for P-selectin /PSGL-1 bond. We found that N_r has a value which is 100 times higher. This is due to the fact that $\beta' \, and \, \lambda'$ used are measured using AFM and adhesion force is much lower for these experiments.

Table 5 Bond density

	$N_r(Eq.19)$	$N_r(Eq.20)$	$N_r(Xd = \beta' - \lambda')$
A	1.856	2.105	288
B	2.187	2.4	252
C	2.395	1.7	228
D	2.9	2.7	189

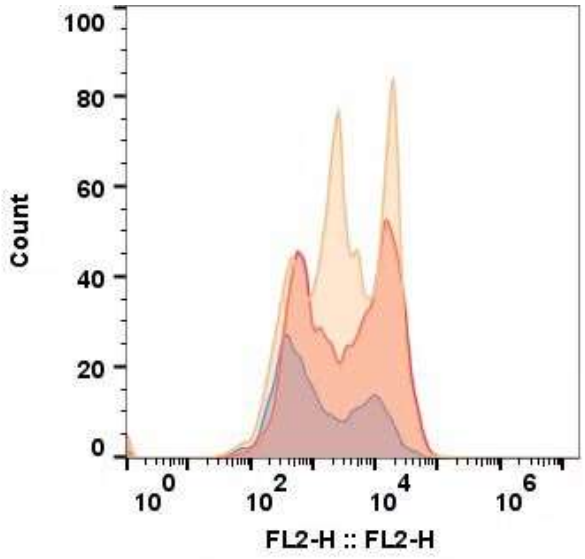

Figure 48 Flow cytometry results for Jurkat cells flowing at a flow rate of 4.5 µl/min through P-selectin coated device. Expression level of PSGL-1 of cells is plotted in terms of mean fluorescent intensity (x-axis) of fluorescently tagged secondary antibodies.

REFERENCES

1. Emery, P.; Dörner, T., Optimising treatment in rheumatoid arthritis: a review of potential biological markers of response. *Annals of the rheumatic diseases* **2011**, annrheumdis-2010-148015.

2. Szodoray, P.; Szabó, Z.; Kapitány, A.; Gyetvai, Á.; Lakos, G.; Szántó, S.; Szücs, G.; Szekanecz, Z., Anti-citrullinated protein/peptide autoantibodies in association with genetic and environmental factors as indicators of disease outcome in rheumatoid arthritis. *Autoimmunity reviews* **2010,** *9* (3), 140-143.

3. Iskandar, H. N.; Ciorba, M. A., Biomarkers in inflammatory bowel disease: current practices and recent advances. *Translational Research* **2012,** *159* (4), 313-325.

4. Rhea, J. M.; Molinaro, R. J., Cancer biomarkers: surviving the journey from bench to bedside. *MLO: medical laboratory observer* **2011,** *43* (3), 10-2, 16, 18; quiz 20, 22.

5. Bruce Alberts, A.; Lewis, J.; Raff, M.; Roberts, K.; Walter, P., Molecular biology of the cell. 2002. *Garland Science*.

6. Toner, M.; Irimia, D., BLOOD-ON-A-CHIP. *Annual review of biomedical engineering* **2005,** *7*, 77-103.

7. William, F. G., Review of medical physiology. *Maruzen Asian Edition, Lange* **2003**.

8. Turgeon, M. L., *Clinical hematology: theory and procedures*. Lippincott Williams & Wilkins: 2005.

9. Fu, J., Emerging microfluidic tools for functional cellular immunophenotyping: a new potential paradigm for immune status characterization. **2013**.

10. Zhou, Q.; Kwa, T.; Liu, Y.; Revzin, A., Cytokine biosensors: the future of infectious disease diagnosis? *Expert review of anti-infective therapy* **2012,** *10* (10), 1079-1081.

11. McPherson, R. A.; Pincus, M. R., *Henry's clinical diagnosis and management by laboratory methods*. Elsevier Health Sciences: 2016.

12. Bianchi, D. W., Fetal cells in the maternal circulation: feasibility for prenatal diagnosis. *British journal of haematology* **1999,** *105* (3), 574-583.

13. Guetta, E.; Simchen, M. J.; Mammon-Daviko, K.; Gordon, D.; Aviram-Goldring, A.; Rauchbach, N.; Barkai, G., Analysis of fetal blood cells in the maternal circulation: challenges, ongoing efforts, and potential solutions. *Stem cells and development* **2004,** *13* (1), 93-99.

14. Wachtel, S.; Shulman, L.; Sammons, D., Fetal cells in maternal blood. *Clinical genetics* **2001,** *59* (2), 74-79.

15. Mavrou, A.; Kouvidi, E.; Antsaklis, A.; Souka, A.; Kitsiou Tzeli, S.; Kolialexi, A., Identification of nucleated red blood cells in maternal circulation: a second step in screening for fetal aneuploidies and pregnancy complications. *Prenatal diagnosis* **2007,** *27* (2), 150-153.

16. Pratt, E. D.; Huang, C.; Hawkins, B. G.; Gleghorn, J. P.; Kirby, B. J., Rare cell capture in microfluidic devices. *Chemical engineering science* **2011,** *66* (7), 1508-1522.

17. Buckner, D.; GRAW, R. G.; EISEL, R. J.; HENDERSON, E. S.; Perry, S., Leukapheresis* by continuous flow centrifugation (CFC) in patients with chronic myelocytic leukemia (CML). *Blood* **1969,** *33* (2), 353-369.

18. Malachowski, M.; Comenzo, R.; Hillyer, C.; Tiegerman, K.; Berkman, E., Large-volume leukapheresis for peripheral blood stem cell collection in patients with hematologic malignancies. *Transfusion* **1992,** *32* (8), 732-735.

19. Chu, R., Leukocytes in blood transfusion: adverse effects and their prevention. *Hong Kong Med J* **1999,** *5* (3), 280-284.

20. Habibi, N.; Soumetz, F. C.; Giulianelli, M.; Pastorino, L.; Herrera, O.; Sbrana, F.; Raiteri, R.; Ruggiero, C. In *Self-assembly and recrystallization of bacterial S-layer proteins of Bacillus sphaericus and Bacillus thuringiensis on silicone, mica and quartz crystal supports*, 2010 Annual International Conference of the IEEE Engineering in Medicine and Biology, IEEE: 2010; pp 3739-3742.

21. Herrmann, A.; Fleischer, K.; Czajkowska, H.; Müller-Newen, G.; Becker, W., Characterization of cyclin L1 as an immobile component of the splicing factor compartment. *The FASEB Journal* **2007,** *21* (12), 3142-3152.

22. Dandulakis, G.; Herr, J. C.; Kirwan, D. J., Cell growth and monoclonal antibody production in the presence of antigen and serum. *Biotechnology progress* **1995,** *11* (5), 518-524.

23. Bierer, B. E.; Herrmann, S. H.; Brown, C. S.; Burakoff, S. J.; Golan, D. E., Lateral mobility of class I histocompatibility antigens in B lymphoblastoid cell membranes: modulation by cross-linking and effect of cell density. *The Journal of cell biology* **1987,** *105* (3), 1147-1152.

24. Triulzi, D.; Grifith, B., Blood usage in lung transplantation. *Transfusion* **1998,** *38* (1), 12-15.

25. Cristofanilli, M.; Budd, G. T.; Ellis, M. J.; Stopeck, A.; Matera, J.; Miller, M. C.; Reuben, J. M.; Doyle, G. V.; Allard, W. J.; Terstappen, L. W., Circulating tumor cells, disease progression, and survival in metastatic breast cancer. *New England Journal of Medicine* **2004,** *351* (8), 781-791.

26. Liu, M. C.; Shields, P. G.; Warren, R. D.; Cohen, P.; Wilkinson, M.; Ottaviano, Y. L.; Rao, S. B.; Eng-Wong, J.; Seillier-Moiseiwitsch, F.; Noone, A.-M., Circulating tumor cells: a useful predictor of treatment efficacy in metastatic breast cancer. *Journal of Clinical Oncology* **2009,** *27* (31), 5153-5159.

27. Miller, M. C.; Doyle, G. V.; Terstappen, L. W., Significance of circulating tumor cells detected by the CellSearch system in patients with metastatic breast colorectal and prostate cancer. *Journal of oncology* **2009,** *2010*.

28. Jones, M. L.; Siddiqui, J.; Pienta, K. J.; Getzenberg, R. H., Circulating fibroblast-like cells in men with metastatic prostate cancer. *The Prostate* **2013,** *73* (2), 176-181.

29. Bongiorno, T.; Kazlow, J.; Mezencev, R.; Griffiths, S.; Olivares-Navarrete, R.; McDonald, J. F.; Schwartz, Z.; Boyan, B. D.; McDevitt, T. C.; Sulchek, T., Mechanical stiffness as an improved single-cell indicator of osteoblastic human mesenchymal stem cell differentiation. *Journal of biomechanics* **2014,** *47* (9), 2197-2204.

30. Dharmasiri, U.; Witek, M. A.; Adams, A. A.; Soper, S. A., Microsystems for the capture of low-abundance cells. *Annual review of analytical chemistry* **2010,** *3*, 409-431.

31. Yu, Z. T. F.; Yong, K. M. A.; Fu, J., Microfluidic Blood Cell Sorting: Now and Beyond. *Small (Weinheim an der Bergstrasse, Germany)* **2014,** *10* (9), 1687-1703.

32. Hardwick, J., Blood processing. *ISBT Science Series* **2008,** *3* (2), 148-176.

33. Kreuger, A.; Åkerblom, O.; Högman, C. F., A Clinical Evaluation of Citrate-Phosphate-Dextrose-Adenine Blood. *Vox sanguinis* **1975,** *29* (2), 81-89.

34. Lozada, J. L.; Caplanis, N.; Proussaefs, P.; Willardsen, J.; Kammeyer, G., Platelet-rich plasma application in sinus graft surgery: Part I-Background and processing techniques. *Journal of Oral Implantology* **2001,** *27* (1), 38-42.

35. Pasqualetti, D.; Ghirardini, A.; Arista, M. C.; Vaglio, S.; Fakeri, A.; Waldman, A. A.; Girelli, G., Blood component fractionation: manual versus automatic procedures. *Transfusion and apheresis science* **2004,** *30* (1), 23-28.

36. Rossi, E.; Simon, T., Rossi's principles of transfusion medicine. **2009**.

37. Chernyshev, A. V.; Tarasov, P. A.; Semianov, K. A.; Nekrasov, V. M.; Hoekstra, A. G.; Maltsev, V. P., Erythrocyte lysis in isotonic solution of ammonium chloride: Theoretical modeling and experimental verification. *Journal of theoretical biology* **2008,** *251* (1), 93-107.

38. Bonner, W.; Hulett, H.; Sweet, R.; Herzenberg, L., Fluorescence activated cell sorting. *Review of Scientific Instruments* **1972,** *43* (3), 404-409.

39. Miltenyi, S.; Müller, W.; Weichel, W.; Radbruch, A., High gradient magnetic cell separation with MACS. *Cytometry* **1990,** *11* (2), 231-238.

40. Fukuda, S.; Schmid-Schönbein, G. W., Centrifugation attenuates the fluid shear response of circulating leukocytes. *Journal of leukocyte biology* **2002,** *72* (1), 133-139.

41. Lundahl, J.; Hallden, G.; Hallgren, M.; Sköld, C.; Hed, J., Altered expression of CD11b/CD18 and CD62L on human monocytes after cell preparation procedures. *Journal of immunological methods* **1995,** *180* (1), 93-100.

42. Brass, L. F.; Stalker, T. J.; Zhu, L.; Woulfe, D. S., Signal transduction during platelet plug formation. *Platelets* **2007,** *3*, 367-398.

43. Perrotta, P.; Snyder, E., Platelet storage and transfusion. *Platelets* **2007**, 1265-1295.

44. Wyman, T. H.; Bjornsen, A. J.; Elzi, D. J.; Smith, C. W.; England, K. M.; Kelher, M.; Silliman, C. C., A two-insult in vitro model of PMN-mediated pulmonary endothelial damage: requirements for adherence and chemokine release. *American Journal of Physiology-Cell Physiology* **2002,** *283* (6), C1592-C1603.

45. Yang, X.; Li, N.; Gorenstein, D. G., Strategies for the discovery of therapeutic aptamers. *Expert opinion on drug discovery* **2011,** *6* (1), 75-87.

46. Inganäs, M.; Dérand, H.; Eckersten, A.; Ekstrand, G.; Honerud, A.-K.; Jesson, G.; Thorsén, G.; Söderman, T.; Andersson, P., Integrated microfluidic compact disc device with potential use in both centralized and point-of-care laboratory settings. *Clinical chemistry* **2005,** *51* (10), 1985-1987.

47. Lee, D.; Sukumar, P.; Mahyuddin, A.; Choolani, M.; Xu, G., Separation of model mixtures of epsilon-globin positive fetal nucleated red blood cells and anucleate erythrocytes using a microfluidic device. *Journal of Chromatography A* **2010,** *1217* (11), 1862-1866.

48. Choi, S.; Ku, T.; Song, S.; Choi, C.; Park, J.-K., Hydrophoretic high-throughput selection of platelets in physiological shear-stress range. *Lab on a Chip* **2011,** *11* (3), 413-418.

49. Bose, S.; Singh, R.; Hanewich-Hollatz, M.; Shen, C.; Lee, C.-H.; Dorfman, D. M.; Karp, J. M.; Karnik, R., Affinity flow fractionation of cells via transient interactions with asymmetric molecular patterns. *Scientific reports* **2013,** *3*.

50. Han, K.-H.; Frazier, A. B., Continuous magnetophoretic separation of blood cells in microdevice format. *Journal of Applied Physics* **2004,** *96* (10), 5797-5802.

51. Lenshof, A.; Ahmad-Tajudin, A.; Järås, K.; Swärd-Nilsson, A.-M.; Åberg, L.; Marko-Varga, G. r.; Malm, J.; Lilja, H.; Laurell, T., Acoustic whole blood plasmapheresis chip for prostate specific antigen microarray diagnostics. *Analytical chemistry* **2009,** *81* (15), 6030-6037.

52. Huang, Y.; Joo, S.; Duhon, M.; Heller, M.; Wallace, B.; Xu, X., Dielectrophoretic cell separation and gene expression profiling on microelectronic chip arrays. *Analytical chemistry* **2002,** *74* (14), 3362-3371.

53. SooHoo, J. R.; Walker, G. M., Microfluidic aqueous two phase system for leukocyte concentration from whole blood. *Biomedical microdevices* **2009,** *11* (2), 323-329.

54. Hellesø, O. G.; Løvhaugen, P.; Subramanian, A. Z.; Wilkinson, J. S.; Ahluwalia, B. S., Surface transport and stable trapping of particles and cells by an optical waveguide loop. *Lab on a Chip* **2012,** *12* (18), 3436-3440.

55. Zhang, X.-B.; Wu, Z.-Q.; Wang, K.; Zhu, J.; Xu, J.-J.; Xia, X.-H.; Chen, H.-Y., Gravitational sedimentation induced blood delamination for continuous plasma separation on a microfluidics chip. *Analytical chemistry* **2012,** *84* (8), 3780-3786.

56. Song, J. W.; Cavnar, S. P.; Walker, A. C.; Luker, K. E.; Gupta, M.; Tung, Y.-C.; Luker, G. D.; Takayama, S., Microfluidic endothelium for studying the intravascular adhesion of metastatic breast cancer cells. *PloS one* **2009,** *4* (6), e5756.

57. Di Carlo, D., Inertial microfluidics. *Lab on a Chip* **2009,** *9* (21), 3038-3046.

58. Kuo, J. S.; Zhao, Y.; Schiro, P. G.; Ng, L.; Lim, D. S.; Shelby, J. P.; Chiu, D. T., Deformability considerations in filtration of biological cells. *Lab on a Chip* **2010,** *10* (7), 837-842.

59. Di Carlo, D.; Irimia, D.; Tompkins, R. G.; Toner, M., Continuous inertial focusing, ordering, and separation of particles in microchannels. *Proceedings of the National Academy of Sciences* **2007,** *104* (48), 18892-18897.

60. Huang, L. R.; Cox, E. C.; Austin, R. H.; Sturm, J. C., Continuous particle separation through deterministic lateral displacement. *Science* **2004,** *304* (5673), 987-990.

61. Lee, K.; Shao, H.; Weissleder, R.; Lee, H., Acoustic Purification of Extracellular Microvesicles. *ACS nano* **2015,** *9* (3), 2321-2327.

62. Lenshof, A.; Laurell, T., Continuous separation of cells and particles in microfluidic systems. *Chemical Society Reviews* **2010,** *39* (3), 1203-1217.

63. Pamme, N., Continuous flow separations in microfluidic devices. *Lab Chip* **2007,** *7* (12), 1644-1659.

64. Wei, H., Particle sorting using a porous membrane in a microfluidic device. *Lab Chip* **2011,** *11*, 238-45.

65. Zheng, S., Membrane microfilter device for selective capture, electrolysis and genomic analysis of human circulating tumor cells. *Journal Of Chromatography. A* **2007,** *1162*, 154-61.

66. Bhagat, A. A. S.; Kuntaegowdanahalli, S. S.; Papautsky, I., Inertial microfluidics for continuous particle filtration and extraction. *Microfluid. Nanofluid.* **2009,** *7* (2), 217-226.

67. Chmela, E.; Tijssen, R.; Blom, M. T.; Gardeniers, H. J. G. E.; van den Berg, A., A Chip System for Size Separation of Macromolecules and Particles by Hydrodynamic Chromatography. *Anal. Chem.* **2002,** *74* (14), 3470-3475.

68. Lee, M. G.; Bae, C. Y.; Choi, S.; Cho, H.; Park, J., High-Throughput Inertial Separation Of Cancer Cells From Human Whole Blood In A Contraction-Expansion Array Microchannel. *Proceedings Of Micro Tas* **2011**, 2065-2067.

69. Mach, A. J.; Di Carlo, D., Continuous scalable blood filtration device using inertial microfluidics. *Biotechnol. Bioeng.* **2010,** *107*, 302-11.

70. Mach, A. J.; Kim, J. H.; Arshi, A.; Hur, S. C.; Di Carlo, D., Automated cellular sample preparation using a Centrifuge-on-a-Chip. *Lab Chip* **2011,** *11*, 2827-34.

71. Pamme, N., Continuous flow separations in microfluidic devices. *Lab on a Chip* **2007,** *7* (12), 1644-1659.

72. Yamada, M.; Seki, M., Hydrodynamic filtration for on-chip particle concentration and classification utilizing microfluidics. *Lab Chip* **2005,** *5*, 1233-9.

73. Mach, A. J.; Di Carlo, D., Continuous scalable blood filtration device using inertial microfluidics. *Biotechnol. Bioeng.* **2010,** *107* (2), 302-311.

74. Di Carlo, D.; Edd, J.; Humphry, K.; Stone, H.; Toner, M., Particle Segregation and Dynamics in Confined Flows. *Phys. Rev. Lett.* **2009,** *102*, 1-4.

75. Wang, G.; Mao, W.; Byler, R.; Patel, K.; Henegar, C.; Alexeev, A.; Sulchek, T., Stiffness Dependent Separation of Cells in a Microfluidic Device. *PLoS ONE* **2013,** *8* (10), e75901.

76. McPherson, R.; Pincus, M. R.; Henry, J. B., Henry's clinical diagnosis and management by laboratory methods. Saunders Elsevier: 2007.

77. K Tannenberg, R.; H Lauridsen, L.; R Kanwar, J.; R Dodd, P.; N Veedu, R., Nucleic acid aptamers as novel class of therapeutics to mitigate Alzheimer's disease pathology. *Current Alzheimer Research* **2013,** *10* (4), 442-448.

78. Cheng, X.; Irimia, D.; Dixon, M.; Sekine, K.; Demirci, U.; Zamir, L.; Tompkins, R. G.; Rodriguez, W.; Toner, M., A microfluidic device for practical label-free CD4+ T cell counting of HIV-infected subjects. *Lab on a Chip* **2007,** *7* (2), 170-178.

79. Yu, X.; He, R.; Li, S.; Cai, B.; Zhao, L.; Liao, L.; Liu, W.; Zeng, Q.; Wang, H.; Guo, S. S., Magneto-Controllable Capture and Release of Cancer Cells by Using a Micropillar Device Decorated with Graphite Oxide-Coated Magnetic Nanoparticles. *Small* **2013,** *9* (22), 3895-3901.

80. Cheung, L. S. L.; Zheng, X.; Stopa, A.; Baygents, J. C.; Guzman, R.; Schroeder, J. A.; Heimark, R. L.; Zohar, Y., Detachment of captured cancer cells under flow acceleration in a bio-functionalized microchannel. *Lab on a Chip* **2009,** *9* (12), 1721-1731.

81. Parkinson, D. R.; Dracopoli, N.; Petty, B. G.; Compton, C.; Cristofanilli, M.; Deisseroth, A.; Hayes, D. F.; Kapke, G.; Kumar, P.; Lee, J. S., Considerations in the development of circulating tumor cell technology for clinical use. *Journal of translational medicine* **2012,** *10* (1), 1.

82. Nair, S. V.; Witek, M. A.; Jackson, J. M.; Lindell, M. A.; Hunsucker, S. A.; Sapp, T.; Perry, C. E.; Hupert, M. L.; Bae-Jump, V.; Gehrig, P. A., Enzymatic cleavage of uracil-containing single-stranded DNA linkers for the efficient release of affinity-selected circulating tumor cells. *Chemical Communications* **2015,** *51* (15), 3266-3269.

83. Pullagurla, S. R.; Witek, M. A.; Jackson, J. M.; Lindell, M. A.; Hupert, M. L.; Nesterova, I. V.; Baird, A. E.; Soper, S. A., Parallel affinity-based isolation of leukocyte subsets using microfluidics: Application for stroke diagnosis. *Analytical chemistry* **2014,** *86* (8), 4058-4065.

84. Adams, A. A.; Okagbare, P. I.; Feng, J.; Hupert, M. L.; Patterson, D.; Göttert, J.; McCarley, R. L.; Nikitopoulos, D.; Murphy, M. C.; Soper, S. A., Highly efficient circulating tumor cell isolation from whole blood and label-free enumeration using polymer-based microfluidics with an integrated conductivity sensor. *Journal of the American Chemical Society* **2008,** *130* (27), 8633-8641.

85. Janshoff, A.; Steinem, C., Scanning force microscopy of artificial membranes. *ChemBioChem* **2001,** *2* (11), 798-808.

86. Yuan, Y.; Oberholzer, M.; Lenhoff, A., Size does matter: electrostatically determined surface coverage trends in protein and colloid adsorption. *Colloids and Surfaces A: Physicochemical and Engineering Aspects* **2000,** *165* (1), 125-141.

87. Shah, M. A.; Schwartz, G. K., The relevance of drug sequence in combination chemotherapy. *Drug Resistance Updates* **2000,** *3* (6), 335-356.

88. Simon, A.; Nagel, D.; Kitchen, B.; Bode, U., Clinical relevance of etoposide (VP-16) pharmacokinetics in children and adults. *INTERNATIONAL JOURNAL OF PEDIATRIC HEMATOLOGY/ONCOLOGY* **1997,** *4* (4), 401-414.

89. Ruardy, T.; Schakenraad, J.; Van der Mei, H.; Busscher, H., Preparation and characterization of chemical gradient surfaces and their application for the study of cellular interaction phenomena. *Surface science reports* **1997,** *29* (1), 3-30.

90. Anderson, B. N.; Ding, A. M.; Nilsson, L. M.; Kusuma, K.; Tchesnokova, V.; Vogel, V.; Sokurenko, E. V.; Thomas, W. E., Weak rolling adhesion enhances bacterial surface colonization. *Journal of bacteriology* **2007,** *189* (5), 1794-1802.

91. Tedder, T.; Steeber, D.; Chen, A.; Engel, P., The selectins: vascular adhesion molecules. *The FASEB Journal* **1995,** *9* (10), 866-873.

92. Stone, J. D.; Chervin, A. S.; Kranz, D. M., T-cell receptor binding affinities and kinetics: impact on T-cell activity and specificity. *Immunology* **2009,** *126* (2), 165-176.

93. Barthel, S. R.; Schatton, T., Homing in on the Sweet Side of Immune Checkpoint Biology. *Immunity* **2016,** *44* (5), 1083-1085.

94. Nishimura, Y.; Shimojima, M.; Tano, Y.; Miyamura, T.; Wakita, T.; Shimizu, H., Human P-selectin glycoprotein ligand-1 is a functional receptor for enterovirus 71. *Nature medicine* **2009,** *15* (7), 794-797.

95. Tinoco, R.; Carrette, F.; Barraza, M. L.; Bradley, L. M., The adhesion molecule PSGL-1 is a checkpoint regulator that promotes T cell dysfunction in melanoma tumors. *The Journal of Immunology* **2016,** *196* (1 Supplement), 72.9-72.9.

96. Gong, L.; Cai, Y.; Zhou, X.; Yang, H., Activated platelets interact with lung cancer cells through P-selectin glycoprotein ligand-1. *Pathology & Oncology Research* **2012,** *18* (4), 989-996.

97. Greenberg, A. W.; Hammer, D. A., Cell separation mediated by differential rolling adhesion. *Biotechnology and bioengineering* **2001,** *73* (2), 111-124.

98. Choi, S.; Karp, J. M.; Karnik, R., Cell sorting by deterministic cell rolling. *Lab on a Chip* **2012,** *12* (8), 1427-1430.

99. Huang, R.; Barber, T.; Schmidt, M.; Tompkins, R.; Toner, M.; Bianchi, D.; Kapur, R.; Flejter, W., A microfluidics approach for the isolation of nucleated red blood cells (NRBCs) from the peripheral blood of pregnant women. *Prenatal diagnosis* **2008,** *28* (10), 892-899.

100. Burguillos, M. A.; Magnusson, C.; Nordin, M.; Lenshof, A.; Augustsson, P.; Hansson, M. J.; Elmer, E.; Lilja, H.; Brundin, P.; Laurell, T., Microchannel acoustophoresis does not impact survival or function of microglia, leukocytes or tumor cells. *PLoS One* **2013,** *8* (5), e64233.

101. Islam, M.; Brink, H.; Blanche, S.; DiPrete, C.; Bongiorno, T.; Stone, N.; Liu, A.; Philip, A.; Wang, G.; Lam, W., Microfluidic Sorting of Cells by Viability Based on Differences in Cell Stiffness. *Scientific Reports* **2017,** *7*.

102. Choi, S.; Park, J.-K., Continuous hydrophoretic separation and sizing of microparticles using slanted obstacles in a microchannel. *Lab Chip* **2007,** *7* (7), 890-897.

103. Mao, W.; Alexeev, A., Hydrodynamic sorting of microparticles by size in ridged microchannels. *Physics of Fluids* **2011,** *23* (5), 051704.

104. Wang, G.; Crawford, K.; Turbyfield, C.; Lam, W.; Alexeev, A.; Sulchek, T., Microfluidic cellular enrichment and separation through differences in viscoelastic deformation. *Lab on a Chip* **2015,** *15* (2), 532-540.

105. Lee, W.; Tseng, P.; Di Carlo, D., Microtechnology for Cell Manipulation and Sorting. Springer: 2016.

106. Tsai, M.; Kita, A.; Leach, J.; Rounsevell, R.; Huang, J. N.; Moake, J.; Ware, R. E.; Fletcher, D. A.; Lam, W. A., In vitro modeling of the microvascular occlusion and thrombosis that occur in hematologic diseases using microfluidic technology. *The Journal of Clinical Investigation* **2012,** *122* (1), 11.

107. Wang, G.; Mao, W.; Byler, R.; Patel, K.; Henegar, C.; Alexeev, A.; Sulchek, T., Stiffness Dependent Separation of Cells in a Microfluidic Device. *PLoS ONE* **2013,** *8* (10).

108. Wu, L. Y.; Di Carlo, D.; Lee, L. P., Microfluidic Self-Assembly of Tumor Spheroids for Anti-Cancer Drug Discovery. *Biomedical Microdevices* **2008,** *10* (2), 6.

109. Wang, G.; Crawford, K.; Turbyfield, C.; Lam, W.; Alexeev, A.; Sulchek, T., Microfluidic cellular enrichment and separation through differences in viscoelastic deformation. *Lab on a Chip* **2015**.

110. Schwar, M. J. R.; Weinberg, F. J., The Measurement of Velocity by Applying Schlieren-Interferometry to Doppler-Shifted Laser Light. *Proceedings of the Royal Society of London. Series A, Mathematical and Physical Sciences* **1969,** *311* (1506), 8.

111. Melling, A., Tracer particles and seeding for particle image velocimetry. *Meas. Sci. Technol.* **1997,** *8*, 11.

112. Cheung, K.; Ng, W. B.; Zhang, Y., Three dimensional tracking of particles and their local orientations. *Flow Meas Instrum* **2005,** *16*, 8.

113. Maas, H. G.; Gruen, A.; Papantoniou, D., Particle tracking velocimetry in three-dimensional flows. *Experiments in Fluids* **1993,** *15* (2), 14.

114. Toprak, E.; Balci, H.; Blehm, B. H.; Selvin, P. R., Three-dimensional particle tracking via bifocal imaging. *Nano Lett.* **2007,** *7* (7), 3.

115. Deng, Y.; Shaevitz, J. W., Effect of aberration on height calibration in three-dimensional localization-based microscopy and particle tracking. *Applied Optics* **2009,** *48*, 5.

116. Rogers, S. S.; Waigh, T. A.; Zhao, X.; Lu, J. R., Precise particle tracking against a complicated background: polynomial fitting with Gaussian weight. *Physical Biology* **2007,** *4*, 8.

117. Zhang, Z.; H., M. C., Three-Dimensional particle tracking with subnanometer resolution using off-focus images. *Applied Optics* **2008,** *47* (13), 10.

118. Lewis, J. P., Fast template matching. *Vision Interface '95, Proceedings* **1994**, 120-123.

119. French, T. E., *A Manual of Engineering Drawing for Students and Draftsmen* McGraw-Hill: New York, 1911.

120. Choi, S.; Park, J. K., Continuous hydrophoretic separation and sizing of microparticles using slanted obstacles in a microchannel. *Lab on a Chip* **2007,** *7* (7), 8.

121. Stroock, A. D.; Dertinger, S. K.; Ajdari, A.; Mezic , I.; Stone, H. A.; Whitesides, G. M., Chaotic mixer for microchannels. *Science* **2002,** *295* (5555), 5.

122. Mao, W.; Alexeev, A., Continuous sorting of microparticles by size in ridged microchannels. *Physics of Fluids* **2011**.

123. Meijering, E.; Dzyubachyk, O.; Smat, I., Methods for Cell and Particle Tracking In *Methods in Enzymology*, Conn, P. M., Ed. Elsevier: February 2012; Vol. 504, p 18.

124. Choi, S.; Ku, T.; Song, S.; Choi, C.; Park, J.-K., Hydrophoretic high-throughput selection of platelets in physiological shear-stress range. *Lab Chip* **2011,** *11* (3), 413-418.

125. Tasadduq, B.; Wang, G.; El Banani, M.; Mao, W.; Lam, W.; Alexeev, A.; Sulchek, T., Three-dimensional particle tracking in microfluidic channel flow using in and out of focus diffraction. *Flow Meas. Instrum.* **2015,** *45*, 218-224.

126. Mao, W.; Alexeev, A., Hydrodynamic sorting of microparticles by size in ridged microchannels. *Phys. Fluids* **2011,** *23* (5), 051704.

127. Tasadduq, B.; Wang, G.; El Banani, M.; Mao, W.; Lam, W.; Alexeev, A.; Sulchek, T., Three-dimensional particle tracking in microfluidic channel flow using in and out of focus diffraction. *Flow Measurement and Instrumentation* **2015,** *45*, 218-224.

128. Wang, X.; Liedert, C.; Liedert, R.; Papautsky, I., A disposable, roll-to-roll hot-embossed inertial microfluidic device for size-based sorting of microbeads and cells. *Lab on a Chip* **2016,** *16* (10), 1821-1830.

129. Yamada, M.; Seko, W.; Yanai, T.; Ninomiya, K.; Seki, M., Slanted, asymmetric microfluidic lattices as size-selective sieves for continuous particle/cell sorting. *Lab on a Chip* **2017**.

130. Wu, Z.; Chen, Y.; Wang, M.; Chung, A. J., Continuous inertial microparticle and blood cell separation in straight channels with local microstructures. *Lab Chip* **2016,** *16* (3), 532-542.

131. Choi, S.; Song, S.; Choi, C.; Park, J.-K., Continuous blood cell separation by hydrophoretic filtration. *Lab on a Chip* **2007,** *7* (11), 1532-1538.

132. Chiu, Y.-Y.; Huang, C.-K.; Lu, Y.-W., Enhancement of microfluidic particle separation using cross-flow filters with hydrodynamic focusing. *Biomicrofluidics* **2016,** *10* (1), 011906.

133. Yamada, M.; Seki, M., Hydrodynamic filtration for on-chip particle concentration and classification utilizing microfluidics. *Lab on a Chip* **2005,** *5* (11), 1233-1239.

134. Wu, L.; Guan, G.; Hou, H. W.; Bhagat, A. A. S.; Han, J., Separation of leukocytes from blood using spiral channel with trapezoid cross-section. *Analytical chemistry* **2012,** *84* (21), 9324-9331.

135. Cheng, Y.; Ye, X.; Ma, Z.; Xie, S.; Wang, W., High-throughput and clogging-free microfluidic filtration platform for on-chip cell separation from undiluted whole blood. *Biomicrofluidics* **2016,** *10* (1), 014118.

136. Han, K.-H.; Frazier, A. B., Paramagnetic capture mode magnetophoretic microseparator for high efficiency blood cell separations. *Lab on a Chip* **2006,** *6* (2), 265-273.

137. Han, K.-H.; Frazier, A. B., Lateral-driven continuous dielectrophoretic microseparators for blood cells suspended in a highly conductive medium. *Lab on a Chip* **2008,** *8* (7), 1079-1086.

138. Li, X.; Chen, W.; Liu, G.; Lu, W.; Fu, J., Continuous-flow microfluidic blood cell sorting for unprocessed whole blood using surface-micromachined microfiltration membranes. *Lab on a Chip* **2014,** *14* (14), 2565-2575.

139. Choi, J.; Hyun, J.-c.; Yang, S., On-chip extraction of intracellular molecules in white blood cells from whole blood. *Scientific reports* **2015,** *5*.

140. Jain, A.; Munn, L. L., Biomimetic postcapillary expansions for enhancing rare blood cell separation on a microfluidic chip. *Lab on a chip* **2011,** *11* (17), 2941-2947.

141. Kim, B.; Choi, Y. J.; Seo, H.; Shin, E. C.; Choi, S., Deterministic Migration-Based Separation of White Blood Cells. *Small* **2016,** *12* (37), 5159-5168.

142. Crocker, P. R.; Feizi, T., Carbohydrate recognition systems: functional triads in cell—cell interactions. *Current opinion in structural biology* **1996,** *6* (5), 679-691.

143. Kannagi, R., Regulatory roles of carbohydrate ligands for selectins in the homing of lymphocytes. *Current opinion in structural biology* **2002,** *12* (5), 599-608.

144. Shattil, S. J.; Ginsberg, M. H.; Brugge, J. S., Adhesive signaling in platelets. *Current opinion in cell biology* **1994,** *6* (5), 695-704.

145. Zhu, J.; Xue, J.; Guo, Z.; Zhang, L.; Marchant, R. E., Biomimetic glycoliposomes as nanocarriers for targeting P-selectin on activated platelets. *Bioconjugate chemistry* **2007,** *18* (5), 1366-1369.

146. Ley, K.; Laudanna, C.; Cybulsky, M. I.; Nourshargh, S., Getting to the site of inflammation: the leukocyte adhesion cascade updated. *Nature Reviews Immunology* **2007,** *7* (9), 678-689.

147. Goetz, D. J.; Greif, D. M.; Ding, H.; Camphausen, R. T.; Howes, S.; Comess, K. M.; Snapp, K. R.; Kansas, G. S.; Luscinskas, F. W., Isolated P-selectin glycoprotein ligand-1 dynamic adhesion to P-and E-selectin. *The Journal of cell biology* **1997,** *137* (2), 509-519.

148. Spertini, O.; Cordey, A.-S.; Monai, N.; Giuffrè, L.; Schapira, M., P-selectin glycoprotein ligand 1 is a ligand for L-selectin on neutrophils, monocytes, and CD34+ hematopoietic progenitor cells. *The Journal of cell biology* **1996,** *135* (2), 523-531.

149. Xia, L.; Ramachandran, V.; McDaniel, J. M.; Nguyen, K. N.; Cummings, R. D.; McEver, R. P., N-terminal residues in murine P-selectin glycoprotein ligand-1 required for binding to murine P-selectin. *Blood* **2003,** *101* (2), 552-559.

150. Asa, D.; Raycroft, L.; Ma, L.; Aeed, P. A.; Kaytes, P. S.; Elhammer, A. P.; Geng, J.-G., The P-selectin glycoprotein ligand functions as a common human leukocyte ligand for P-and E-selectins. *Journal of Biological Chemistry* **1995,** *270* (19), 11662-11670.

151. Guyer, D. A.; Moore, K. L.; Lynam, E. B.; Schammel, C.; Rogelj, S.; McEver, R. P.; Sklar, L. A., P-selectin glycoprotein ligand-1 (PSGL-1) is a ligand for L-selectin in neutrophil aggregation. *Blood* **1996,** *88* (7), 2415-2421.

152. Martinez, M.; Joffraud, M.; Giraud, S.; Baïsse, B.; Bernimoulin, M. P.; Schapira, M.; Spertini, O., Regulation of PSGL-1 Interactions with L-selectin, P-selectin, and E-selectin ROLE OF HUMAN FUCOSYLTRANSFERASE-IV AND-VII. *Journal of Biological Chemistry* **2005,** *280* (7), 5378-5390.

153. Tinoco, R.; Otero, D. C.; Takahashi, A. A.; Bradley, L. M., PSGL-1: A New Player in the Immune Checkpoint Landscape. *Trends in Immunology* **2017**.

154. Borges, E.; Eytner, R.; Moll, T.; Steegmaier, M.; Campbell, M. A.; Ley, K.; Mossmann, H.; Vestweber, D., The P-selectin glycoprotein ligand-1 is important for recruitment of neutrophils into inflamed mouse peritoneum. *Blood* **1997,** *90* (5), 1934-1942.

155. Asaduzzaman, M.; Mihaescu, A.; Wang, Y.; Sato, T.; Thorlacius, H., P-selectin and P-selectin glycoprotein ligand 1 mediate rolling of activated CD8+ T cells in inflamed colonic venules. *Journal of Investigative Medicine* **2009,** *57* (7), 765-768.

156. Martín-Fontecha, A.; Baumjohann, D.; Guarda, G.; Reboldi, A.; Hons, M.; Lanzavecchia, A.; Sallusto, F., CD40L+ CD4+ memory T cells migrate in a CD62P-dependent fashion into reactive lymph nodes and license dendritic cells for T cell priming. *Journal of Experimental Medicine* **2008,** *205* (11), 2561-2574.

157. Xu, H.; Manivannan, A.; Jiang, H.-R.; Liversidge, J.; Sharp, P. F.; Forrester, J. V.; Crane, I. J., Recruitment of IFN-γ-producing (Th1-like) cells into the inflamed retina in vivo is preferentially regulated by P-selectin glycoprotein ligand 1: P/E-selectin interactions. *The Journal of Immunology* **2004,** *172* (5), 3215-3224.

158. Nuñez-Andrade, N.; Lamana, A.; Sancho, D.; Gisbert, J. P.; Gonzalez-Amaro, R.; Sanchez-Madrid, F.; Urzainqui, A., P-selectin glycoprotein ligand-1 modulates immune inflammatory responses in the enteric lamina propria. *The Journal of pathology* **2011,** *224* (2), 212-221.

159. Frenette, P. S.; Denis, C. V.; Weiss, L.; Jurk, K.; Subbarao, S.; Kehrel, B.; Hartwig, J. H.; Vestweber, D.; Wagner, D. D., P-Selectin glycoprotein ligand 1 (PSGL-1) is expressed on platelets and can mediate platelet–endothelial interactions in vivo. *Journal of Experimental Medicine* **2000,** *191* (8), 1413-1422.

160. Kum, W. W.; Lee, S.; Grassl, G. A.; Bidshahri, R.; Hsu, K.; Ziltener, H. J.; Finlay, B. B., Lack of functional P-selectin ligand exacerbates Salmonella serovar typhimurium infection. *The Journal of Immunology* **2009,** *182* (10), 6550-6561.

161. Ramos-Sevillano, E.; Urzainqui, A.; de Andrés, B.; González-Tajuelo, R.; Domenech, M.; González-Camacho, F.; Sánchez-Madrid, F.; Brown, J. S.; García, E.; Yuste, J., PSGL-1 on Leukocytes is a Critical Component of the Host Immune Response against Invasive Pneumococcal Disease. *PLoS Pathog* **2016,** *12* (3), e1005500.

162. Lévesque, J.-P.; Zannettino, A. C.; Pudney, M.; Niutta, S.; Haylock, D. N.; Snapp, K. R.; Kansas, G. S.; Berndt, M. C.; Simmons, P. J., PSGL-1-mediated adhesion of human hematopoietic progenitors to P-selectin results in suppression of hematopoiesis. *Immunity* **1999,** *11* (3), 369-378.

163. Urzainqui, A.; del Hoyo, G. M.; Lamana, A.; de la Fuente, H.; Barreiro, O.; Olazabal, I. M.; Martin, P.; Wild, M. K.; Vestweber, D.; González-Amaro, R., Functional role of P-selectin glycoprotein ligand 1/P-selectin interaction in the generation of tolerogenic dendritic cells. *The Journal of Immunology* **2007,** *179* (11), 7457-7465.

164. Xu, T.; Zhang, L.; Geng, Z. H.; Wang, H.-B.; Wang, J.-T.; Chen, M.; Geng, J.-G., P-selectin cross-links PSGL-1 and enhances neutrophil adhesion to fibrinogen and ICAM-1 in a Src kinase-dependent, but GPCR-independent mechanism. *Cell adhesion & migration* **2007,** *1* (3), 115-123.

165. Tinoco, R.; Carrette, F.; Barraza, M. L.; Otero, D. C.; Magaña, J.; Bosenberg, M. W.; Swain, S. L.; Bradley, L. M., PSGL-1 Is an Immune Checkpoint Regulator that Promotes T Cell Exhaustion. *Immunity* **2016,** *44* (5), 1190-1203.

166. Kim, D.; Herr, A. E., Protein immobilization techniques for microfluidic assays. *Biomicrofluidics* **2013,** *7* (4), 041501.

167. Martinez, A. W.; Phillips, S. T.; Whitesides, G. M.; Carrilho, E., Diagnostics for the developing world: microfluidic paper-based analytical devices. ACS Publications: 2009.

168. Hughes, A. J.; Lin, R. K.; Peehl, D. M.; Herr, A. E., Microfluidic integration for automated targeted proteomic assays. *Proceedings of the National Academy of Sciences* **2012,** *109* (16), 5972-5977.

169. Rubina, A. Y.; Kolchinsky, A.; Makarov, A. A.; Zasedatelev, A. S., Why 3-D? Gel-based microarrays in proteomics. *Proteomics* **2008,** *8* (4), 817-831.

170. Thorsen, T.; Maerkl, S. J.; Quake, S. R., Microfluidic large-scale integration. *Science* **2002,** *298* (5593), 580-584.

171. Rusmini, F.; Zhong, Z.; Feijen, J., Protein immobilization strategies for protein biochips. *Biomacromolecules* **2007,** *8* (6), 1775-1789.

172. Křenková, J.; Foret, F., Immobilized microfluidic enzymatic reactors. *Electrophoresis* **2004,** *25* (21-22), 3550-3563.

173. Asanomi, Y.; Yamaguchi, H.; Miyazaki, M.; Maeda, H., Enzyme-immobilized microfluidic process reactors. *Molecules* **2011,** *16* (7), 6041-6059.

174. Bange, A.; Halsall, H. B.; Heineman, W. R., Microfluidic immunosensor systems. *Biosensors and Bioelectronics* **2005,** *20* (12), 2488-2503.

175. Hermanson, G. T., *Bioconjugate techniques*. Academic press: 2013.

176. Liu, P.; Li, X.; Greenspoon, S. A.; Scherer, J. R.; Mathies, R. A., Integrated DNA purification, PCR, sample cleanup, and capillary electrophoresis microchip for forensic human identification. *Lab on a Chip* **2011,** *11* (6), 1041-1048.

177. Li, Q.; Lee, G.; Ong, C.; Lim, C., AFM indentation study of breast cancer cells. *Biochemical and biophysical research communications* **2008,** *374* (4), 609-613.

178. Herman, C. T.; Potts, G. K.; Michael, M. C.; Tolan, N. V.; Bailey, R. C., Probing Dynamic Cell-Substrate Interactions using Photochemically Generated Surface-Immobilized Gradients: Application to Selectin-Mediated Leukocyte Rolling. *Integrative biology : quantitative biosciences from nano to macro* **2011,** *3* (7), 779-791.

179. Wang, G.; Turbyfield, C.; Crawford, K.; Alexeev, A.; Sulchek, T., Cellular enrichment through microfluidic fractionation based on cell biomechanical properties. *Microfluidics and Nanofluidics* **2015,** *19* (4), 987-993.

180. Kishimoto, T. K.; Jutila, M. A.; Berg, E. L.; Butcher, E. C., Neutrophil Mac-1 and MEL-14 adhesion proteins inversely regulated by chemotactic factors. *Science* **1989,** *245* (4923), 1238-1242.

181. Orsini, J. J.; Kay, D. M.; Saavedra-Matiz, C. A.; Wenger, D. A.; Duffner, P. K.; Erbe, R. W.; Biski, C.; Martin, M.; Krein, L. M.; Nichols, M., Newborn screening for Krabbe disease in New York State: the first eight years' experience. *Genetics in Medicine* **2016,** *18* (3), 239-248.

182. Yu, Z. T. F.; Yong, K. M. A.; Fu, J., Microfluidic Blood Cell Preparation: Now and Beyond. *Small (Weinheim an der Bergstrasse, Germany)* **2014,** *10* (9), 1687-1703.

183. McEver, R. P., Selectins: initiators of leukocyte adhesion and signaling at the vascular wall. *Cardiovascular research* **2015**, cvv154.

184. Kazuya, I.-P.; Weyrich, A. S.; Zimmerman, G. A.; McEver, R. P., Engagement of P-selectin glycoprotein ligand-1 enhances tyrosine phosphorylation and activates mitogen-activated protein kinases in human neutrophils. *Journal of Biological Chemistry* **1997,** *272* (45), 28750-28756.

185. Watanabe, K.; Terakura, S.; Martens, A. C.; van Meerten, T.; Uchiyama, S.; Imai, M.; Sakemura, R.; Goto, T.; Hanajiri, R.; Imahashi, N., Target Antigen Density Governs the Efficacy of Anti–CD20-CD28-CD3 ζ Chimeric Antigen Receptor–Modified Effector CD8+ T Cells. *The Journal of Immunology* **2015,** *194* (3), 911-920.

186. Karp, J. M.; Teo, G. S. L., Mesenchymal stem cell homing: the devil is in the details. *Cell stem cell* **2009,** *4* (3), 206-216.

187. Reticker-Flynn, N. E.; Malta, D. F. B.; Winslow, M. M.; Lamar, J. M.; Xu, M. J.; Underhill, G. H.; Hynes, R. O.; Jacks, T. E.; Bhatia, S. N., A combinatorial extracellular matrix platform identifies cell-extracellular matrix interactions that correlate with metastasis. *Nature communications* **2012,** *3*, 1122.

188. Kim, G.; Davidson, B.; Henning, R.; Wang, J.; Yu, M.; Annunziata, C.; Hetland, T.; Kohn, E. C., Adhesion molecule protein signature in ovarian cancer effusions is prognostic of patient outcome. *Cancer* **2012,** *118* (6), 1543-1553.

189. Rhee, M.; Valencia, P. M.; Rodriguez, M. I.; Langer, R.; Farokhzad, O. C.; Karnik, R., Synthesis of Size-Tunable Polymeric Nanoparticles Enabled by 3D Hydrodynamic

Flow Focusing in Single-Layer Microchannels. *Advanced Materials* **2011,** *23* (12), H79-H83.

190. Lee, G.-B.; Chang, C.-C.; Huang, S.-B.; Yang, R.-J., The hydrodynamic focusing effect inside rectangular microchannels. *Journal of Micromechanics and Microengineering* **2006,** *16* (5), 1024.

191. Stiles, T.; Fallon, R.; Vestad, T.; Oakey, J.; Marr, D.; Squier, J.; Jimenez, R., Hydrodynamic focusing for vacuum-pumped microfluidics. *Microfluidics and Nanofluidics* **2005,** *1* (3), 280-283.

192. Rabinowitz, J. D.; Beeson, C.; Lyons, D. S.; Davis, M. M.; McConnell, H. M., Kinetic discrimination in T-cell activation. *Proceedings of the National Academy of Sciences* **1996,** *93* (4), 1401-1405.

193. Valitutti, S.; Muller, S.; Cella, M.; Padovan, E.; Lanzavecchia, A., Serial triggering of many T-cell receptors by a few peptide-MHC complexes. *Nature* **1995,** *375* (6527), 148.

194. Fritz, J.; Katopodis, A. G.; Kolbinger, F.; Anselmetti, D., Force-mediated kinetics of single P-selectin/ligand complexes observed by atomic force microscopy. *Proceedings of the National Academy of Sciences* **1998,** *95* (21), 12283-12288.

195. Bell, G. I., Models for the specific adhesion of cells to cells. *Science* **1978,** *200* (4342), 618-627.

196. Dong, C.; Lei, X. X., Biomechanics of cell rolling: shear flow, cell-surface adhesion, and cell deformability. *Journal of biomechanics* **2000,** *33* (1), 35-43.

197. Sarangapani, K. K.; Marshall, B. T.; McEver, R. P.; Zhu, C., Molecular stiffness of selectins. *Journal of Biological Chemistry* **2011,** *286* (11), 9567-9576.